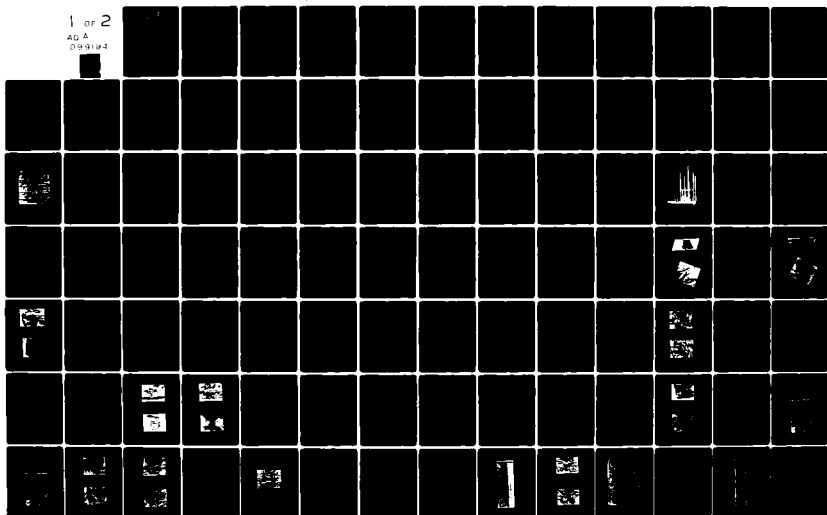


AD-A099 194 ILLINOIS UNIV AT URBANA DEPT OF METALLURGY AND MINING--ETC F/6 11/6  
FRACTURE KINETICS OF HYDROGEN EMBRITTLED NIOBIUM.(U)  
MAR 81 B S HINDIN, H K BIRNBAUM N00014-75-C-1012  
NL

UNCLASSIFIED

1 of 2

AD A  
009194



AD A099194

LEVEL

2

3

6 FRACTURE KINETICS OF HYDROGEN EMBRITTLED NIOBIUM.

9 Technical Report

Barry S Hindin and H K Birnbaum

University of Illinois at Urbana Champaign

Technical Report - Office of Naval Research

15 Contract USN 00014-75-C-1012

4 March 1981

12 176

10 Barry Scott Hindin  
H. K. Birnbaum

DTIC  
ELECTRA  
MAY 18 1981

DTIC FILE COPY

This document is unclassified. Distribution and reproduction is permitted for any purpose of the US government.

DISTRIBUTION STATEMENT A

Approved for public release;  
Distribution Unlimited

81 4 13 067

## FRACTURE KINETICS OF HYDROGEN EMBRITTLED NIOBIUM

Barry Scott Hindin, Ph.D.

Department of Metallurgy and Mining Engineering  
University of Illinois at Urbana-Champaign, 1981

Kinetics of crack propagation in hydrogen charged niobium were studied in the temperature range 77 to 303 K and for hydrogen concentrations between 0.068 and 3.2 at.%. Crack velocities between  $10^{-8}$  and  $10^{-2}$  m/s were determined as a function of the Mode I stress intensity factors using single edge notch and double torsion specimens. . Validity of the double torsion technique was established using a variety of methods including photoelastic analysis of the stresses in the plane normal to the specimen's crack surface.

Increasing, decreasing and constant  $K_I$  tests were carried out and the  $\ln V$  versus  $K_I$  data exhibited various behavior depending upon the type of loading. Linking up of fracturing hydrides was shown to be responsible for a unique three region (V-K) behavior which occurred only at intermediate temperatures for decreasing  $K_I$  tests. Analysis of the temperature dependence for Stage II during constant  $K_I$  tests indicated that the cracking kinetics are controlled by hydrogen diffusion to the crack tip. Differences between crack velocities in deuterium and hydrogen charged specimens were consistent with the isotopic differences in their diffusion coefficients. Fracture surfaces of the test specimens were examined and shown to exhibit features consistent with their crack velocity behavior.

## TABLE OF CONTENTS

	Page
1. INTRODUCTION . . . . .	1
2. REVIEW OF PREVIOUS RESEARCH. . . . .	3
2.1 Stress Effects on Hydrogen Solubility . . . . .	3
2.2 Stress Effects on Hydride Solvus. . . . .	4
2.3 Subcritical Crack Growth Behavior and Mechanism . . . . .	6
2.4 Crack Propagation Measurements and Techniques . . . . .	10
3. THEORY . . . . .	16
3.1 Constant Deflection Double Torsion Test (Decreasing $K_I$ ) . . . . .	16
3.2 Constant Load Double Torsion Test (Constant $K_I$ ) . . . . .	18
4. EXPERIMENTAL PROCEDURE . . . . .	20
4.1 Sample Preparation. . . . .	20
4.1.1 Single Edge Notch Specimens. . . . .	20
4.1.2 Double Torsion Specimens . . . . .	24
4.2 Double Torsion Compliance Measurements. . . . .	29
4.3 Loading Procedures. . . . .	29
4.3.1 Single Edge Notch Specimens. . . . .	29
4.3.2 Double Torsion Specimens . . . . .	32
4.3.2.1 Constant Deflection Tests (Decreasing $K_I$ ) . . . . .	32
4.3.2.2 Plastic Correction for Constant Deflection Tests. . . . .	32
4.3.2.3 Constant Load Tests (Constant $K_I$ ) . . . . .	36
4.3.2.4 Plastic Correction for Constant Load Tests. . . . .	36
5. RESULTS. . . . .	39
5.1 Single Edge Notch Data (Increasing $K_I$ ). . . . .	39
5.1.1 Increasing $K_I$ (V-K) Curves . . . . .	40
5.1.2 Fractography . . . . .	56
5.2 Double Torsion Data . . . . .	61

## TABLE OF CONTENTS (Continued)

Page

5.2.1	Compliance Measurements . . . . .	61
5.2.2	Constant Deflection (Decreasing $K_I$ ) . . . . .	66
5.2.2.1	High Temperature (V-K) Curves. . . . .	66
5.2.2.2	High Temperature Fractography. . . . .	70
5.2.2.3	Low Temperature (V-K) Curves . . . . .	70
5.2.2.4	Low Temperature Fractography . . . . .	75
5.2.2.5	Intermediate Temperature (V-K) Curves . . . . .	75
5.2.2.6	Intermediate Temperature Fractography . . . . .	83
5.2.3	Constant Load (Constant $K_I$ ) Data. . . . .	90
5.2.3.1	Constant $K_I$ (V-K) Curves . . . . .	90
5.2.3.2	Constant $K_I$ Fractography . . . . .	94
5.2.4	Critical Hydride Size . . . . .	98
6.	DISCUSSION . . . . .	105
6.1	Single Edge Notch Data (Increasing $K_I$ Tests) . . . . .	105
6.2	Double Torsion Specimen. . . . .	109
6.2.1	Decreasing $K_I$ Data. . . . .	109
6.2.2	Constant $K_I$ Data . . . . .	125
6.3	Theoretical Stage II Activation Energy . . . . .	126
6.4	Threshold Stress Intensity Factors . . . . .	136
7.	SUMMARY AND CONCLUSIONS . . . . .	142
APPENDIX A	PHOTOELASTIC INVESTIGATION OF DOUBLE TORSION GEOMETRY. . . . .	144
A.1	Introduction . . . . .	144
A.2	Experimental Procedure . . . . .	145
A.3	Model Fringe Value Calculation . . . . .	147
A.4	Principal Stress Differences and Directions. . . . .	150
A.5	Mode I Opening . . . . .	166

Accession For

NTIS GRA&amp;I

DTIC TAB

Unannounced

Per file

By

Distribution

Availability Codes

Avail and/or

Dist

A

## TABLE OF CONTENTS (Continued)

	Page
APPENDIX B ERROR ANALYSIS OF (V-K) DATA . . . . .	169
B.1 Single Edge Notch Tests . . . . .	169
B.2 Double Torsion Tests. . . . .	170
B.2.1 Stress Intensity Factor. . . . .	170
B.2.2 Constant Deflection Method (Decreasing $K_I$ ) .	171
B.2.3 Constant Load Method (Constant $K_I$ ) . . . . .	172
APPENDIX C VELOCITY MEASUREMENT LIMITS. . . . .	173
C.2 Double Torsion, Constant Deflection (Decreasing $K_I$ )	173
C.3 Double Torsion, Constant Load (Constant $K_I$ ) . . . . .	174
REFERENCES . . . . .	175
VITA . . . . .	179

## 1. INTRODUCTION

The phenomenon of hydrogen embrittlement of pure metals and alloys has been extensively researched.<sup>(1)</sup> It is now recognized that a single mechanism cannot account for all instances of hydrogen embrittlement. Based on the degree of hydrogen solubility in metals, two classes of hydrogen embrittlement can be distinguished. The first class includes metals that have low hydrogen solubility, endothermic heats of solution, and do not form stable hydrides, e.g. copper, iron and molybdenum. Some elements in this class, e.g. iron, nickel and their alloys have severe susceptibility to hydrogen embrittlement, while others e.g., aluminum and molybdenum have moderate susceptibility or are insensitive like copper. The second class includes metals that have high hydrogen solubility, exothermic heats of solution and form stable hydrides. This class includes all elements belonging to groups IVa and Va of the periodic table and many others which form stable hydrides such as lithium, titanium and magnesium. The formation of stable hydrides in these metals causes their severe susceptibility to hydrogen embrittlement. Niobium is a member of the second class.

In specimens which form stable hydrides while under external stress, the embrittlement process involves two main steps. The first step requires hydrogen to diffuse down a stress gradient to the stress concentrator where a hydride is formed. The second step is the fracture of the hydride. The crack tip advances by a repetition

of these steps. The first step controls the crack velocity since the hydride itself fractures quite rapidly.

This study investigates the kinetics of crack propagation in hydrogen embrittled niobium to further understand the embrittlement mechanism. Kinetics are presented in terms of crack velocity as a function of stress intensity factor. The fracture mechanics approach was used since the stress intensity can relate the crack tip stresses to the externally applied stresses. Double torsion and single edge notch specimen were used in crack velocity measurements. Photoelastic analysis of the double torsion specimen was undertaken and evidence for Mode I stress intensity at the crack tip is presented. Fractography was used to correlate fracture surface features to crack velocity kinetics. Crack velocity measurements as a function of increasing, decreasing and constant stress intensity were made. Several contributing factors are shown to explain the crack velocity behavior in each case. These factors include the type of loading a specimen undergoes, the magnitude of the loading and the test temperature proximity to the specimen's solvus temperature. The ideas presented here are generally applicable to other exothermic hydrogen occluders forming stable hydrides.



## 2. REVIEW OF PREVIOUS RESEARCH

### 2.1 Stress Effects on Hydrogen Solubility

An expression relating the solubility of hydrogen in a stress free solid to the solubility in a stressed solid was given by Grossbeck<sup>(2)</sup> as

$$C_H^\sigma / C_H^0 = \exp(W_H - \bar{w}_H) / RT \quad (1)$$

where  $W_H$  = total work per mole addition of hydrogen,  
 $\bar{w}_H$  = partial molar strain energy.

Equation (1) was derived using the thermodynamic approach of stressed solids of Li et al.<sup>(3)</sup> Puls<sup>(4)</sup> has shown an identical result can be derived for hydride forming alloys using the atomistic model of Eshelby. It was further shown<sup>(2,5)</sup> that for a specimen subjected to a triaxial tension stress field and assuming all shear stresses to be zero, Eqn. (1) becomes

$$C_H^\sigma / C_H^0 = \exp(P_{\text{hyd}} \cdot \bar{V}_H / RT) \quad (2)$$

where  $\bar{V}_H$  = partial molal volume of hydrogen in the metal,

$P_{\text{hyd}}$  = hydrostatic stress given by  $(\sigma_{11} + \sigma_{22} + \sigma_{33})/3$ .

Values calculated for  $C_H^\sigma / C_H^0$  in zirconium ranged from 1.65 to 1.005 depending upon temperature and stress.<sup>(5)</sup> For niobium, in plane stressed specimens, Grossbeck<sup>(2)</sup> has shown the ratio  $C_H^\sigma / C_H^0$  to be as high as 66 for a temperature of 77 K and a stress of one tenth the shear modulus.

## 2.2 Stress Effects on Hydride Solvus

Grossbeck<sup>(2)</sup> noted that the increase of hydrogen at a crack tip from an applied stress does not by itself result in hydride precipitation for an exothermic occluder. The chemical potential of the hydride phase must be lowered upon application of an external stress in order for the solvus to be raised. Flanagan et al.<sup>(6)</sup> have distinguished between the effects of uniform and nonuniform applied stress fields on the thermodynamics of hydride precipitation. Elastic and plastic constraints were not considered. Their conclusions can be summarized as follows.

1. For systems where partial molal volumes of hydrogen in the hydride and solid solution are equal, a uniform stress has no effect on the solvus.
2. For the case where the partial molal volumes are not equal, a uniform stress has a small effect on the solvus depending upon the magnitude to the differences in partial molal volumes.
3. For a nonuniform stress, a hydride will precipitate when the chemical potentials of the unstressed volume of the solid solution and the stressed volume of the hydride are equal. This occurs even in the absence of a structural change in forming the hydride.

Westlake and Ockers,<sup>(7)</sup> using electrical resistivity methods, have shown that the terminal solid solubility for the niobium-hydrogen system depended on the cooling rate. In addition, the alpha-beta solvus exhibited a hysteresis for the precipitation and reversion of the beta phase. The magnitude of the hysteresis depended on the number of thermal cycles the specimen underwent and in the absence of an external stress, they found the solvus to be given by

$$\ln C_H^0 = 1.320 - 11.45(\text{kJ/mol})/RT_s^0(n) \quad (3)$$

where  $C_H^0$  = hydrogen concentration in atom fraction,

$T_s^0(n)$  = stress free solvus temperature after many thermal cycles.

It has long been known that the formation of niobium hydride is accompanied by a 12% increase of the molar volume.<sup>(8)</sup> This led Birnbaum et al.<sup>(9)</sup> to consider the effects of elastic and plastic deformations resulting from hydride precipitation in the alpha-beta solvus. They showed that the elastic accommodation due to cooling was reversed during re-solution and the plastic accommodation was responsible for the hysteresis in the heating and cooling cycles. Electron microscopy has been used to observe the accommodation effects of hydride precipitation for niobium-hydrogen alloys.<sup>(10)</sup> It was found that during precipitation, volume increase of the beta phase was accommodated elastically and by punching out of interstitial dislocation loops in the alpha phase. Upon dissolution of the hydride during heating, volume decrease was accommodated by recovery of elastic strain and dislocation processes.

Grossbeck and Birnbaum<sup>(11)</sup> showed that the alpha-beta solvus increases in the presence of an external tensile stress and its free energy change is given by

$$\Delta G_{\alpha \rightarrow \beta}^{\sigma} = \Delta G_{\alpha \rightarrow \beta}^0 - \sum \sigma_{ij} e_{ij} \cdot \bar{V} \quad (4)$$

where  $\sigma_{ij}$  = applied stress,

$e_{ij}$  = strain tensor describing the alpha-beta phase change,

$\bar{V}$  = molar volume.

It was also shown, that a further increase in the solvus results from the external stress assisting the plastic accommodation process during precipitation. Grossbeck<sup>(2)</sup> showed that the solvus temperature given in Eqn. (3), is increased in the presence of an external stress by the amount given by

$$\Delta T_s = -P\Delta V/R(1.320 - \ln C_H) \quad (5)$$

where  $P$  = applied hydrostatic stress,

$\Delta V$  = volume change accompanying hydride formation.

For applied stress of 0.05 of the shear modulus under plane stress conditions, increases of 18 K to 28 K were found for hydrogen concentrations between 0.1 and 2.0 at %, respectively. Birnbaum et al.<sup>(9)</sup> have calculated the equilibrium solvus based on a consideration of the plastic and elastic contributions to the molar free energy change in forming the beta phase hydride. Puls,<sup>(5)</sup> however, contends that the equilibrium solvus cannot in general be calculated but must be measured experimentally. Koike and Suzuki<sup>(12)</sup> presented evidence for triaxial stresses not contributing to stress induced hydride formation at a crack tip in the case of vanadium-hydrogen alloys. For these alloys, the alpha to beta phase transformation resembles a martensitic transformation and a uniaxial tension appears responsible for the stress induced hydride formation.

### 2.3 Subcritical Crack Growth Behavior and Mechanisms

It has been observed<sup>(13-17)</sup> that subcritical crack growth often exhibits three distinct stages of crack velocity ( $V$ ) versus

stress intensity ( $K_I$ ), (Fig. 1). Stage I occurs at the low  $K_I$  values and low crack velocities and is characterized by a steep dependence of  $V$  on  $K_I$  and a possible threshold stress intensity,  $K_{I_0}$ . Stage II is characterized by a plateau region where the crack velocity is independent of  $K_I$ . Stage III represents the onset of unstable crack growth and rapid fracture near  $K_{IC}$ .

Several investigations<sup>(15,18-20)</sup> of stress corrosion cracking exhibited three stage (V-K) curves. It was suggested that Stage II results from a rate limiting mechanism such as diffusion of the corrosive component to the crack tip. Three stage behavior has also been found by Nelson<sup>(21)</sup> for titanium alloys fractured in hydrogen gas atmospheres. He presented a film rupture model of hydrogen-induced slow growth for these alloys which include 6Al-4V, 5Al-2.5Sn and 8Al-1Mo-1V. They share common microstructures all of which exhibit acicular alpha phase platelets in a beta phase matrix. Three stage behavior has been observed for certain high strength steels e.g. 4130 and 4340 in gaseous hydrogen.<sup>(22)</sup> Non-metallic systems have also exhibited three stages of crack velocity. Examples of these include polycrystalline alumina in toluene,<sup>(23)</sup> polymethylmethacrylate in air<sup>(23)</sup> and soda lime glass in air.<sup>(16)</sup>

On the basis of the behavior of 18-Ni-maraging steels in gaseous hydrogen, Hudak and Wei<sup>(18)</sup> has suggested that the  $K_I$  independence of Stage II velocities is due to a rate limited chemical process which restricts the amount of hydrogen delivered to the fracture zone. An activation energy for the rate limiting step can be calculated for constant  $K_I$  tests using a family of Stage II

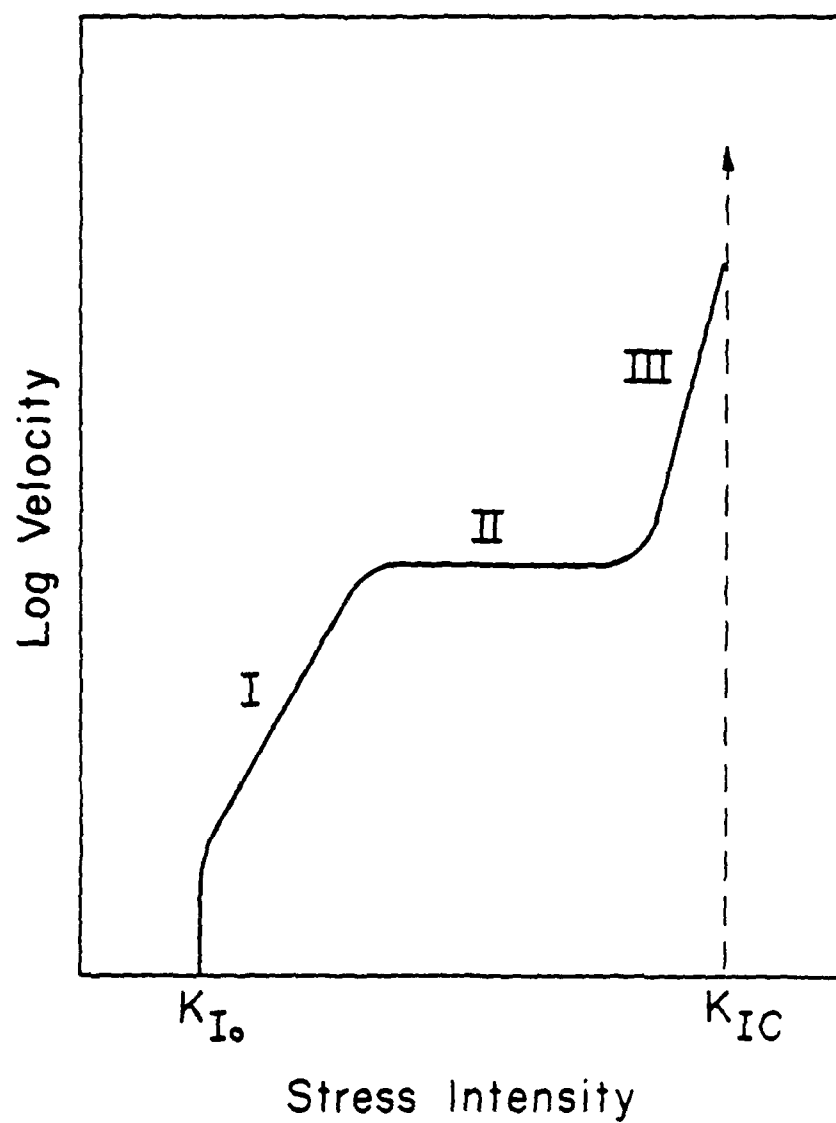


Fig. 1. Crack velocity versus  $K_I$  diagram exhibiting three stage behavior.

velocity data taken at various temperatures. Activation energies measured for these steels do not as yet suggest a definite mechanism. In particular it is noted that activation energies for hydrogen permeation in these steels are two to three times larger than the activation energies which characterize Stage II crack propagation.<sup>(18)</sup> Williams and Nelson<sup>(24)</sup> suggested that the adsorption of hydrogen on steel surfaces is the rate limiting step of gaseous hydrogen assisted crack growth. A similar rate limiting process due to surface transfer is advocated by Oriani and Josephic<sup>(25)</sup> in their lattice decohesion model for hydrogen assisted cracking in steels.

The occurrence of three stage behavior in hydrogen embrittled refractory alloys has been well established. Early work on Zircalloy by Dutton et al.<sup>(26)</sup> suggested Stage I and Stage II were independent phenomenon being controlled by elastic and plastic zone stress fields, respectively. However, more recent work by Simpson and Puls<sup>(27)</sup> suggested that Stage I is not due to a different mechanism than Stage II. Indeed, Stage II does not even appear to exist. Also much emphasis was placed on the conditioning of the machined specimen notch in order to obtain what they considered valid test results. It will be shown in this thesis, that three stage behavior for hydrogen embrittled niobium exists and its absence or presence is a function of the type of loading a specimen undergoes.

## 2.4 Crack Propagation Measurements and Techniques

Techniques for measuring crack propagation fall in two categories. The first requires the direct visual observation of the crack tip either by eye or video tape recorder. The second involves indirect measurement of the crack velocity. This would include acoustic emission, potential drop, load relaxation and crosshead displacement. Each of these techniques have advantages and disadvantages. The type of equipment available to an investigator would be important in determining which technique one would use.

The most common fracture mechanics specimens used in crack propagation measurements are the single edge notched (s.e.n.), double cantilever beam (d.c.b.), center cracked tensile (c.c.t.), and compact tension (c.t.) specimens. Less used but gaining in popularity, for reasons explained below, is the double torsion specimen (d.t.).

Only the tapered d.c.b. specimen and d.t. specimen are constant  $K_I$  specimens. That is,  $K_I$  is independent of the crack length. This is particularly useful since  $K_I$  is then simply proportional to the applied load. The measurements of crack velocities in specimens other than the d.t. specimen are more difficult. The potential drop method when applied to the c.t., tapered d.c.b. or wedge opening loaded etc. specimens requires very stable and low noise constant current supplies. Careful calibration techniques are required when a change in load is attempted during a test in order to relate the potential drop to the correct crack extension. (28)



Crack velocity measurements in the d.t. specimen are particularly simple. As described in the Theory section in more detail, only the monitoring of either the load relaxation or crosshead displacement as a function of time is required. Moreover, the geometry of the d.t. specimen consists simply of a thin plate, minimizing the amount of machining and metal required for a specimen. It was primarily for these reasons that the d.t. specimen was chosen for these test.

The d.t. specimen, whose geometry is shown in Fig. 2 was designed by Outwater and Gerry<sup>(29)</sup> but first reported by Kies and Clark.<sup>(30)</sup> It was developed in response to the need for a specimen which was simple to machine and enable crack velocities to be measured in severe testing environments. The equations governing the crack velocity and stress intensity for the d.t. specimen are derived in the Theory section. These equations, however, apply strictly to specimens undergoing elastic deflection only. This assumption is true for glass or ceramics (at room temperature) but is not generally correct for steels or niobium. Another assumption in the derivation of these analytic equations involves the crack front profile. Ideally, the crack front is normal to the specimen's top surface whereas in reality it is a sloping curve as shown in Fig. 3. Departure from a perpendicular crack front increases as one goes to increasingly ductile materials. To correct for the nonideal crack front profile, a multiplicative constant derived in section 5.2.1 is applied to the analytical equations. This factor must be empirically found for each material but does not differ

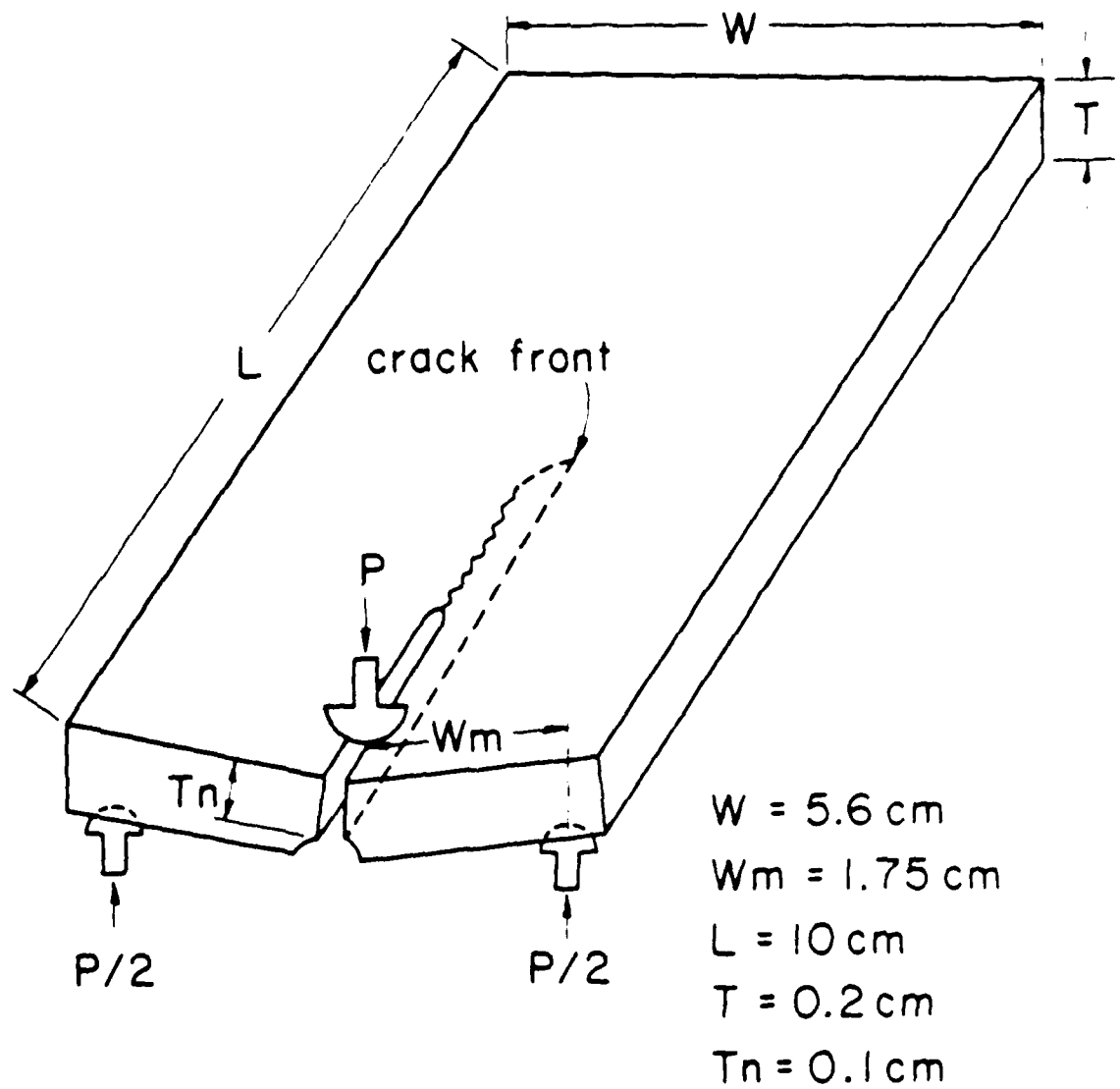


Fig. 2. Double torsion specimen geometry with typical dimensions.

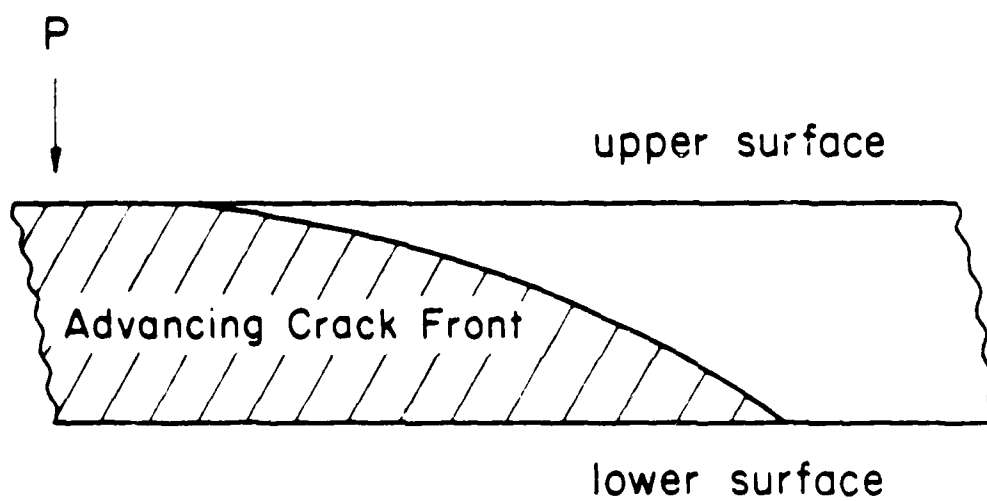


Fig. 3. Typical crack front profile of d.t. specimen.

greatly from unity in most cases. Pollet and Burns<sup>(31)</sup> and Shetty et al.<sup>(32)</sup> have derived additional crack velocity correction factors for the d.t. specimen which essentially give the same results as the method used in this investigation.

Trantina<sup>(33)</sup> measured the stress intensity factor of the d.t. specimen as a function of crack length and ligament length using a three dimensional elastic finite-element stress analysis. He found the stress intensity was nearly constant through one half the specimen's thickness and the analytical equations were correct for crack lengths greater than  $0.55 W$  and ligament lengths less than  $0.65W$  where  $W$  is the specimen's width.

An additional test for the validity of the d.t. specimen is to compare its results with measurements taken from specimen geometries which are known to give "correct" fracture mechanics data. A comparison between bend specimens and d.t. specimens agreed very well in measurements of the critical stress intensity factor.<sup>(23)</sup> Comparisons of the (V-K) data for glass and 4130 steel using d.c.b. and d.t. specimens, showed very similar functional dependence except that the d.t. specimens had a consistently higher crack velocity by a factor of five.<sup>(23)</sup> This discrepancy has been attributed to the nonideal crack front profile discussed above. For niobium, during constant  $K_I$  tests, the bottom crack advance length measured after a run with a micrometer, was within 10% of the length calculated from velocity and time data. Various other checks of the validity of the d.t. specimen geometry for fracture of the niobium-hydrogen

alloys were made as will be discussed and these all indicated that the tests give valid  $K_I$  data. Procedures for taking into account the contribution to the deflection from the plastic behavior of niobium will be presented in the Experimental Procedure section.

### 3. THEORY

The usefulness of the d.t. specimen geometry in measuring subcritical crack growth as a function of stress intensity factor is due to two properties. One is that the stress intensity is independent of the crack length, i.e. a constant  $K_I$  specimen. Secondly, the crack velocity can be calculated by monitoring either the rate of load relaxation (constant crosshead deflection test) or the rate of crosshead deflection (constant load test). The derivation of the equations governing the velocity at constant load,  $V_p$ , and at constant crosshead deflection,  $V_y$ , is given below.

#### 3.1 Constant Deflection Double Torsion Test (Decreasing $K_I$ )

Novozhilov<sup>(34)</sup> showed that the d.t. specimen's compliance,  $C$ , for small deflections and for plates whose width,  $W$ , is much greater than its thickness,  $T$ , is given by

$$C = (3w_m a / WT^3 \mu) = y/P \quad (6)$$

where  $a$  = crack length measured from specimen's edge.

$w_m$  = moment arm length,

$\mu$  = shear modulus,

$P$  = load,

$y$  = deflection of specimen due to loading.

Williams and Evans<sup>(23)</sup> showed that the stress intensity factor,

assuming the crack front profile is independent of crack length,  
is given by

$$K_I = Pw_m [3(1 + \nu)/WT^3 T_n]^{1/2} \quad (7)$$

where  $\nu$  = Poisson's ratio,

$T_n$  = Thickness of specimen minus groove depth.

Since the factors  $\nu$ ,  $W$ ,  $T$  and  $T_n$  are constants which depend only on the specimen's dimensions and mechanical properties, they can be combined into one constant to yield

$$C_1 = W_m [3(1 + \nu)/WT^3 T_n]^{1/2} \quad (8)$$

The constant,  $C_1$ , has units of  $(\text{length})^{-3/2}$ . Equation (7) can then be rewritten as

$$K_I = C_1 P \quad (7)$$

For constant deflection (decreasing  $K_I$ ),  $a = a(t)$ ,  $P = P(t)$  and  $y = \text{constant}$ . Rearranging Eqn. (6), there follows

$$y(t) = 3w_m^2 aP/WT^3 \mu \quad (6')$$

and since

$$\mu = E/2(1 + \nu) \quad (9)$$

where  $E$ , is Young's modulus, implies

$$y(t) = 6w_m^2 (1 + \nu) aP/WT^3 E \quad (10)$$

Differentiating Eqn. (10) with respect to time,  $t$ , yields

$$(\partial y / \partial t)_y = 0 = [3w_m^2 / WT^3 \mu] \cdot [(\partial a / \partial t)_y P + (\partial P / \partial t)_y a] \quad (11)$$

which implies

$$(\partial a / \partial t)_y = -(a/P) \cdot (\partial P / \partial t)_y \quad (12)$$

From Eqn. (6),

$$a = WT^3 Ey / 6Pw_m^2 (1 + \nu) \quad (13)$$

and substituting the above expression for,  $a$ , into Eqn. (12) yields

$$V_y \equiv (\partial a / \partial t)_y = -[WT^3 Ey / P^2 6w_m^2 (1 + \nu)] \cdot (\partial P / \partial t)_y \quad (14)$$

Again grouping the constants, there follows,

$$C_2 = -WT^3 E / 6w_m^2 (1 + \nu) \quad (15)$$

where  $C_2$  has units of force. Equation (14) can then be rewritten as

$$V_y = (C_2 y / P^2) \cdot (\partial P / \partial t)_y \quad (14')$$

### 3.2 Constant Load Double Torsion Test (Constant $K_I$ )

For constant load conditions,  $y = y(t)$ ,  $a = a(t)$  and  $P =$  constant. Letting

$$\alpha = 6w_m^2 (1 + \nu) / WT^3 E, \quad (16)$$

Eqn. (10) becomes

$$y(t) = \alpha \cdot a(t) \cdot P. \quad (10')$$



Differentiating the above expression with respect to time yields,

$$(\partial a / \partial t)_p = (\alpha P)^{-1} (\partial y / \partial t)_p \quad (17)$$

or

$$V_p \equiv (\partial a / \partial t)_p = [WT^3E/6w_m^2(1 + \nu)P] \cdot (\partial y / \partial t)_p \quad (18)$$

Expressing the above equation in terms of  $C_2$  results in

$$V_p = -(C_2/P) \cdot (\partial y / \partial t)_p \quad (19)$$

The crack length,  $a$ , is taken as the longest portion which occurs on the bottom of the specimen. The consequence of this is shown in the compliance measurements of the d.t. tests in the Results Section. Photoelastic analysis of the d.t. geometry is presented in the Appendix. It will be shown that the stress intensity factor given in Eqn. (7), closely resembles the stress intensity for Mode I loading, i.e.  $K_I$ .

#### 4. EXPERIMENTAL PROCEDURE

##### 4.1 Sample Preparation

##### 4.1.1 Single Edge Notch Specimens

Niobium specimens having a single edge notch geometry were prepared from 0.1 cm rolled sheet obtained from Wah Chang Albany Corporation. Typical specimen dimensions are shown in Fig. 4. Reference lines from 150 to 90 microns apart were engraved on the specimen's surfaces with a diamond stylus (Fig. 5). These lines allowed the average velocity of the crack to be calculated by the following expression,

$$V = \Delta x / \Delta t \quad (19)$$

where  $\Delta x$  = crack advance distance,

$\Delta t$  = elapsed time of crack advance.

To remove surface contamination, the specimens were etched after machining, in a solution with equal parts by volume of  $\text{HNO}_3$ , HF and lactic acid. The mass spectrographic analysis before annealing is shown in Table 1. All s.e.n. specimens were annealed prior to hydrogen charging in a vacuum of  $6.5 \times 10^{-8}$  Pa and held at 2300 K for several hours. The typical grain size diameter after annealing was 0.3 cm. Specimens were charged with hydrogen concentrations from 0.068 to 0.74 at % in an ultra high vacuum charging apparatus which allowed equilibration of the specimens with hydrogen gas

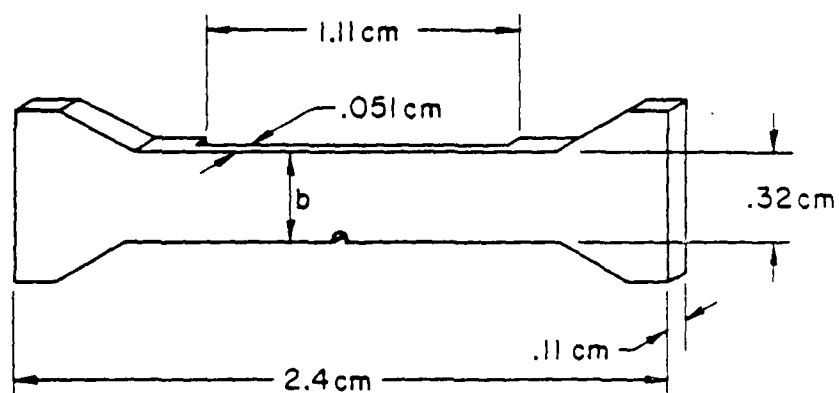
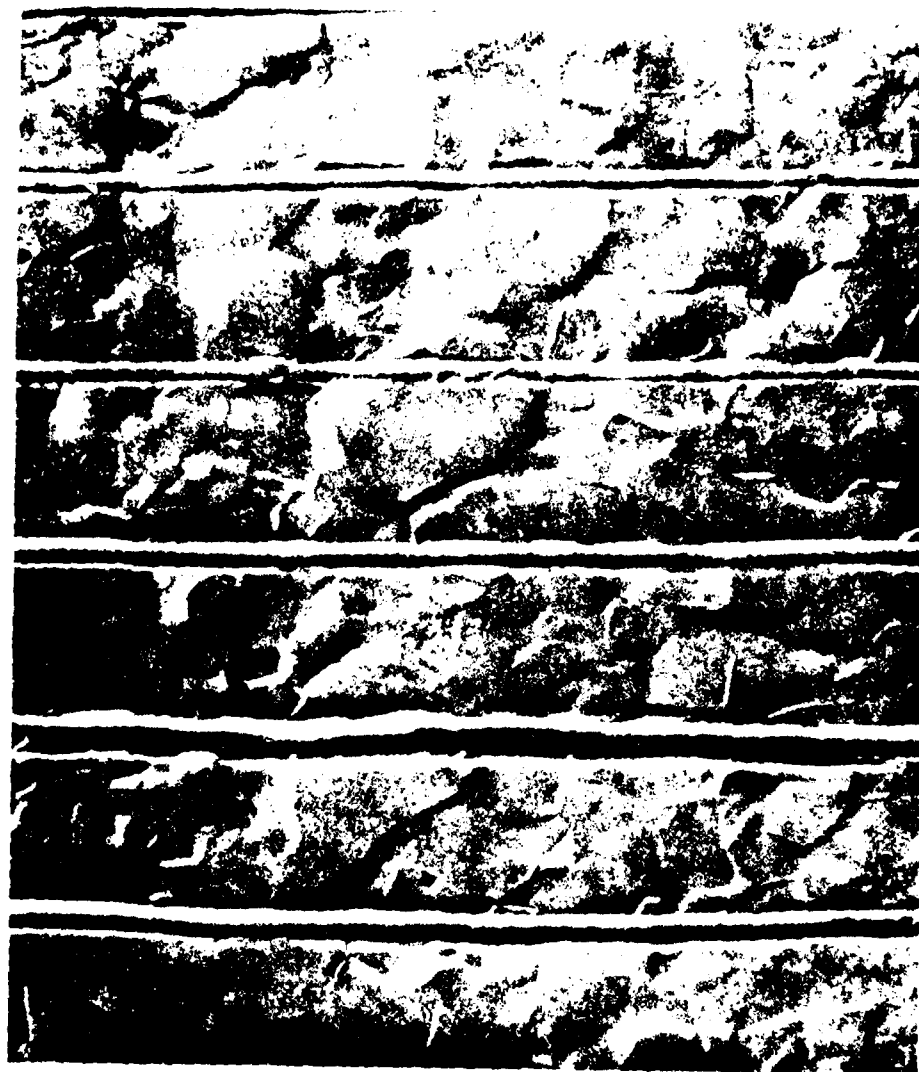


Fig. 4. Single edge notch specimen geometry and dimensions.



150  $\mu\text{m}$

Fig. 5. In etched reference film on s.c.m. specimen surface.

TABLE 1  
Mass Spectrographic Analysis of Niobium  
(Concentrations in atomic ppm)

---

F	0.4
S	4
Cl	3
Ti	0.1
V	0.2
Cr	0.04
Mn	0.03
Fe	0.03
Cu	0.1
Zn	0.06
Zr	0.06
Mo	0.04
Ta	10
W	5

---

(purified by a palladium membrane cell) at controlled temperature and pressure. Vacuum fusion analysis was used to measure the interstitial impurities. Typical values are found in Table 2.

#### 4.1.2 Double Torsion Specimens

Double torsion specimens were prepared from 0.2 cm plate obtained from Wah Chang Albany Corporation. Mass spectrographic analyses for the substitutional impurities in the niobium stock are shown in Table 3. The ASTM grain size was 4.5 in the rolling direction.

Electron discharge machining was used to cut grooves down the center of one side to a depth of approximately one half the specimen thickness and was also used to cut a notch to a length of 3 cm on one end of each specimen. This was done to avoid end effects which exhibit nonlinear behavior of the compliance change as a function of crack length. This is discussed further in section 5.2.1. Thirty gauge wire was used in all e.d.m. Typical dimensions of the specimens after machining are shown in Fig. 2. Etching of the d.t. specimens were carried out as described for the s.e.n. specimens after which they were either annealed or used as received. Specimens to be annealed were placed in a vacuum of  $10^{-4}$  Pa and held at 2300 K for several hours. Typical final grain size diameter was 0.7  $\mu$ m.

The charging procedure was similar to the one described for s.e.n. specimens and consists of heating the d.t. specimens to 973 K under a vacuum of  $1.3 \times 10^{-4}$  Pa. Purified hydrogen gas was then introduced at the appropriate pressure to achieve the desired hydrogen

TABLE 2  
Vacuum Fusion Analysis for  
Hydrogen Charged S.E.N. Specimens  
(Concentrations in at. %)

Specimen	O	H	N
112	0.064	0.068	0.028
114	0.035	0.178	0.019
119	0.090	0.50	0.016
121	0.080	0.50	0.023
124-129	0.076	0.30	0.025

TABLE 3

Mass Spectrographic Analysis for  
Niobium Double Torsion Specimens  
(Concentrations in atomic ppm)

---

F	10
Al	3
S	8
K	3
Ca	15
Cr	2
Fe	2
Ni	3
Cu	1
Ta	30
W	10

---



concentration in solution. This concentration was maintained by slowly lowering both the specimen temperature and hydrogen gas pressure by the appropriate amounts. This procedure is followed until a temperature of approximately 400 K was reached. It is fortunate that an oxide layer forms on the surface for temperatures under about 520 K which prevents hydrogen from diffusing out after charging. Deuterium gas was used to charge several d.t. specimens to determine whether an isotope effect could be seen in the (V-K) curves. The charging procedure for deuterium was the same as for hydrogen except the equilibration times are longer due to deuterium's smaller diffusion coefficient. Vacuum fusion analysis for selected annealed and unannealed specimens are shown in Table 4.

After charging, the d.t. specimens were then suitable for testing using the constant deflection method (decreasing  $K_I$ ). Specimens to be used for the constant load tests (constant  $K_I$ ) were fatigued to initiate a small sharp crack in front of the machined notch. Fatiguing was carried out on a four column table MTS machine using a frequency of 2 Hz and sinusoidally loading between 44.5 and 534 N with a mean load of 245 N. The total number of cycles was  $10^4$ . The final fatigue crack length was typically 0.08 cm. Specimens were fatigued after hydrogen charging since niobium-hydrogen alloys fatigue more rapidly using low frequency loading rates than at high frequency loading rates. (35)

TABLE 4

Typical Interstitial Concentrations for Charged  
Niobium Double Torsion Specimens  
(Concentrations in at. %)

Specimen	Annealed	H	O	N	C
14	Yes	0.55	0.035	0.016	0.015
19	No	2.3	0.056	0.031	0.006
49	No	0.30	0.068	0.018	0.009

#### 4.2 Double Torsion Compliance Measurements

Williams and Evans<sup>(23)</sup> showed that  $K_I$  for the d.t. specimen could be expressed as

$$K_I = [(E/2T_n)(dC/da)]^{1/2} \quad (20)$$

where  $(dC/da)$  is found by differentiating the compliance,  $C$ , given by Eqn. (6) with respect to crack length,  $a$ , and is given by

$$(dC/da) = [6w_m^2(1 + \nu)/WT^3E] \quad (21)$$

To determine any discrepancy between the theoretical and measured values of  $K_I$  for niobium d.t. specimens, the compliance as a function of crack length was measured. Incremental crack lengths were cut with a jeweler's saw at an inclination which approximated the actual crack front profile. Results of the compliance measurements at 77 K and 273 K are presented and discussed in section 5.2.1.

#### 4.3 Loading Procedures

##### 4.3.1 Single Edge Notch Specimens

Single edge notch specimens were tested in a tensile cold stage designed to be used in a JEOL JSM-U3 scanning electron microscope.<sup>(2)</sup> Load was controlled by a variable speed motor and measured by a piezoelectric quartz load cell. Strain and strain rate were recorded by gear driven potentiometers. A video tape recorder monitored the propagating crack by recording the video signal from the s.e.m.

The basic equation that was used for calculating  $K_I$  for the s.e.n. specimen has been given by Gerberich and Katz<sup>(36)</sup> as

$$K_I = (P/hW)a^{1/2}f(a/W) \quad (22)$$

where  $P$  = applied load,

$h$  = specimen thickness,

$W$  = specimen width,

$a$  = crack length measured from specimen edge,

$$f(a/W) = 2[\sin^2(\pi a/2W) + \sec^2(\pi a/2W)]. \quad (23)$$

This expression agrees within 1% of Brown and Srawley's<sup>(37)</sup> fourth order polynomial for  $K_I$  for values of  $(a/W)$  less than 0.65.

For s.e.n. experiments used in this research, the notch was "u" shaped to serve as a stress concentrator and Eqn. (22) was slightly modified to take this into account. The modification was in the form of a multiplicative factor obtained by the graphical solutions of Peterson<sup>(38)</sup> for the effect of stress concentrators on s.e.n. specimens. As an illustration for the typical amount of correction required to Eqn. (22),  $f(a/W)$  versus  $(a/W)$  is shown in Fig. 6 for s.e.n. specimen 119. The dashed portion of the curve represents the effect of the "u" shaped notch on  $f(a/W)$ . Data acquisition was normally restricted to  $(a/W)$  greater than 0.15 and less than 0.70. For  $(a/W)$  greater than 0.70,  $f(a/W)$  becomes increasingly less accurate. Difficulties with the s.e.n. specimen tests will be discussed in the Results Section.

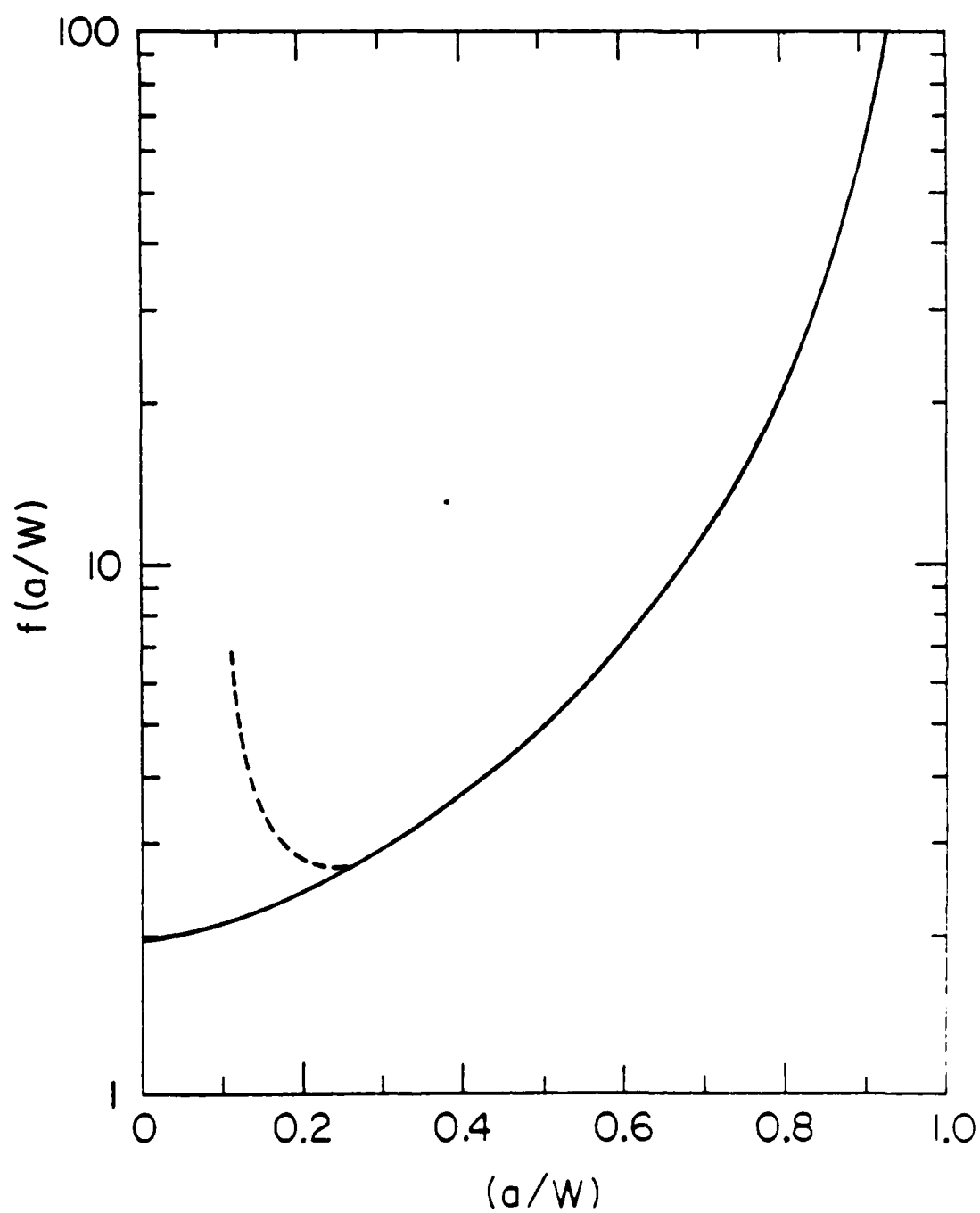


Fig. 6. Graph of  $f(a/W)$  versus  $(a/W)$  for s.e.n. specimen 119. Dashed portion of curve represents effect of the "u" shaped notch on  $f(a/W)$ .

#### 4.3.2 Double Torsion Specimens

##### 4.3.2.1 Constant Deflection Tests (Decreasing $K_I$ )

An Instron loading machine, floor model F/CM, was used for all the d.t. tests. Figure 7 shows the d.t. loading stage which was attached to the bottom of the Instron's moveable crosshead. A typical loading procedure for constant deflection would consist of the following. A charged specimen was rapidly loaded to a preselected value (loading rate,  $r_L$ , was controlled by the crosshead speed which was 0.2 cm/min). Then the crosshead was stopped and the Instron's load cell and a linear variable differential transformer (which measured crosshead displacement) were interfaced with a Wang 720C computer that calculated and printed out the crack velocity, stress intensity factor and the error associated with these parameters. Specimens temperatures were controlled by use of inert freezing mixture baths or by a regulated flow of nitrogen gas.

##### 4.3.2.2 Plastic Correction for Constant Deflection Tests

The equations given in the Theory section apply strictly for the case of a crack propagating in linear elastic medium. For niobium this is rarely the situation except at very low temperatures near 77 K. Therefore, at temperatures above 77 K, there exists two contributions to the load relaxation in a hydrogen charged specimen being fractured under load. One contribution is from the propagating crack. The other is due to plastic deformation caused by low temperature creep.

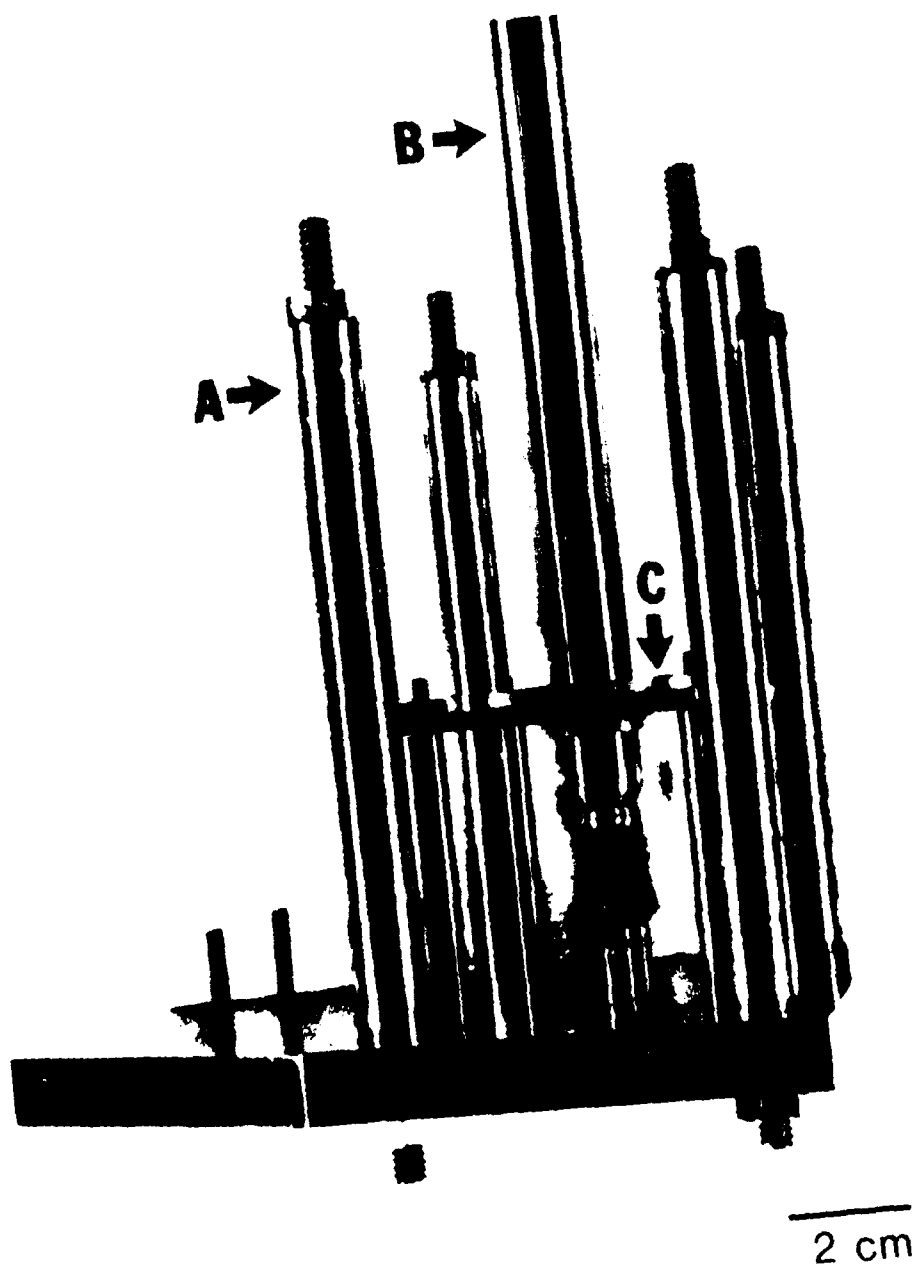


Fig. 1. Stainless steel detector cell. Four posts (A) attach to under side of detector. Load rod (B) is connected to the detector and guided by nylon sleeve (C).

In order to correct for this plasticity contribution, the procedure outlined below was followed.

1. A load relaxation curve using a hydrogen charged specimen was recorded on a strip chart, as described in section 4.3.2.1.
2. The test was repeated using an uncharged specimen under the identical conditions and similarly recorded.
3. Strip charts from steps 1 and 2 were superimposed as shown schematically in Fig. 8.
4. At each point in time,  $t$ , the load relaxation,  $P_c(t)$ , due only to the advancing crack tip was given by<sup>c</sup>

$$P_c(t) = P_m(t) - P_p(t) + P_o \quad (24)$$

- where  $P_m(t)$  = load relaxation curve from the charged specimen,  
 $P_p(t)$  = load relaxation curve from the uncharged specimen,  
 $P_o$  = initial load both the uncharged and charged specimens are brought to at the moment the crosshead is stopped ( $t = 0$ ).
5. Time versus  $P_c(t)$  was plotted and using Eqns. (14') and (7') the corrected velocities and stress intensity factors, respectively were calculated.
  6. Velocity versus stress intensity data points from step 5 were plotted.

Shown in Fig. 8 is a region of the superimposed curves which are in complete coincidence and is labeled " $t_{inc}$ ". This appears to represent a region where no cracking occurs in the charged specimen and can be explained by assuming the existence of an incubation time for a growing hydride to reach a critical size before cracking. A systematic study of this incubation period was not undertaken. However, it was found that the incubation period was longest at the low temperatures and shortest at high temperatures with times ranging



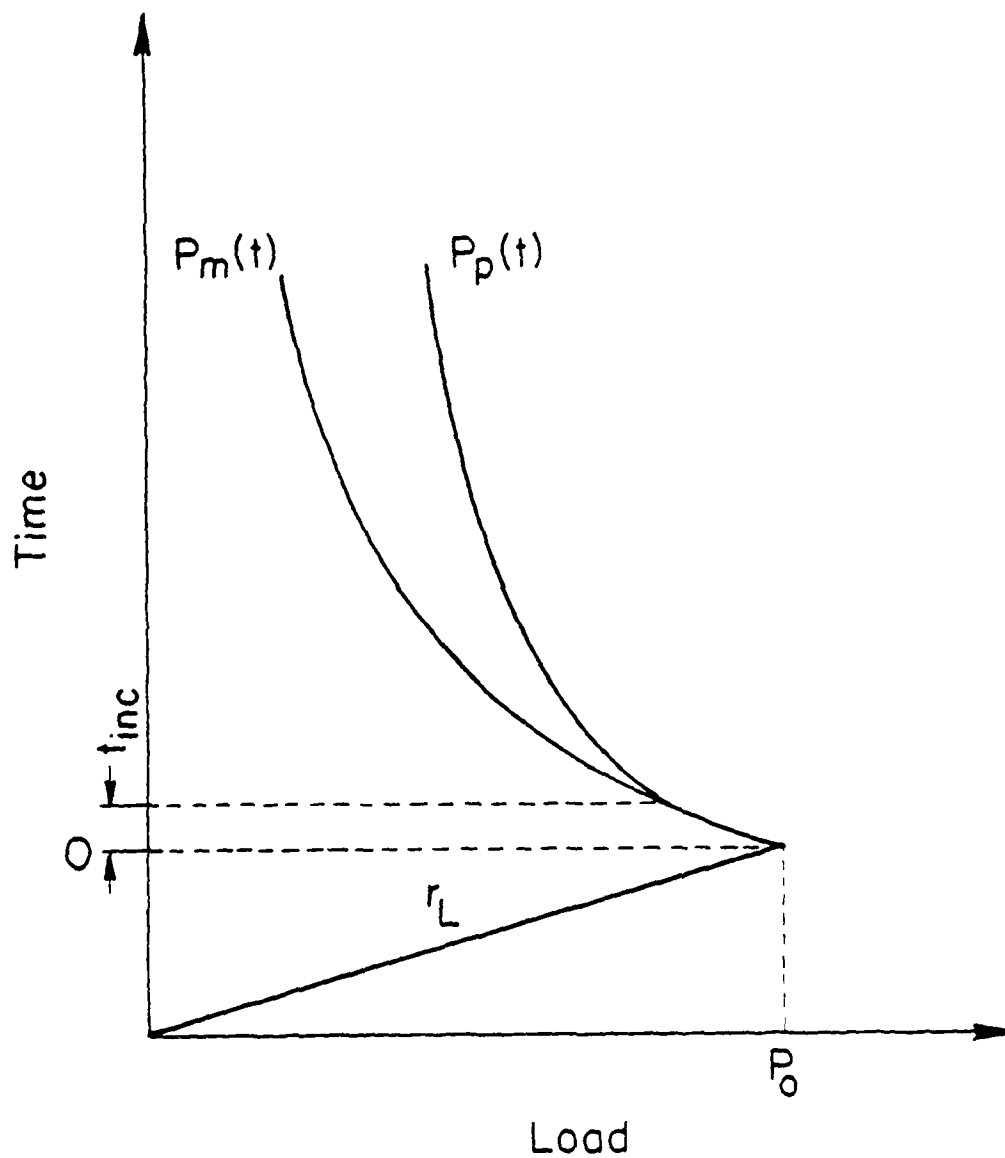


Fig. 8. Diagram of superimposed strip charts for load relaxations due to hydrogen charged specimen ( $P_m(t)$ ) and uncharged specimen ( $P_p(t)$ ). Initial load,  $P_0$  was the same for both specimens,  $r_L$  was the load rate (0.2 cm/min) and  $t_{inc}$  the interval where both curves coincided.

from a few seconds to over a minute. A theoretical estimate of the critical hydride size is given in the Results sections.

#### 4.3.2.3 Constant Load Tests (Constant $K_I$ )

The procedure for constant load testing was analogous to the constant deflection method. However; in this case a constant load was maintained instead of constant deflection. This was accomplished by means of an Instron servo load control system which will automatically maintain a desired load by changing the crosshead position.

Change in crosshead displacement was monitored as a function of time and the calculated crack velocities along with its errors were printed out on a teletype. It was instructive to note that the constant load tests do not yield as much data from each d.t. specimen compared to the constant deflection test. One d.t. specimen usually generates an entire (V-K) curve using the constant deflection procedure whereas only one or two data points are obtainable using the constant load method. Many specimens, therefore, may be required to complete a (V-K) curve for each temperature and hydrogen concentration when using the constant load method.

#### 4.3.2.4 Plastic Correction for Constant Load Tests

Two contributions to the change in crosshead displacement as a function of time will occur and these are analogous to the contributions to the load change in the constant deflection tests. The constant load test will result in greater plasticity corrections

than the constant deflection test for equal hydrogen concentrations, test temperatures and stress intensities.

Fig. 9 schematically shows the crosshead displacement as a function of time for charged and uncharged specimens as recorded on a strip chart. The correction procedure used has been summarized below.

1. Crosshead displacement was recorded on a strip chart for a hydrogen charged specimen.
2. Step 1 was repeated using an uncharged specimen.
3. Using Eqn. (18'), the crack velocities  $V_c$  for the charged specimen, and  $V_p$  for the uncharged specimen were calculated.
4. The differences between  $V_c$  and  $V_p$  at equal times represents the velocity due only to the advancing crack,  $V_c$ , i.e.

$$V_c = V_m(t) - V_p(t) . \quad (25)$$

The velocity due only to the advancing crack tip was found to be essentially a constant, independent of time and represented one data point on a (V-K) curve. An additional test was required for every change in load, i.e. stress intensity and/or temperature.

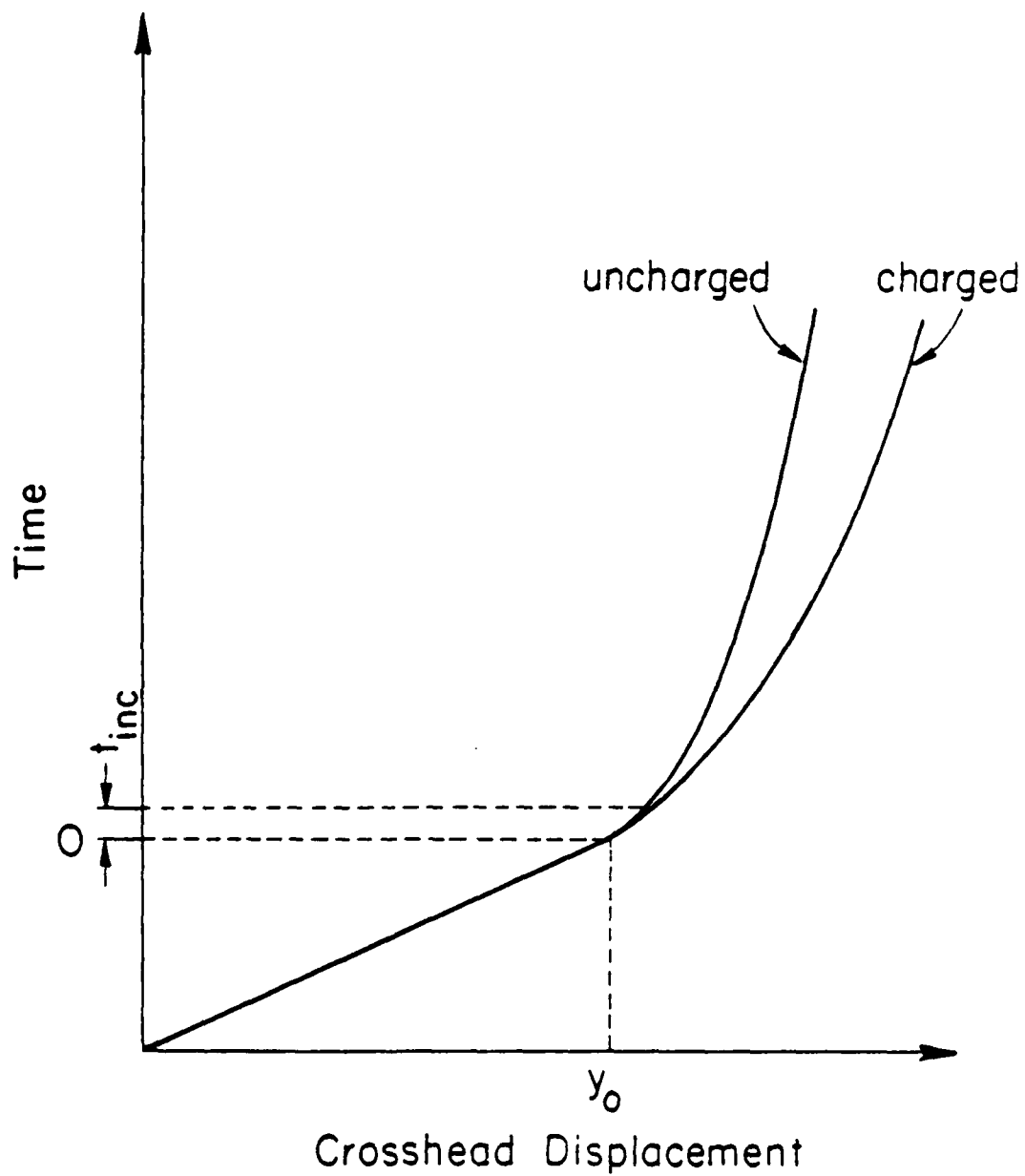


Fig. 9. Diagram of superimposed strip charts for time versus crosshead displacement for charged and uncharged d.t. specimens. Initial crosshead displacement was  $y_0$ . The interval where both curves coincided was denoted by  $t_{inc}$ .

## 5. RESULTS

The accuracy of measurements for crack velocities and stress intensities using s.e.n. and d.t. specimens were limited by various uncertainties in the parameters of Eqns. (7), (14), (18), (19) and (22). By estimating these uncertainties, conservative probable errors were calculated for  $V$  and  $K_I$ . The error analyses are presented in Appendix C. Factors limiting the measurements for maximum and minimum crack velocities using the s.e.n. and d.t. specimens are discussed in Appendix B.

### 5.1 Single Edge Notch Data (Increasing $K_I$ )

Use of the scanning electron microscope tensile stage, though initially successful, met with experimental difficulties on attempting to examine a wide range of crack velocities, hydrogen concentrations and temperatures. Desired strain rates were difficult to achieve and/or maintain due to inherent limitations of the tensile stage motor. Temperature range was limited by the very slow cooling rate of the stage and thermal losses to the microscope column. The major obstacle encountered using s.e.n. specimens was the occurrence of fracture by initiation of multiple cracks. Multiple crack fronts made the calculations of stress intensity factors difficult.

### 5.1.1 Increasing $K_I$ (V-K) Curves

Crack propagation data from the s.e.n. specimens represent increasing  $K_I$  tests. As the crack advanced,  $K_I$  increased according to the expression given by Eqn. (21). Table 5 lists the conditions under which the s.e.n. specimens were tested and includes the hydrogen concentration in solid solution at the test temperature, hydrogen concentration in hydride form prior to loading, true strain to failure,  $\epsilon_f$ , average strain rate,  $\dot{\epsilon} = \epsilon_f / \Delta t$ , stress free solvus and test temperature. Figures 10-13 shows (V-K) results for these tests. Curves were not fitted for Figs. 12 and 13 due to a lack of data points.

All s.e.n. specimens, except specimen 114, were tested slightly below their solvus temperatures. Specimens 119 and 121, which were tested under very similar conditions, exhibited similar (V-K) behavior. The stress intensity factor threshold occurred between 7 and 12  $\text{MPa}\cdot\text{m}^{1/2}$  for specimens 119 and 121, respectively. Stage II behavior is evident in the (V-K) curve of specimen 119 shown in Fig. 10 for  $K_I$  values greater than 30  $\text{MPa}\cdot\text{m}^{1/2}$ . The (V-K) curve for specimen 121, shown in Fig. 11, displays a similar trend in V as  $K_I$  increases beyond 30  $\text{MPa}\cdot\text{m}^{1/2}$ . The (V-K) data for specimen 112 shown in Fig. 13 suggests the existence of a stress intensity factor threshold at approximately 23  $\text{MPa}\cdot\text{m}^{1/2}$  and a comparison with the data for specimens 119 and 121 suggests an increase of  $K_{I0}$  as the test temperature decreases. While the curves are not completely

TABLE 5  
Single Edge Notch Test Conditions

Specimen	Hydrogen Concentration In Solid Solution At Test Temperature (at. %)	Hydrogen Concentration In Hydride Form Prior To Loading (at. %)	Stress Free Solvus Temperature (K)	Test Temperature (K)	True Strain To Failure (%)	Average Strain Rate (s <sup>-1</sup> )
112	0.043	0.025	160	152	2.2	$5.5 \times 10^{-5}$
114	0.178	none	180	183	2.4	$1.0 \times 10^{-4}$
121	0.27	0.23	208	190	2.2	$4.3 \times 10^{-5}$
119	0.38	0.12	208	200	2.3	$6.6 \times 10^{-5}$

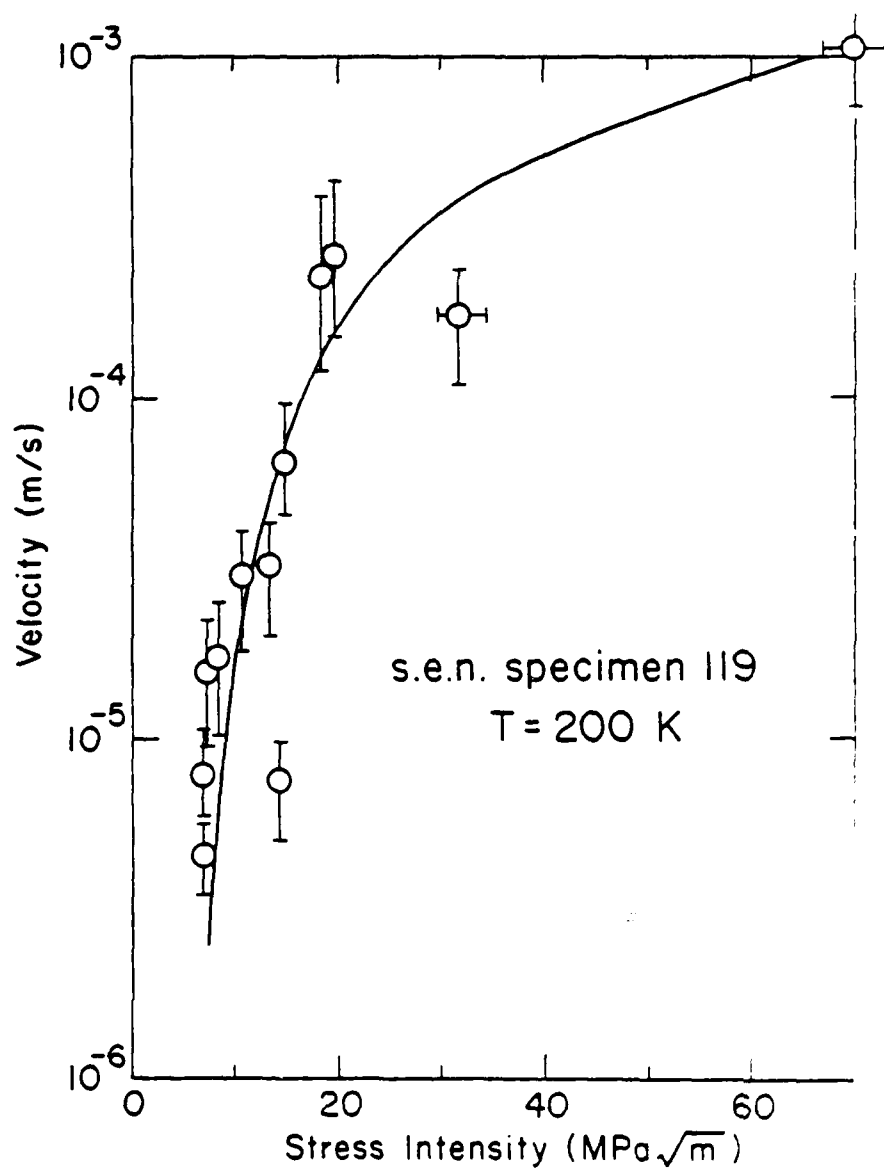


Fig. 10. Crack velocity versus  $K_I$  for s.e.n. specimen 119 tested at 200K and  $H/Nb = 0.5\%$ .



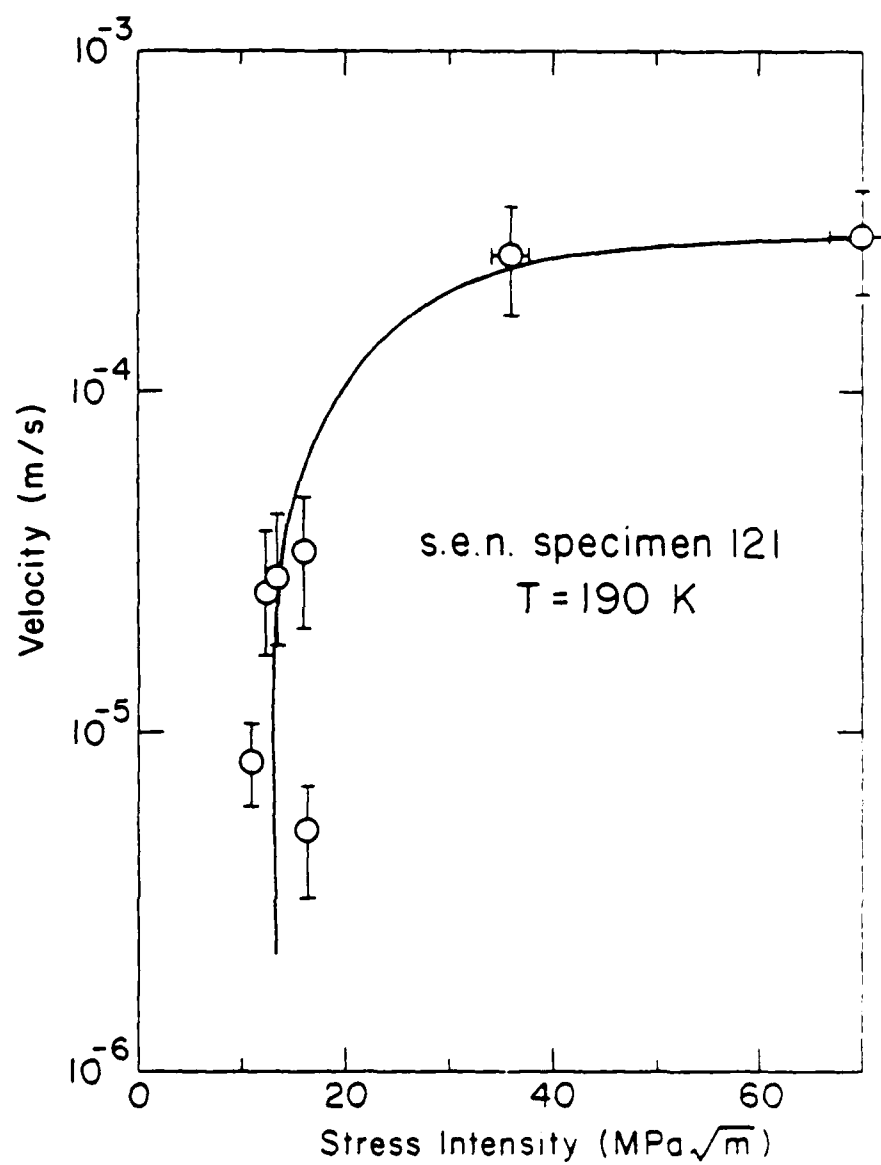


Fig. 11. Crack velocity versus  $K_I$  for s.e.n. specimen 121 tested at 190 K and  $H/Nb = 0.5\%$ .

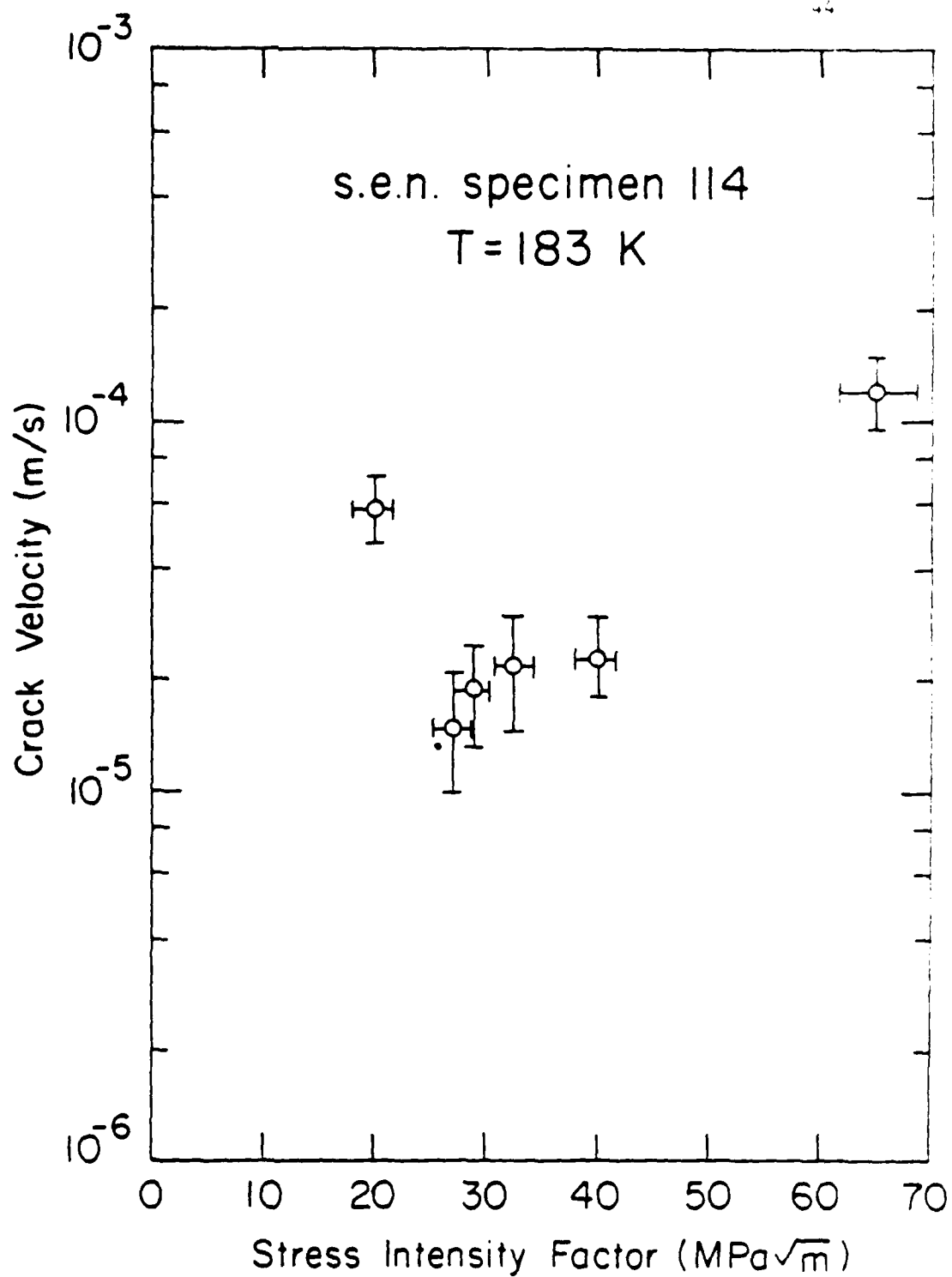


Fig. 12. Crack velocity versus  $K_I$  for s.e.n. specimen 114 tested at 183 K and  $\text{H/Nb} = 0.178\%$ .

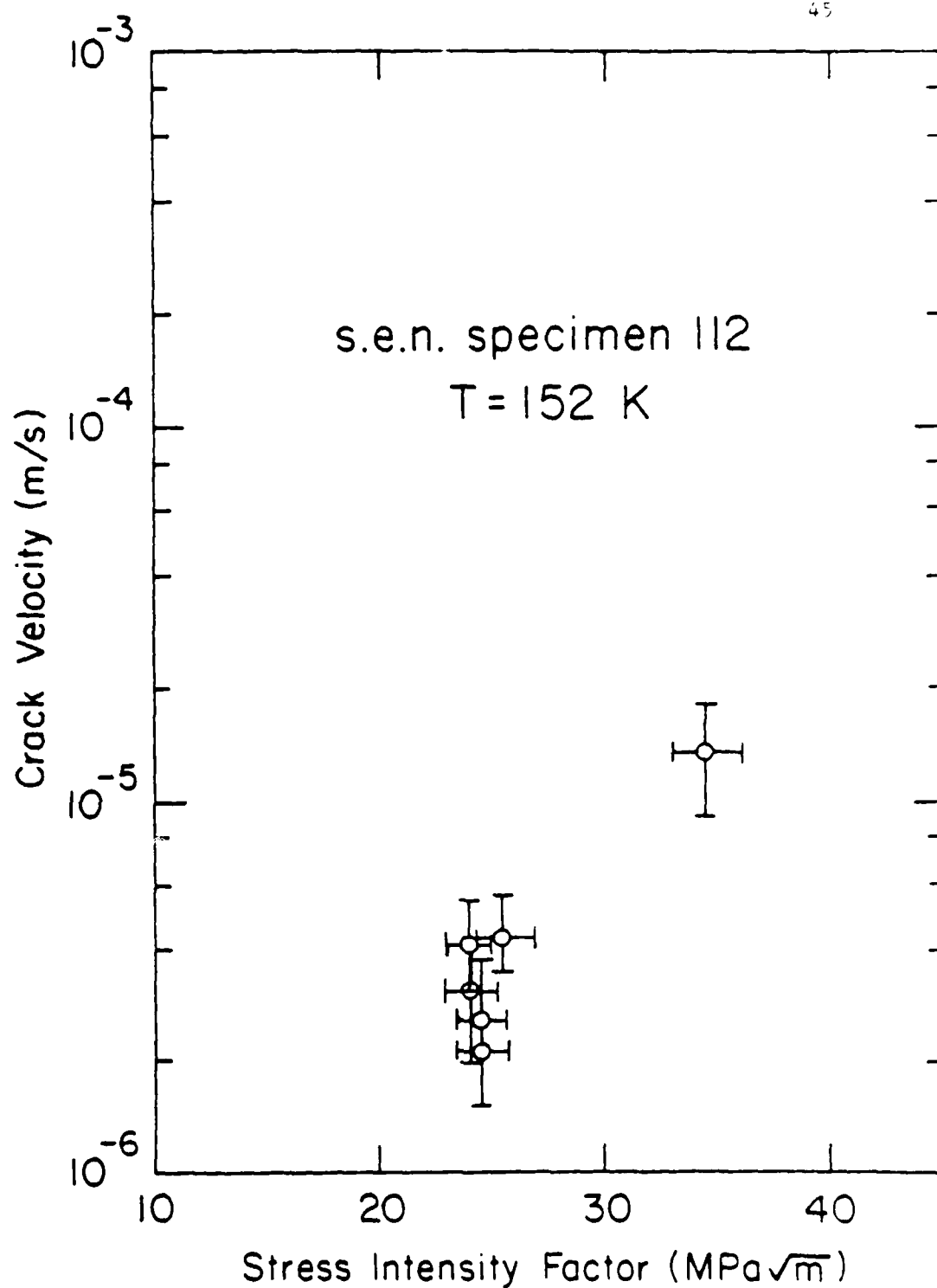


Fig. 13. Crack velocity versus  $K_I$  data for s.e.n. specimen 112 tested at 152 K and  $H/Nb = 0.068\%$ .

defined by the available data, they do exhibit Stage I and II behavior with  $V$  in Stage II decreasing as the test temperature decreases.

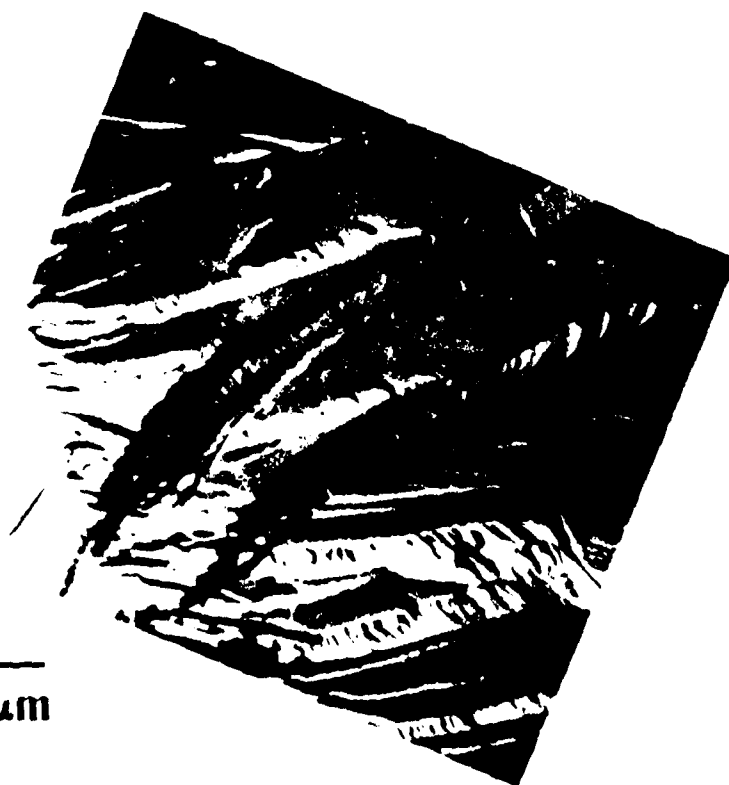
### 5.1.2 Fractography

A detailed examination of the fracture surfaces for hydrogen embrittled s.e.n. specimens has been presented by Grossbeck.<sup>(12)</sup> Fracture surface features for s.e.n. tests in this study are shown in Figs. 14-19 and are in excellent agreement with his results. All of the fracture surfaces at low strain rates exhibited brittle transgranular cleavage. At higher strain rates, ductile necking occurred as the crack tip outran the hydrogen diffusing toward it. Fig. 14 shows the fracture surface for specimen 119 for which the crack propagated from left to right. Fig. 15 is a higher magnification of the right side of Fig. 14. The existence of splinters on the fracture surface are quite prominent and they have been positively identified as niobium-hydride by electron diffraction analysis.<sup>(12)</sup> Fig. 16 is the fracture surface of specimen 114 showing the inscribed reference lines on the specimen's surface as well as splinters on the fracture surface. The presence of grain boundaries on these fracture surfaces is very clear as shown in Fig. 17 which is a higher magnification of the grain boundary appearing in Fig. 16. Similar features are shown in Fig. 18 which shows part of the fracture surface of specimen 121 and Fig. 19 which shows the inscribed reference lines on the surface of specimen 121 after fracture. It is clear that the lines had no effect on the propagating crack.



250  $\mu\text{m}$

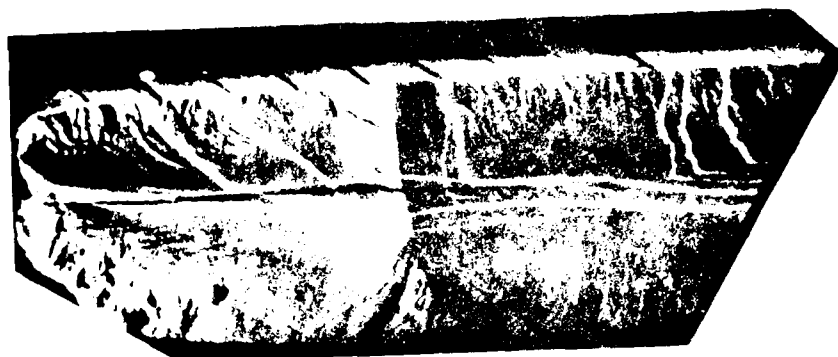
Fig. 11. Fracture surface of steel specimen 119. Three grains are visible. Crack propagated from left to right.



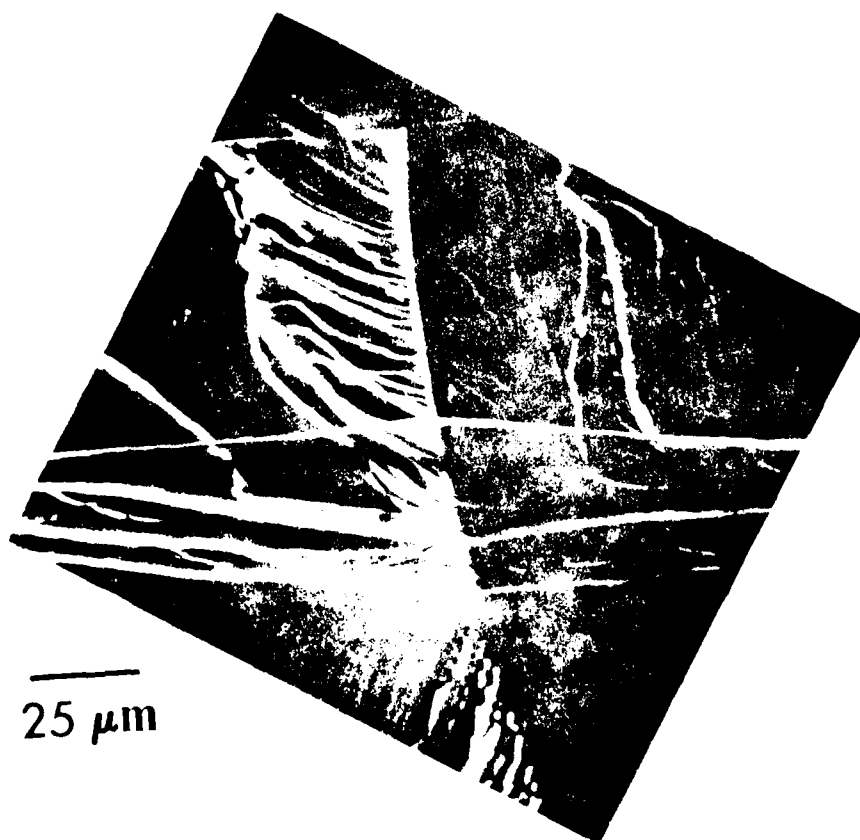
50  $\mu\text{m}$

Fig. 16. Fracture surface of s.e.n. specimen 114. Inscribed reference lines are visible on specimen's top surface. Crack propagated from right to left.

Fig. 17. Higher magnification of grain boundary appearing in center of Fig. 16 showing long horizontal splinter. River lines occur everywhere on the fracture surface.



—  
250  $\mu\text{m}$

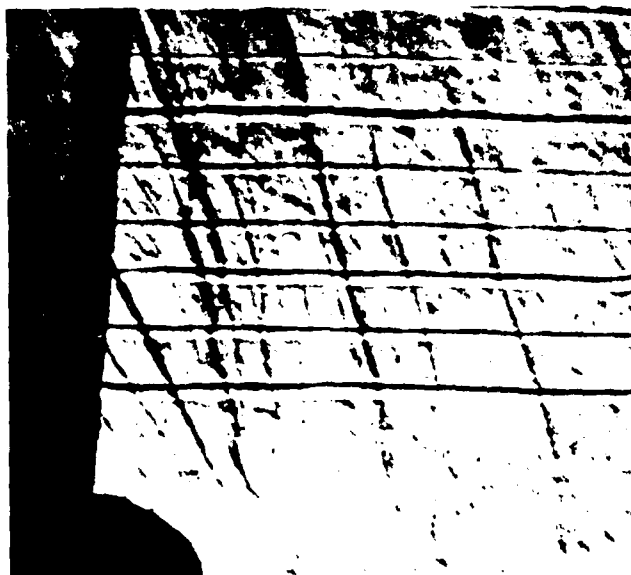


—  
25  $\mu\text{m}$



50  $\mu\text{m}$

Fig. 18. Fracture surface of s.e.n. specimen 121. Splinters appear in various sizes everywhere on the fracture surfaces. Pronounced cleavage steps are evident.



A

100  $\mu\text{m}$

Fig. 19. Inscribed reference lines on surface of s.e.n. specimen 121 after fracture. Notch (A) can be seen in lower left. Slip lines can be observed to obliquely intersect the reference lines.



## 5.2 Double Torsion Data

### 5.2.1 Compliance Measurements

Figures 20 and 21 show the results of the compliance measurements at 77 and 273 K, respectively. The linearity of the measured compliance data is further evidence for the validity of the analytical relationships derived in the Theory section. At both temperatures, however, it can be seen that the theoretical values for  $(dC/da)$  are greater than the experimentally determined values and do not extrapolate to the origin. Using Eqn. (17), the ratios of the theoretical and experimental  $K_I$  values can be calculated. At 77 K, it was found that

$$(K_{\text{theory}}/K_{\text{meas.}})_{T = 77} = 1.14 \quad (26)$$

and at 273 K,

$$(K_{\text{theory}}/K_{\text{meas.}})_{T = 273} = 1.09 \quad (27)$$

Ideally, these ratios should be unity. To correct for these slight discrepancies between  $K_{\text{theory}}$  and  $K_{\text{meas.}}$ , an average correction factor of

$$(1.14 + 1.09)/2 = 1.12 \quad (28)$$

was used to multiply the measured  $K_I$  values for all d.t. tests.

The least squares line for the measured compliance was seen to have a positive y-intercept. This has been observed in steel<sup>(23)</sup> and polymethylmethacrylate<sup>(39)</sup> and was found to be a function of the

Fig. 20. Double torsion specimen compliance as a function of crack length for calculated and measured values at 77 K. Solid line is least squares fit for measured data.

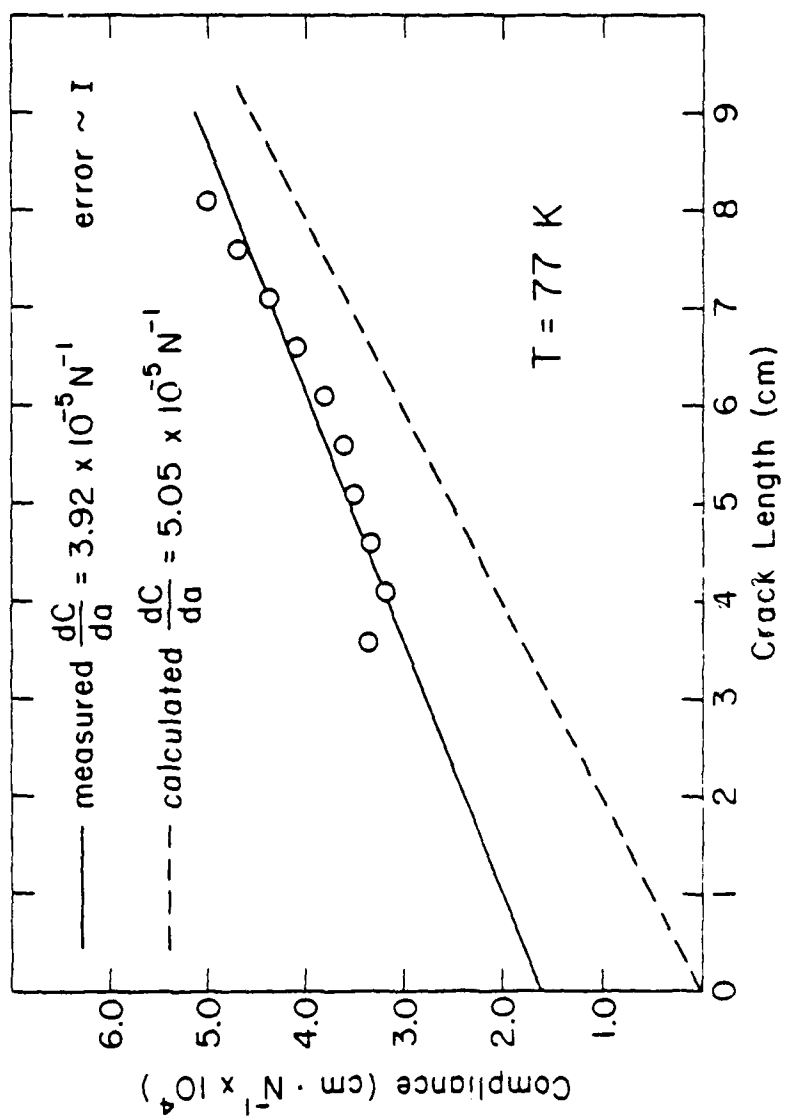
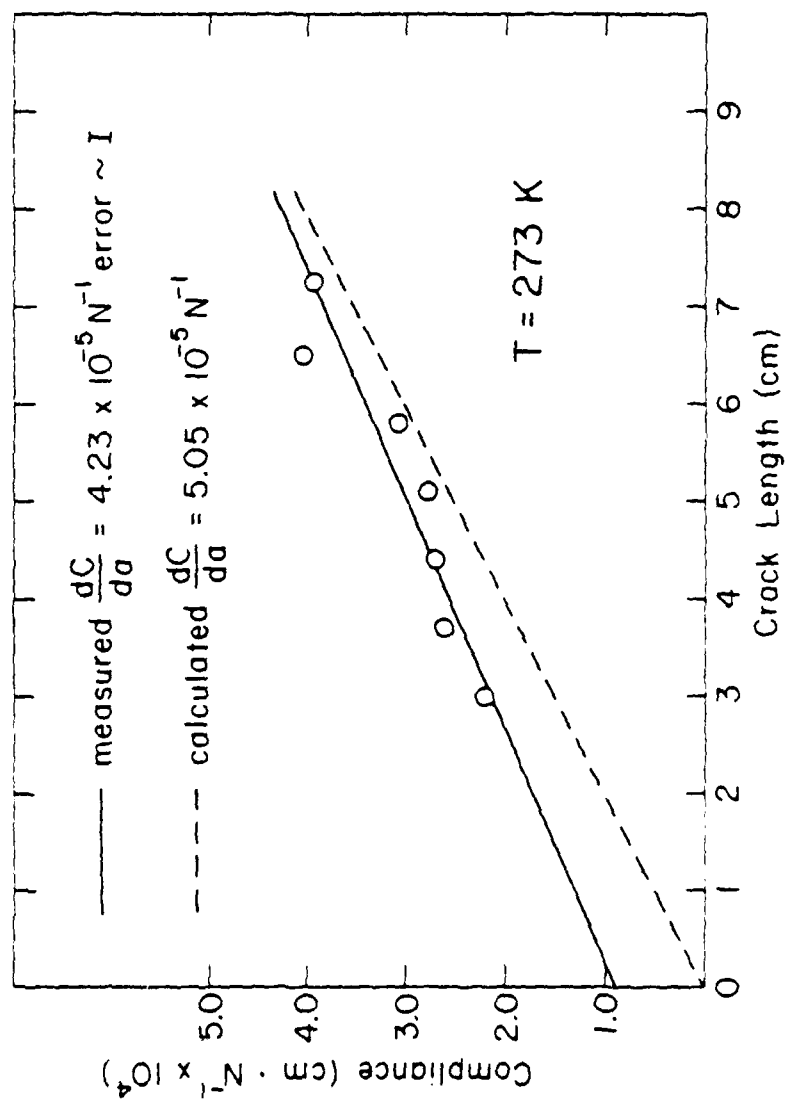


Fig. 21. Double torsion specimen compliance as a function of crack length for calculated and measured values at 273 K. Solid line is least squares fit for measured data.



specimen's elastic properties and dimensions but independent of the crack length.<sup>(40)</sup> This is of little consequence so long as the initial notch length is greater than half the specimen's width. Crack lengths are measured from the edge and since an initial notch length of 3 cm was machined into each d.t. specimen, only data for crack lengths greater than this minimum value are shown.

### 5.2.2 Constant Deflection (Decreasing $K_I$ )

The constant deflection method represents decreasing  $K_I$  tests. As derived in the Theory section, the initial load is proportional to the maximum  $K_I$  for each test and subsequent load relaxations corresponds to the decreasing  $K_I$ . These results are divided into high, low and intermediate temperature ranges which must be related to the specimen solvus. The high temperature range for the specimen's studied is between 220 K and 303 K. Specimens in this range have been tested at or above their solvus. The low temperature range is between 77 K and 148 K which corresponds to specimens tested below their solvus and having a very small amount of hydrogen remaining in solid solution. Specimens tested in the intermediate temperature range, 148 K to 220 K, were slightly above or below their solvus but still had a significant amount of hydrogen in solid solution. Table 6 lists the conditions for these decreasing  $K_I$  tests.

#### 5.2.2.1 High Temperature (V-K) Curves

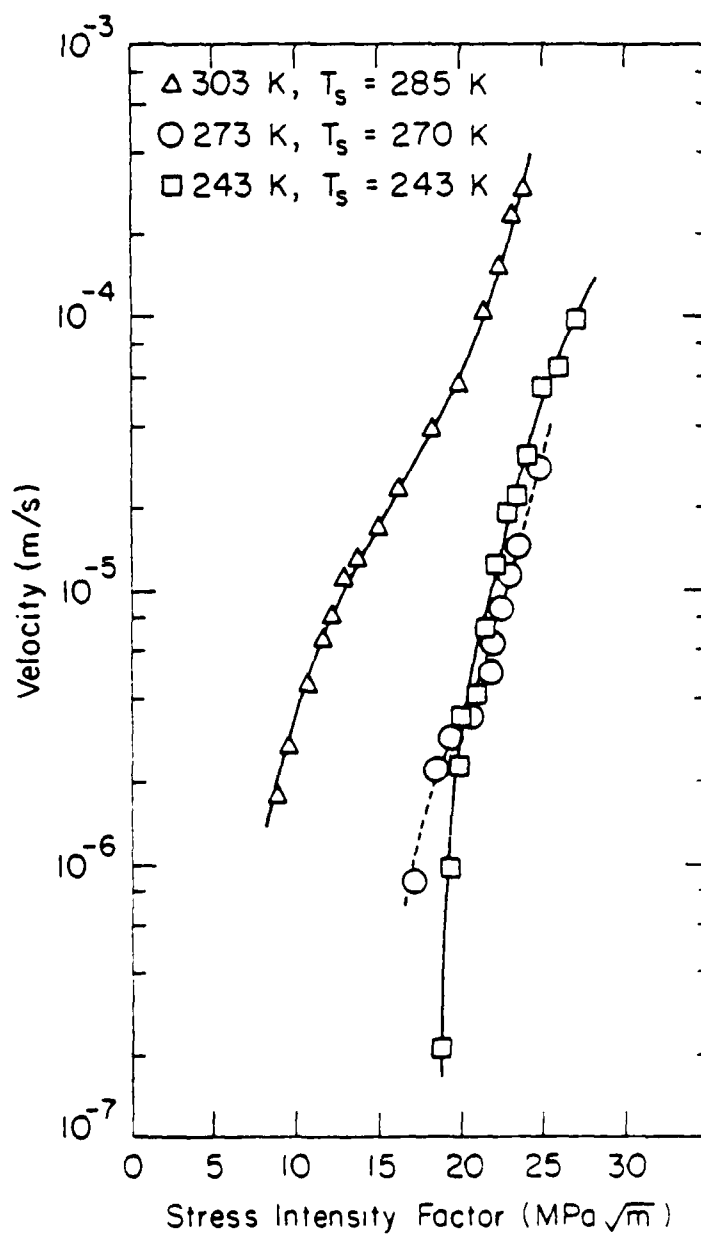
Figure 22 shows the results for several tests in the high temperature region. Maximum  $K_I$  values achieved during the tests.

TABLE 6  
Double Torsion Decreasing  $K_I$  Test Conditions

Temperature Range ( K )	Hydrogen Concentration In Solid Solution At Test Temperature ( at. % )	Hydrogen Concentration In Hydride Form Prior To Loading ( at. % )	Stress Free Solvus Temperature ( K )	Test Temperature ( K )	Specimen
77-148 (Low)	$6.4 \times 10^{-6}$	0.3	193	77	49
	0.0017	0.46	208	112	55
148-222 (Intermed.)	0.03	1.27	243	148	23
	0.03	1.27	243	148	25
	0.30	none	197	215	41
	0.46	none	205	218	53
	0.46	none	205	221	54
222-203 (High)	1.3	none	243	243	24
	2.3	none	270	273	19
	3.0	none	285	303	20

Fig. 22 Crack velocity versus  $K_I$  curves for d.t., high temperature, decreasing  $K_I$  tests.





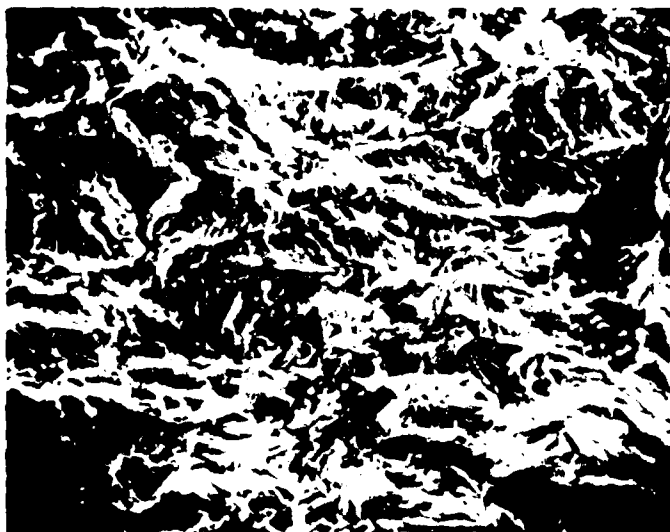
ranged from 22.5 to 27.5 MPa  $\cdot$  m<sup>1/2</sup>. These tests were characterized by a strong dependence of V on  $K_I$  and while the data suggests a three stage curve the constant Stage II extended only over a very limited range of  $K_I$  values. The three stage character of the curves are most evident in the data at 303 and 273 K which were taken slightly above their respective solvus temperatures. The threshold  $K_I$  values decreased while the Stage II velocities increased as the temperature increased. The 243 K data showed a further increase in  $K_{I0}$  but these data taken at the solvus temperature did not exhibit a three stage curve. The stress intensity threshold varied from 8 to 18 MPa  $\cdot$  m<sup>1/2</sup> over the temperature range 303 to 243 K and the maximum velocity measured was  $4 \times 10^{-4}$  m/s.

#### 5.2.2.2 High Temperature Fractography

Fracture surfaces for the high temperature tests are characterized by predominant brittle failure accompanied by some ductile tearing as shown in Figs. 23 and 24 where significant amounts of secondary cracking can also be observed. The occurrence of ductile tearing did not vary appreciably with  $K_I$ . These features occur along the entire fracture surfaces.

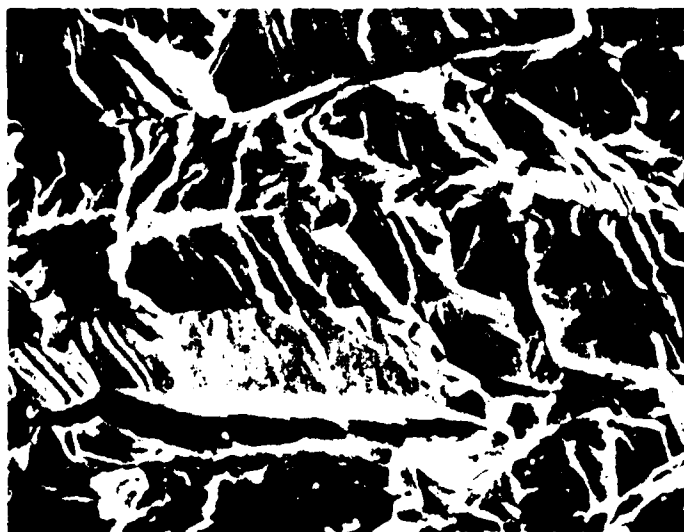
#### 5.2.2.3 Low Temperature (V-K Curves)

Tests at 77 K for the low temperature region are shown in Fig. 25. At 77 K, the data are characterized by crack velocities which are even more strongly dependent on  $K_I$  than the high temperature (V-K) data. The  $K_I$  values attainable are a factor of two to three times



100  $\mu\text{m}$

Fig. 23. Fractured surface after a 1 hr temperature decreasing  $S_{\text{p}}$  test. The cleavage fracture and/or cleavage is evident along with shear and/or secondary cracking.



10  $\mu\text{m}$

Fig. 24. Detail of the crack tip in the center area in Fig. 23, showing secondary cracks. The direction of the secondary cracks is visible along the direction of the primary crack.

greater than those for the high temperatures. Data taken at 77 K with the decreasing  $K_I$  tests appear to depend on the initial  $K_I$  values for each test, i.e. the (V-K) data was multivalued. As seen in Fig. 25, the velocities observed lay in the range  $10^{-5}$  to  $10^{-7}$  m/s for  $K_I$  values between 30 and 70  $\text{MPa} \cdot \text{m}^{1/2}$  and formed three separate curves for the three tests carried out. In this temperature range it is evident that (V-K) data may be compared only when tests (and particularly the initial  $K_I$  values) are carried out under identical conditions. All three 77 K (V-K) curves had identical slopes. The dependence of the data on the initial  $K_I$  value precludes any discussion of threshold stress intensities.

Figure 26 shows results comparing (V-K) curves for deuterium and hydrogen charged specimen tested under identical conditions and an initial  $K_I$  value of 32.5  $\text{MPa} \cdot \text{m}^{1/2}$  at 77 K. The curves are functionally identical except the crack velocities from the deuterium charged specimen are a factor of approximately 15 less than the crack velocities of the hydrogen charged specimen at equal  $K_I$  values. Comparison with the expected crack velocity differences between hydrogen and deuterium charged specimens will be presented in the Discussion section.

The results shown for 112 K in Fig. 25 are significantly different than for 77 K. Stress intensity values less than 46  $\text{MPa} \cdot \text{m}^{1/2}$  for the 112 K data are unavailable due to the specimen's failure at that point. The 112 K (V-K) curve resembles the (V-K) behavior of the intermediate temperature tests to be presented shortly.

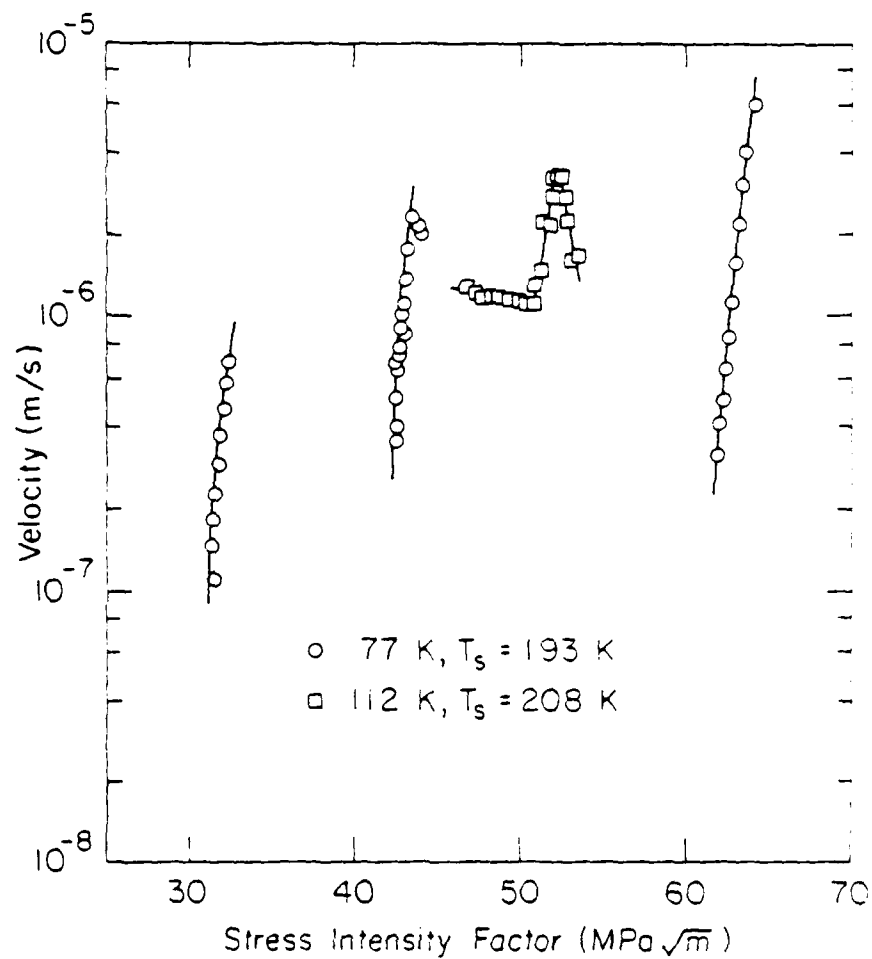


Fig. 25. Crack velocity versus  $K_I$  curves for d.t., low temperature, decreasing  $K_I$  tests.

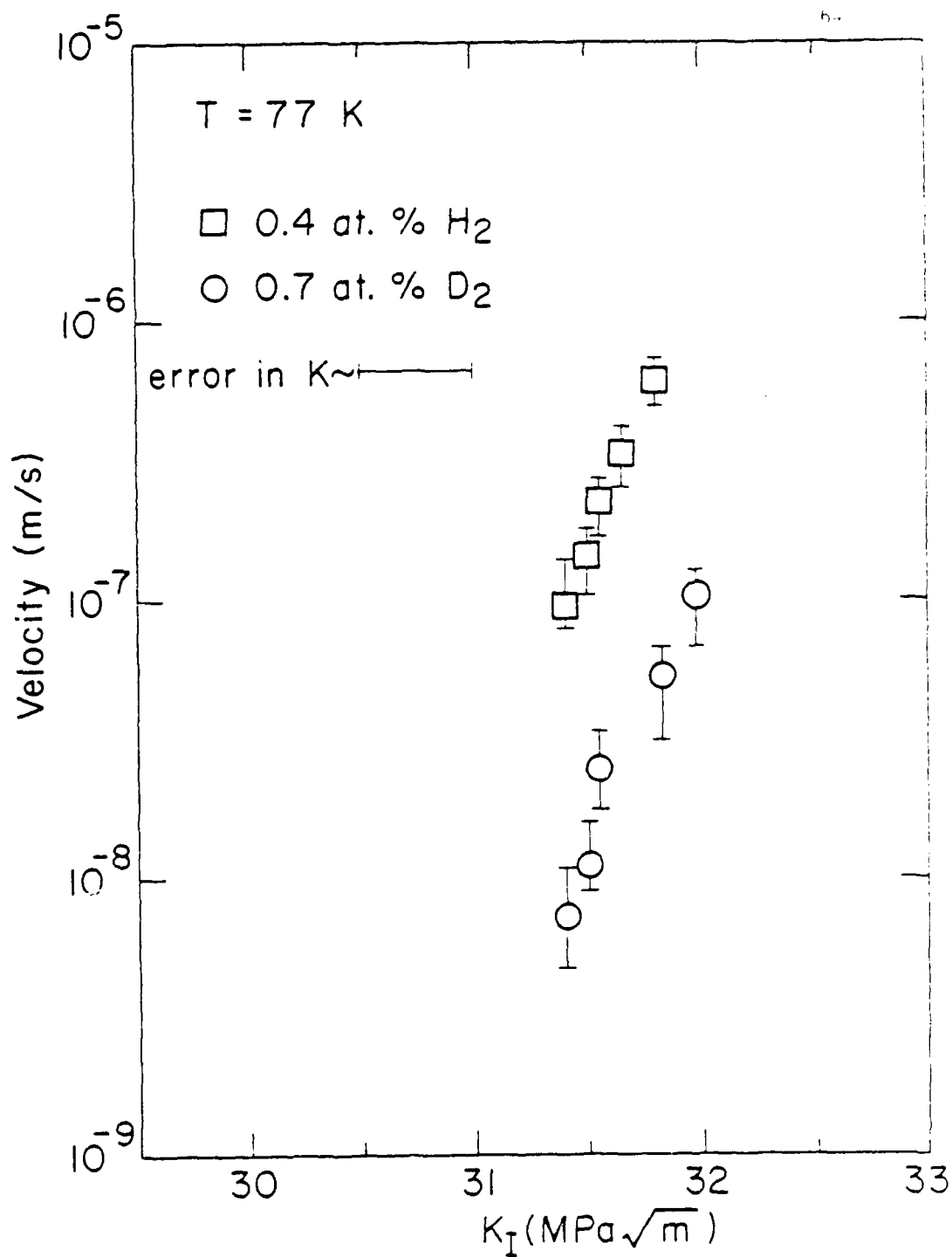


Fig. 26. Crack velocity versus  $K_I$  showing differences in crack velocities between hydrogen and deuterium charged d.t. specimens.

#### 5.2.2.4 Low Temperature Fractography

All low temperature specimens exhibited crystallographic transgranular cleavage for all values of  $K_I$ . Figures 27 and 28 show the fracture surface for the deuterium charged specimen. Secondary cracking was generally not observed. Presence of some microvoid coalescence as well as river patterns can be observed as is consistent with the low hydrogen diffusivity at 77 K. Hydrogen charged specimens tested at 77 K exhibit identical fracture surface features as the deuterium charged specimens as shown in Figs. 29 and 30.

#### 5.2.2.5 Intermediate Temperature (V-K) Curves

Crack velocity versus  $K_I$  curves for intermediate temperatures shown in Figs. 31-35 are strikingly different from both the high and low temperature data. In general, the (V-K) dependence is not monotonic but exhibits a decrease in V and  $K_I$  decreases followed by an increase to a maximum and a further decrease in V with decreasing  $K_I$  values. This behavior is observed both above and below the solvus temperatures in this intermediate temperature range.

Figure 31 shows the (V-K) curves for 218 K at  $H/Nb = 0.46$  and acoustic emission intensity for the propagating crack versus  $K_I$ . Acoustic emission intensity is seen to be almost directly proportional to V. Acoustic emission from an uncharged specimen used in the plasticity correction (section 4.3.2.2) was no greater than 300 counts/min which is several orders of magnitude less than a.e. intensities from the propagating crack. Fig. 32 is a simplified presentation of the



250  $\mu\text{m}$

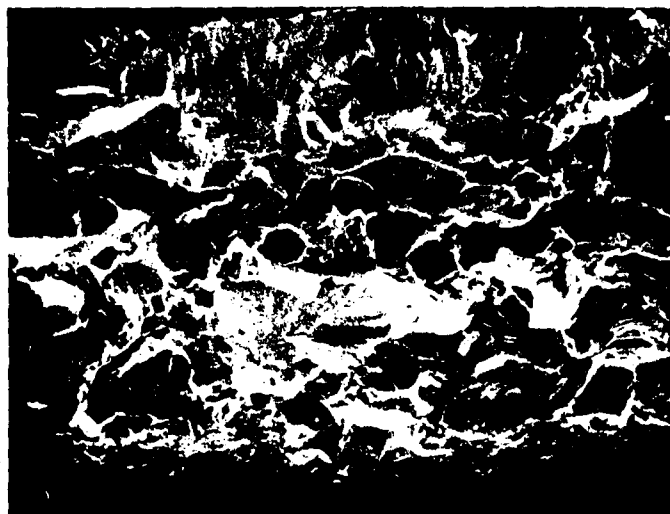
Fig. 27. Fracture surface of deuterium charged d.t. specimen fractured at 77 K. Pronounced crystallographic cleavage is visible. Area below the arrows is the surface of the machined groove on the bottom of the specimen.



50  $\mu\text{m}$

Fig. 28. Higher magnification of the center area in Fig. 27. Microvoid coalescence can be observed on the edge of the larger cleavage steps.





250  $\mu\text{m}$

Fig. 29. Fracture surface of hydrogen charged d.t. specimen fractured at 77 K. Area below arrows is the surface of the machined groove on the bottom of the specimen.



50  $\mu\text{m}$

Fig. 30. Higher magnification of the fracture surface in Fig. 29. Fracture surface features identical to the deuterium charged specimen shown in Fig. 28 can be seen.

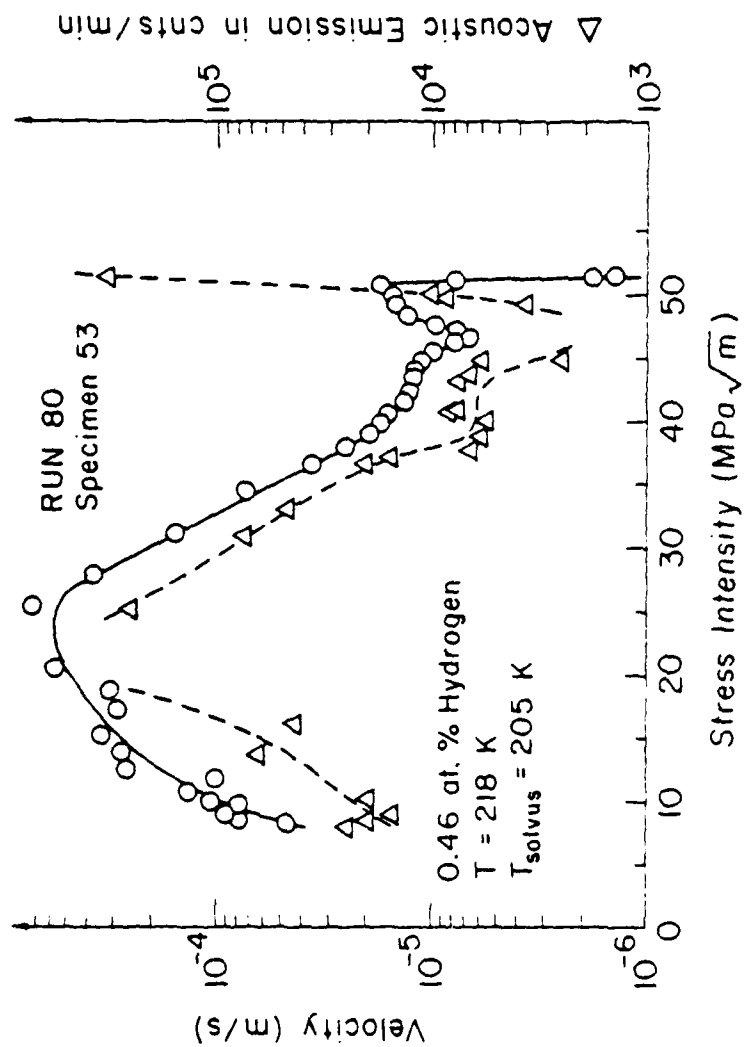


Fig. 31. Crack velocity and acoustic emission versus  $K_I$  for d.t. specimen 53 at 218 K and  $H/Nb = 0.46\%$ .

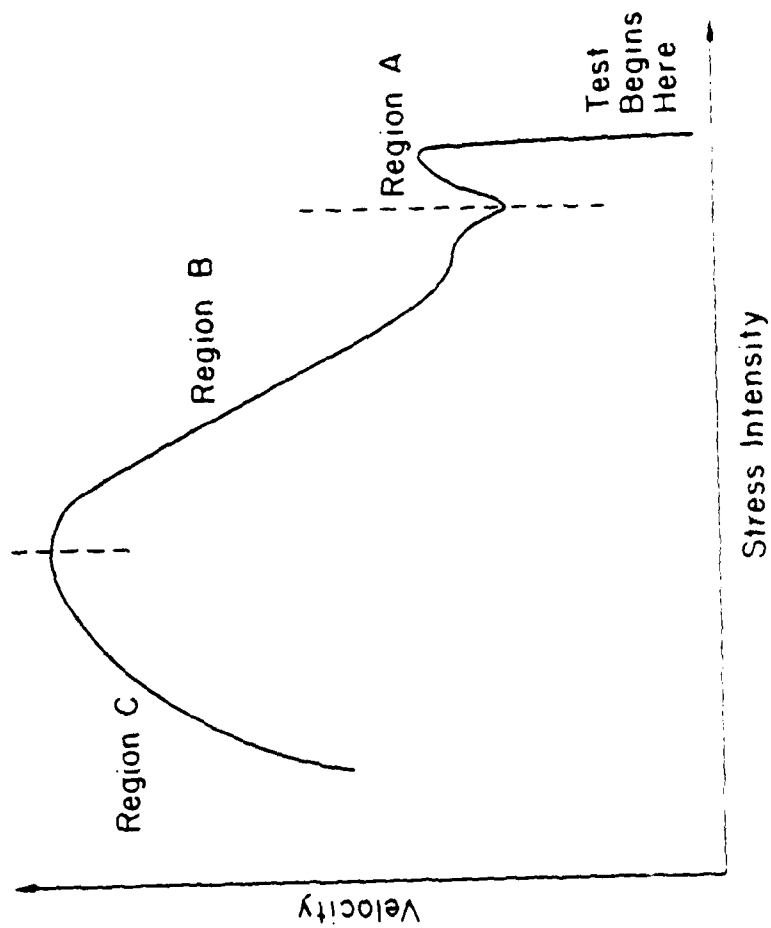


Fig. 32. Crack velocity versus  $K_I$  of Fig. 31 showing three region behavior of decreasing  $K_I$  tests for intermediate temperatures.

(V-K) curve in Fig. 31. Three regions are labeled A, B and C which are characteristic of the intermediate temperature results. Since these results are from decreasing  $K_I$  tests, Region A is observed immediately after the Instron crosshead is stopped and is characterized by a decrease in V to a local minimum. Specimen 53 for which the crack was initiated at the highest stress intensity, Fig. 32, shows an additional feature of an initial increase in V before the local minimum occurs. This initial increase in V should occur for all decreasing  $K_I$  tests since the initial V must start at zero. With the exception of specimen 53, the plastic correction procedure described in section 4.3.2.2 prevented the initial V to be resolved in the other decreasing  $K_I$  tests. Region B corresponds to an increase in V with decreasing  $K_I$ . Crack velocity increase was measured to range from a factor of three to almost two orders of magnitude. Region C is characterized by a sharp decrease in V with decreasing  $K_I$  where V continues to decrease to values beyond the limit of measurement.

Figure 33 shows the (V-K) curves for two specimens tested at 95 K below their solvus temperatures and having identical hydrogen concentrations. Reproducibility of data at low  $K_I$  values is shown to be excellent. Crack initiation occurred at 30 and 40  $\text{MPa} \cdot \text{m}^{1/2}$  for these two specimens. During Region B, V increased by almost two orders of magnitude. Figure 34 shows the (V-K) curves for two specimens having identical hydrogen concentrations and tested at either 13 or 18 K above their solvus temperatures. Regions A and C in this figure are quite similar to Regions A and C of Figs. 32 and 33. Region B of Fig. 34, however, shows only an increase of a factor of three in V

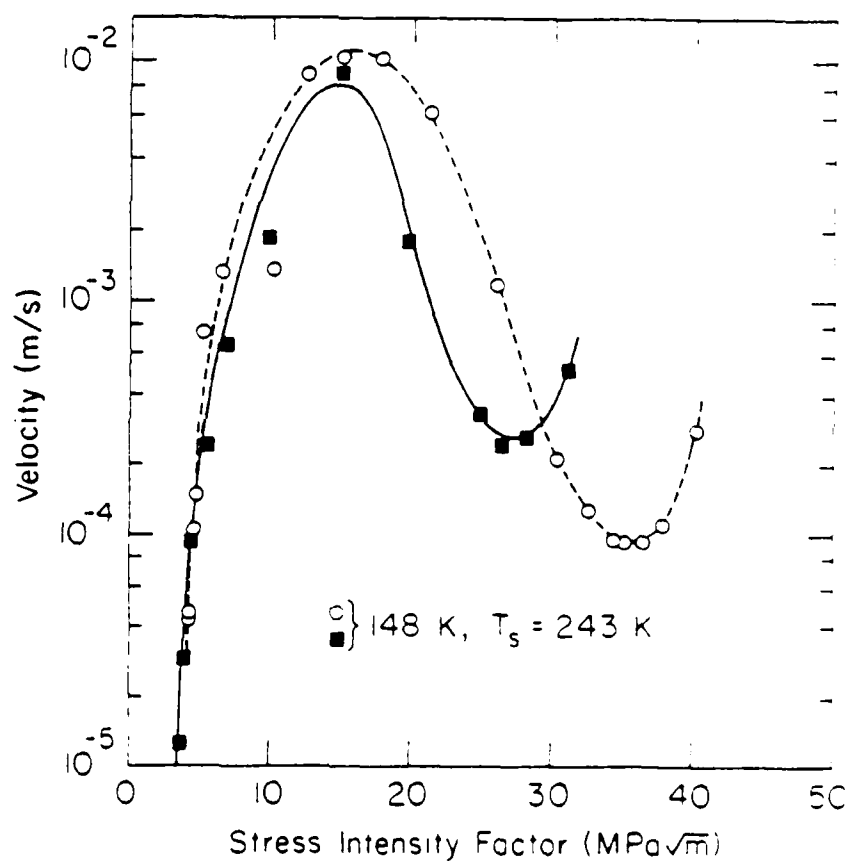


Fig. 33. Crack Velocity versus  $K_I$  curves for i.t. specimens 23 (circles) and 25 (solid squares) tested at 148 K showing three region behavior.

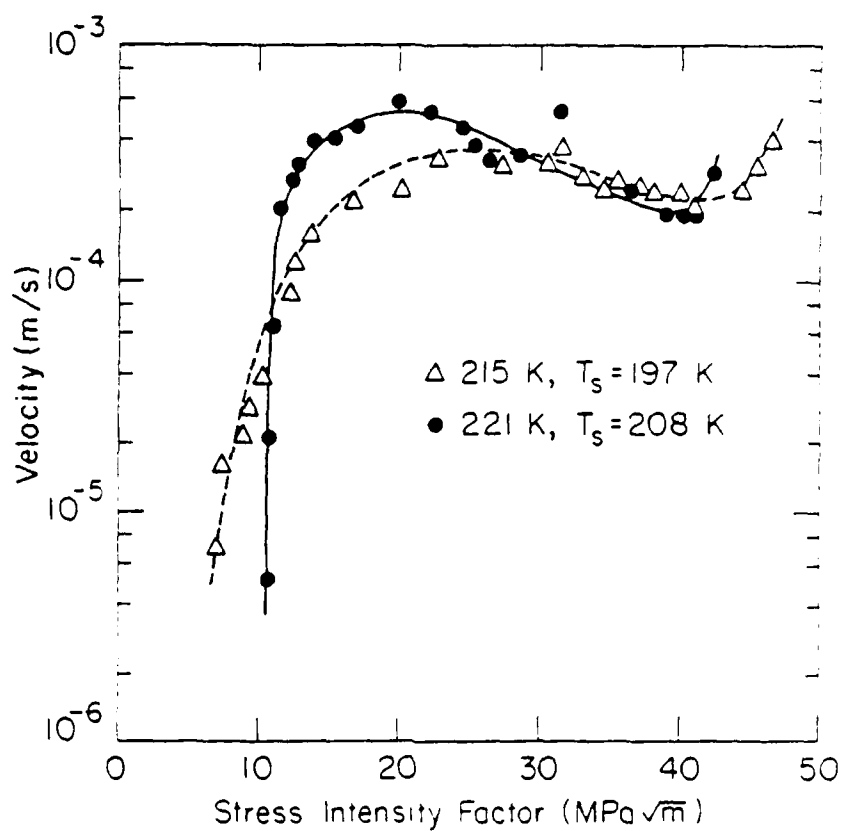


Fig. 34. Crack velocity versus  $K_I$  curves for d.t. specimen 41 (triangles) and 54 (solid circles) showing three region behavior.

before Region C is reached. Figure 35 shows all the intermediate temperature data plotted on one graph for comparison.

#### 5.2.2.6 Intermediate Temperature Fractography

Fracture surface features of the intermediate temperature range tests reflected the behavior of the three region (V-K) curves. Figure 36 shows the notch area where cracking was initiated in Region A. The fracture surface was predominantly transgranular cleavage with a substantial amount of secondary cracking. The area on the fracture surface near the top surface of the specimen exhibits some ductile shearing. Figure 37 is the center area of Fig. 36 at higher magnification and shows the presence of brittle fracture along with some ductility. The bottom area of the fracture surface, near the groove, shows only brittle failure with a multitude of river lines as shown in Fig. 38.

Fracture surfaces corresponding to Region B behavior exhibited predominantly cleavage with a greater amount of ductile fracture than Region A as shown in Fig. 39. The center and bottom area of the fracture surface corresponding to Region B also shows a significant amount of secondary cracking. Figures 40 and 41 show the transition region between ductile and brittle fracture in Region B at high magnification. These figures also show the existence of small slip steps on the rumpled shear surfaces. The ductile shear area was not entirely without brittle cracks. Figures 42 and 43 show another area corresponding to Region B which clearly shows the presence of both ductile and brittle fracture along with secondary cracking.

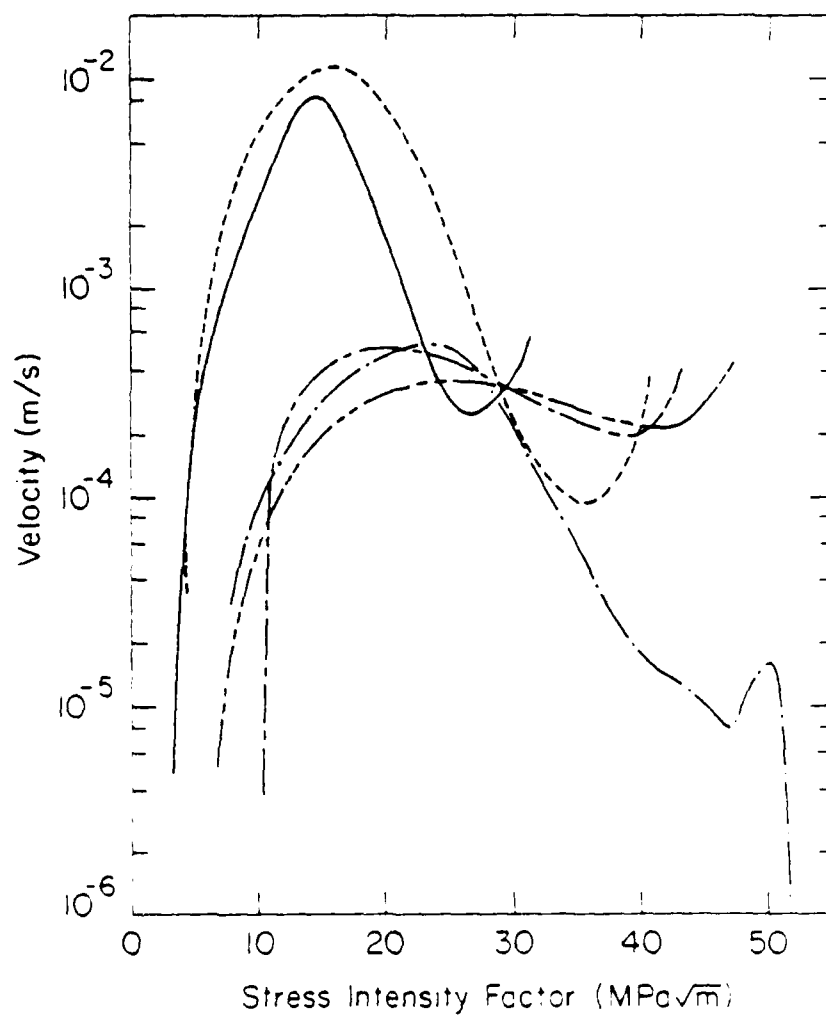


Fig. 35. Crack velocity versus  $K_I$  for all d.t., decreasing  $T$ , intermediate temperature tests showing specimens 25 (\_\_\_\_), 25 (\_\_\_\_), 41 (\_\_\_\_), 53 (\_\_\_\_) and 54 (\_\_\_\_).



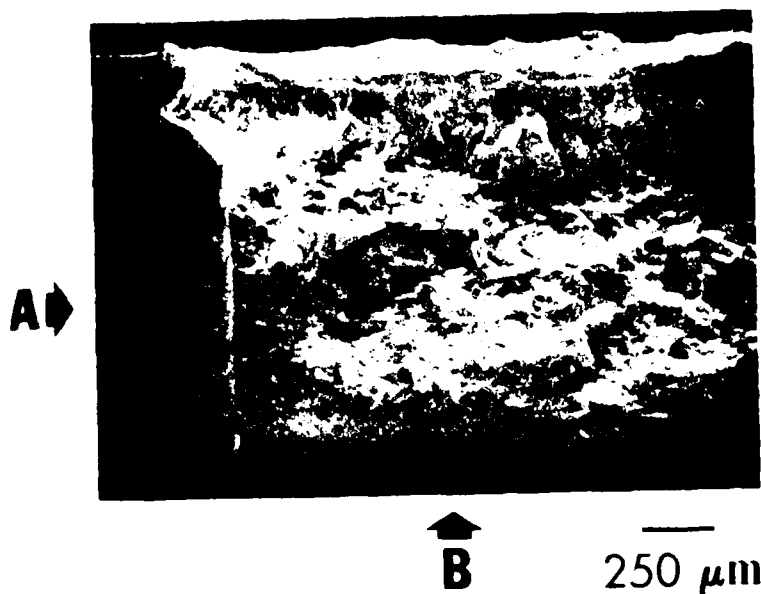


Fig. 36. Fracture surface resulting from Region A behavior near specimen's notch (A). Bottom arrow (B) indicates direction of crack growth. Top of specimen exhibits ductile tearing on fracture surface.



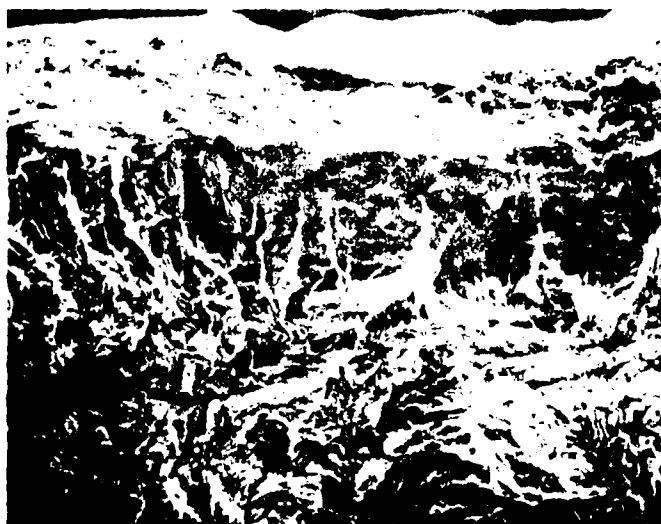
Fig. 37. Close-up of fracture surface showing ductile tearing. Top of specimen exhibits ductile tearing on fracture surface.

Fig. 38. Fracture surface resulting from Region A behavior near the bottom groove (below arrows). Predominance of river lines are visible.

Fig. 39. Fracture surface resulting from Region B behavior showing top of d.t. specimen. Significant amount of ductile tearing can be seen as well as secondary cracking.



100  $\mu\text{m}$



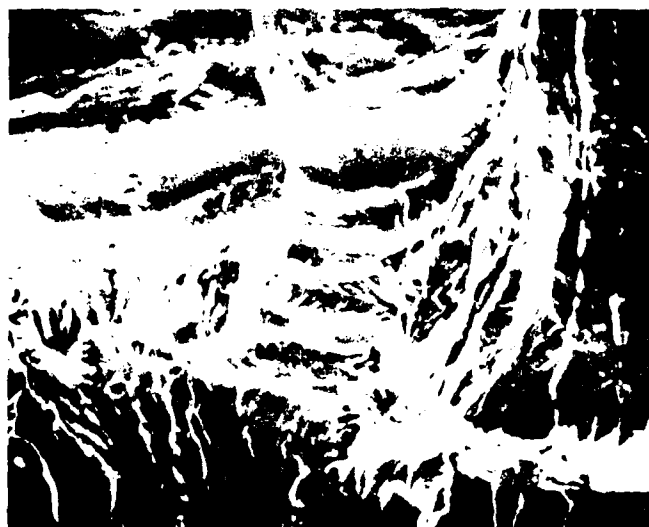
100  $\mu\text{m}$



100  $\mu\text{m}$

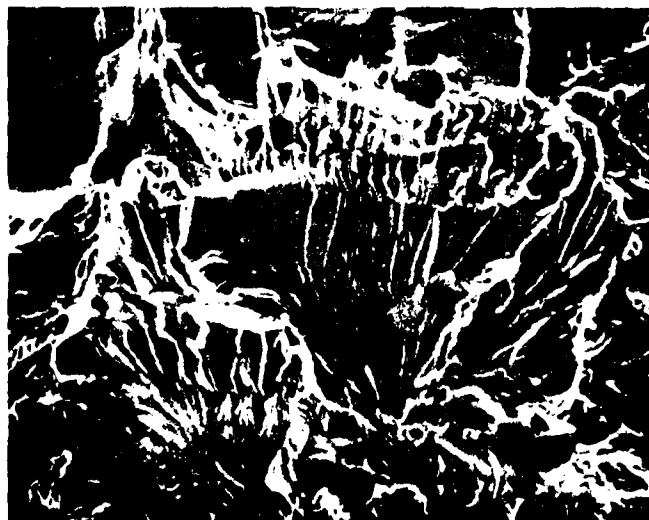


100  $\mu\text{m}$



25  $\mu\text{m}$

Fig. 40. Fracture surface resulting from Region B behavior showing transition from brittle fracture to a roughed ductile shearing near the top of the specimen. Slip steps can be seen on the ductile surface.



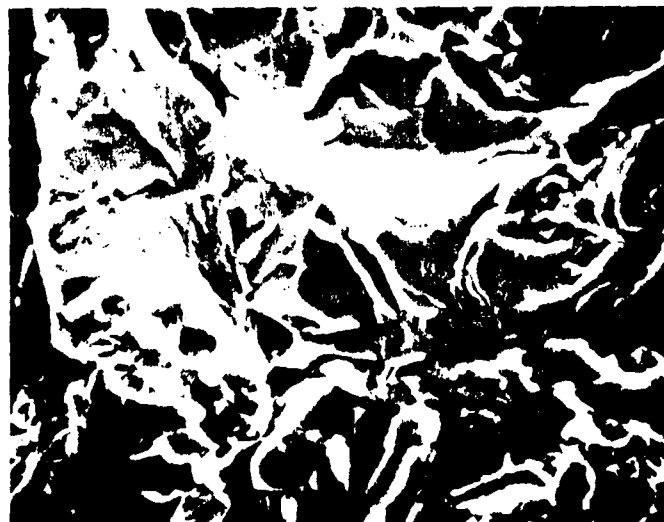
25  $\mu\text{m}$

Fig. 41. Another view of the transition from brittle failure to ductile shearing on the fracture surface resulting from Region B behavior. Secondary cracks are visible in the brittle zone as well as cleavage steps.



10  $\mu\text{m}$

Fig. 42. Secondary crack occurring in ductile shearing zone on fracture surface resulting from Region B behavior.



10  $\mu\text{m}$

Fig. 43. Area on fracture surface resulting from Region B behavior, showing secondary cracking, cleavage steps and ductile tearing.

Region C behavior was typically characterized by brittle cleavage and the presence of river as shown in Fig. 44. In contrast to Regions A and B little evidence for ductile fracture was observed. Also visible in Fig. 44 are elongated grain boundaries along the rolling direction of the plate.

### 5.2.3 Constant Load (Constant $K_I$ ) Data

These results represent (V-K) data obtained from constant stress intensity tests as described in section 4.3.2.3. Crack propagation for constant  $K_I$  tests was significantly different from the decreasing  $K_I$  tests. The constant  $K_I$  data exhibited the familiar three stage velocities, mentioned in section 2.3, often seen in stress corrosion cracking.

#### 5.2.3.1 Constant $K_I$ (V-K) Curves

Table 7 lists the d.t. constant  $K_I$  test conditions and Fig. 45 shows the results for the constant  $K_I$  tests at four temperatures, 180, 218, 232 and 303 K. At the three highest temperatures, tests were carried out above the specimen's solvus temperatures while the 180 K test was carried out at 42 K below the specimen's solvus. Onset of rapid crack growth in Stage III was found to occur at  $K_{I0} = 1.2 \text{ MPa} \cdot \text{m}^{1/2}$  and independent of temperature or hydrogen concentration. A definite threshold stress intensity factor,  $K_{I0}$ , below which no crack velocity (within the limits of the measurement capability) could be measured appears to exist for all the temperatures examined. The value of  $K_{I0}$  decreased as the test temperature decreased in contrast to



25  $\mu\text{m}$

Fig. 44. Typical fracture surface of this from Region C (Fig. 1). Brittle crystalline cleavage is present. Cleavage plane boundaries in the upper left are visible.



TABLE 7  
Double Torsion Constant  $K_I$  Test Conditions

Hydrogen Concentration In Solid Solution At Test Temperature (at. %)	Hydrogen Concentration In Hydride Form Prior To Loading (at. %)	Stress Free Solution Temperature ( K )	Test Temperature ( K )
3.2	none	289	303
0.9	none	222	232
0.46	none	205	218
0.18	0.72	222	180

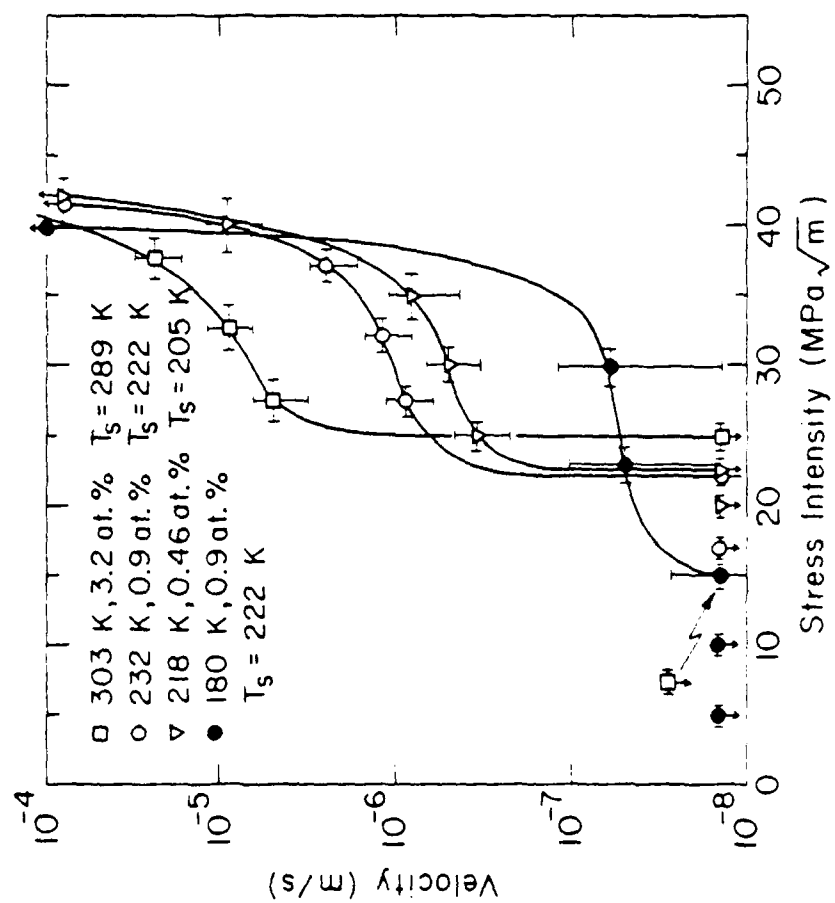


Fig. 45. Crack velocity versus  $K_I$  for all the constant  $K_I$  tests.

results obtained from the increasing  $K_I$  (s.e.n. data) and decreasing  $K_I$  tests. The threshold  $I_I$  values were  $25 \pm 1 \text{ MPa} \cdot \text{m}^{1/2}$  at 303 K,  $22.3 \pm 1 \text{ MPa} \cdot \text{m}^{1/2}$  at 232 and 218 K and  $15 \pm 1 \text{ MPa} \cdot \text{m}^{1/2}$  at 180 K. In Stage I,  $V$  was observed to increase by several orders of magnitude for an increase in  $K_I$  by only 4 or 5  $\text{MPa} \cdot \text{m}^{1/2}$ .

A definite Stage II constant ( $V$ - $K$ ) region was observed for all four temperatures. The velocities in Stage II decreased as the temperature decreased from about  $10^{-5} \text{ m/s}$  at 303 K to  $5 \times 10^{-8} \text{ m/s}$  at 180 K. The trend with temperature is the same as that observed for increasing  $K_I$  (s.e.n. data) and decreasing  $K_I$  curves but the velocity values are orders of magnitude lower for the constant  $K_I$  measurements.

#### 5.2.3.2 Constant $K_I$ Fractography

As mentioned in the Experimental Procedure section, all constant  $K_I$  d.t. specimens were fatigued prior to crack velocity measurements. The fatigue surface of d.t. specimen 51 and the fatigue boundary which is delineated by a white line is shown in Fig. 46. Figures 47 and 48 shows a higher magnification of the fatigue crack fracture surface which exhibits a predominance of ductile tearing as is expected. Figure 49 shows the interface between the fatigue crack and constant  $K_I$  test fracture surfaces. Brittle cleavage steps can be clearly seen on the side of the interface corresponding to the constant  $K_I$  crack propagation and ductile features are seen on the fatigue surface on the other side.

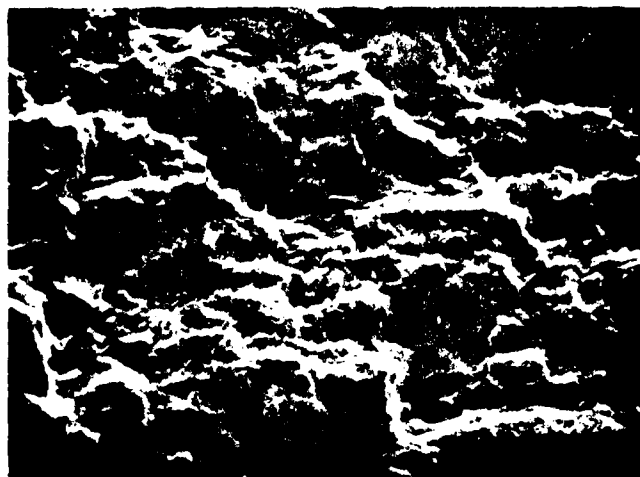
Fracture surface features for constant  $K_I$  specimens tested above and below their solvus temperatures differed slightly from one



1 mm

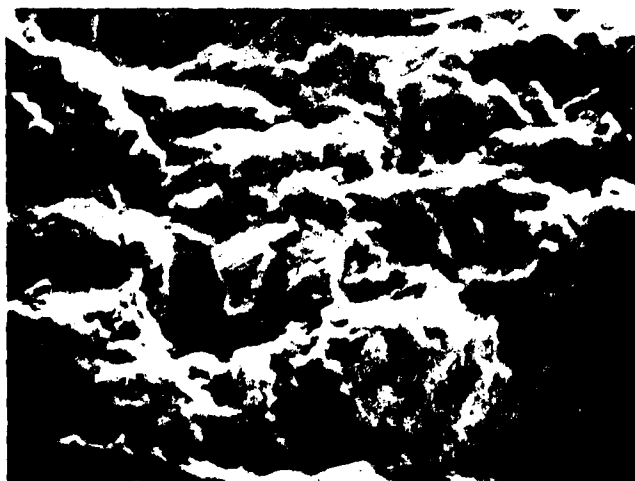
A B

The photograph shows a cross-section of a material, possibly a rock or sediment. The image is oriented vertically, with the top of the image corresponding to the left side of the page. The material is divided into two main layers by a horizontal line. The upper layer is dark and has a granular texture, while the lower layer is lighter and appears more uniform. A scale bar labeled "1 mm" is located to the right of the image. Arrows labeled "A" and "B" point to the left and right sides of the image, respectively.



25  $\mu\text{m}$

Fig. 47. Higher magnification of fatigue crack fracture surface of Fig. 46 showing predominance of ductile tearing.



10  $\mu\text{m}$

Fig. 48. Higher magnification of the center area in Fig. 47 showing ductile features in more detail.



10  $\mu\text{m}$

another. Figure 50 shows the fracture surface near the notch area for d.t. specimen 56 tested above its solvus. The top of the fracture surface shows the presence of some slight ductile shearing. The majority of the specimen's fracture surface exhibited transgranular cleavage with some ductile fracture, much secondary cracking and an abundance of river lines due to brittle cleavage steps which are shown at higher magnifications in Figs. 51 and 52. Figures 53 and 54 show the fracture surface for the specimen tested at 180 K which is 43 K below its solvus. Its fracture surface exhibited similar secondary cracking and the profusion of river lines similar to those shown by the specimens tested above their solvus temperatures. The specimen tested below its solvus did not, however, exhibit any of the ductile shearing that was present for specimens tested above their solvus.

#### 5.2.4 Critical Hydride Size

As mentioned in the Experimental Procedure section, an incubation interval, during which no crack propagation occurred, became apparent during the plastic correction procedure for measuring d.t. specimen crack velocities. A critical hydride size,  $l_c$ , before crack advance occurs, can be estimated by assuming stress assisted diffusion of hydrogen into the crack tip region. Under these conditions, a hydride will continue to grow until a critical size is reached where the local stress distribution exceeds the hydride's fracture stress and failure occurs.

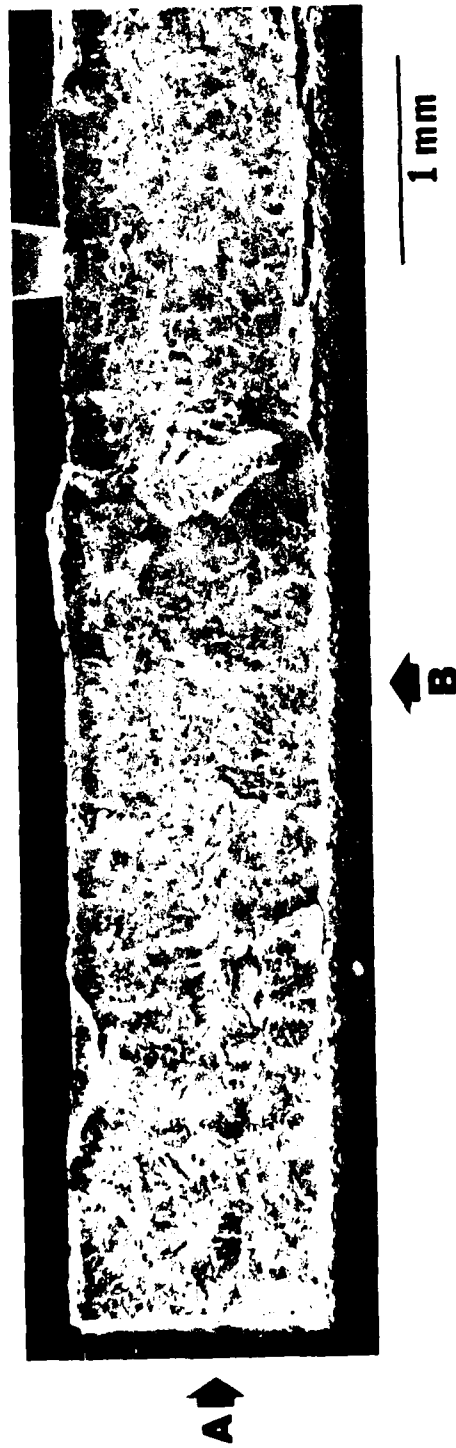


Fig. 2. Fracture surface of specimen to test at 215 K. Notch is shown by arrow (A) and bottom edge of specimen (B). Crack propagated from left to right.



Fig. 51. Typical fracture surface for constant load d.t. specimens tested above their solvus temperatures. Secondary cracks and river lines are visible.

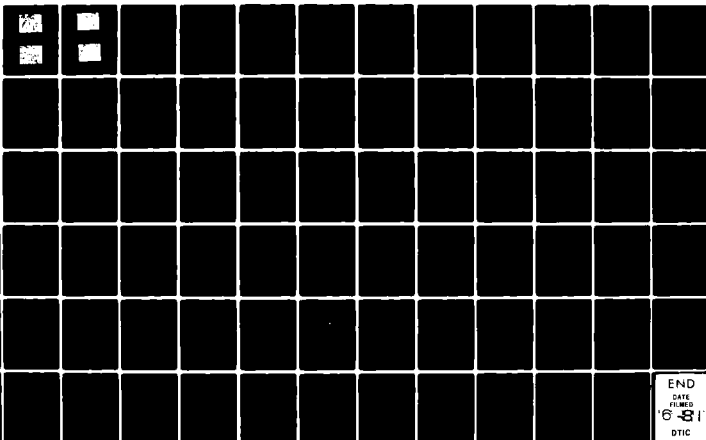
Fig. 52. Higher magnification of center area in Fig. 51 showing secondary cracks and cleavage steps in greater detail.

AD-A099 194 ILLINOIS UNIV AT URBANA DEPT OF METALLURGY AND MINING--ETC F/G 11/6  
FRACTURE KINETICS OF HYDROGEN EMBRITTLED NIOBIUM.(U)  
MAR 81 B S HINDIN, H K BIRNBAUM N00014-75-C-1012  
NL

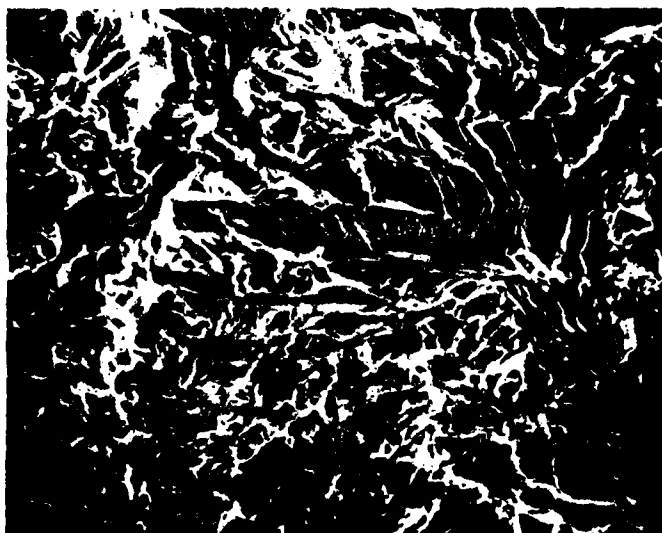
UNCLASSIFIED

2 OF 2

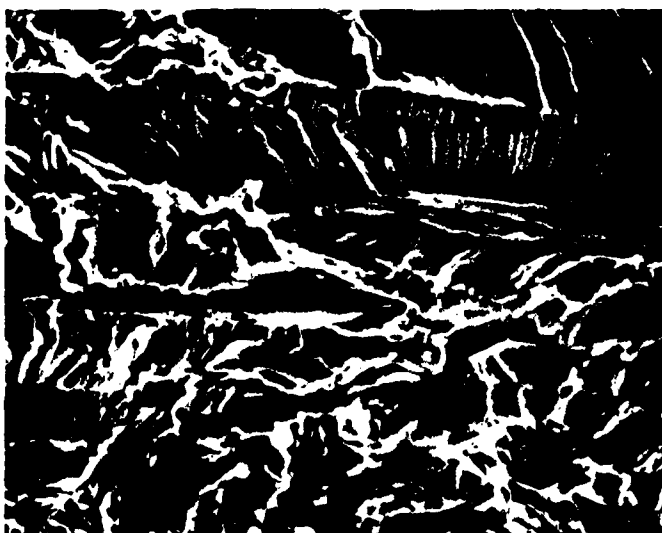
4U A  
039104



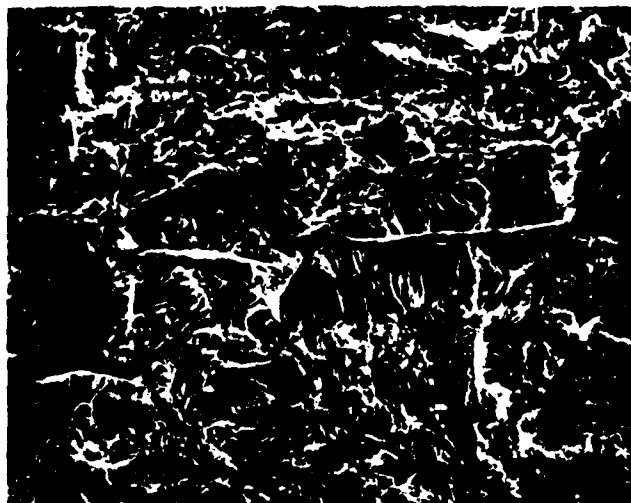
END  
DATE  
FILMED  
6-81  
DTIC



50  $\mu\text{m}$



25  $\mu\text{m}$



100  $\mu\text{m}$

Fig. 53. Fracture surface of d.t. specimen tested at constant  $K_I$  42 K below its solvus temperature.



25  $\mu\text{m}$

Fig. 54. Higher magnification of the center area in Fig. 53 showing brittle secondary crack and cleavage steps.

The assumptions in estimating the critical hydride size are listed below.

1. The stress induced hydride has a composition of  $\text{NbH}_{.75}$  ( $C_{\text{H}}^{\text{hyd}} = 43$  at .%).
2. The hydride has the shape of an ellipse of revolution whose major axis,  $a$ , is twice the length of the minor axis,  $b$ .
3. The surrounding volume from which hydrogen diffuses is bounded by a sphere of radius  $r$  where  $r$  is much greater than the length  $a$ .
4. Stress gradient effects are not taken into account.

For a hydride to form in an alloy with  $C_{\text{H}}^{\text{o}}$  less than 43 at .%, hydrogen must diffuse into the volume of the hydride from the surrounding spherical volume. Therefore,

$$0.43\pi ab^2 = (4/3)\pi r^3 C_{\text{H}}^{\text{o}} \quad (29)$$

The incubation interval  $t_{\text{inc}}$ , for the critical hydride size is given by

$$r = (D_{\text{H}}^{\text{Nb}} t_{\text{inc}})^{1/2} \quad (30)$$

where

$$D_{\text{H}}^{\text{Nb}} = 2.4 \times 10^{-4} \exp(-8.20 \text{ kJ/mol/RT}) \text{ cm/s} \quad (41) \quad (31)$$

Substituting Eqn. (30) into Eqn. (29) and letting  $l_{\text{c}} = a = 2b$ , yields

$$l_{\text{c}} = 76.7 (C_{\text{H}}^{\text{o}})^{1/3} \exp(-4.1 \text{ kJ/mol/RT}) \cdot (t_{\text{inc}})^{1/2} \quad (32)$$

where  $C_{\text{H}}^{\text{o}}$  = hydrogen concentration in solution at test temperature in at.%.  
 $l_{\text{c}}$  = critical hydride length in  $\mu\text{m}$ .

Table 8 lists the estimated hydride size using Eqn. (32) for various test temperatures and hydrogen concentrations. Metallographic observations of stress induced hydrides in this study and Grossbeck's<sup>(2)</sup> for niobium-hydrogen alloys showed sizes ranging from 10 to 50  $\mu\text{m}$ , in agreement with the estimated sizes for the higher temperatures.

TABLE 8  
Critical Hydride Size

$l_c$ ( $\mu\text{m}$ )	Hydrogen Concentration In Solid Solution At Test Temperature (at.%)	Test Temperature ( K )	$t_{inc}$ (s)
0.02	$6.4 \times 10^{-6}$	77	78
0.6	0.0017	112	30
30	0.46	218	24
29	0.46	221	21
35	1.3	243	10
41	2.3	273	6

## 6. DISCUSSION

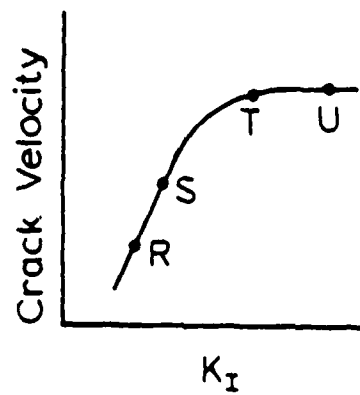
### 6.1 Single Edge Notch Data (Increasing $K_{Ic}$ Tests)

Velocity versus stress intensity results for the s.e.n. tests (Figs. 10-13) can be explained assuming stress induced hydrides precipitate in the region of stress concentration produced at the specimen's notch.<sup>(2)</sup> As the stress is applied, hydrogen diffuses to the stress concentration at the notch due to the chemical potential gradient and stress induced hydrides form and cleave. Figure 55a is a schematic representation of a (V-K) curve for the increasing  $K_{Ic}$  tests and has been labeled with points R, S, T and U. Figures 55b-55e are schematic representations of the conditions occurring at the crack tip corresponding to point R, S, T and U, respectively. The dashed ellipses are the plastic zone boundaries and the smaller ellipses within the boundaries are the precipitated hydrides. These figures will be referenced in the following discussion.

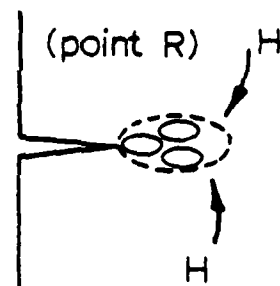
At low stresses hydrogen flux to the crack tip takes place in response to the chemical potential gradient caused by the external stress. At temperatures below the solvus temperature the stress will also induce hydride precipitation at the crack tip<sup>(9,11,42)</sup> while at temperatures above the solvus temperature this will occur only at stresses large enough to increase the local solvus temperature to a value above the test temperature.<sup>(9,11,42)</sup> At a particular stress, corresponding to a threshold stress intensity,  $K_{I0}$ , the hydrides will fracture and the crack will propagate to the interface with the solid

Fig. 55. Schematic representation of the (V-K) curve for increasing  $K_I$  tests (a), and conditions of the plastic zone and hydrides at the crack tip as crack growth occurs (b), (c), (d) and (e).

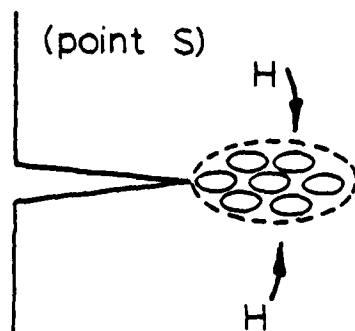




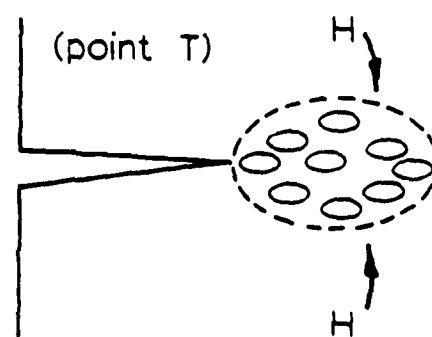
(a)



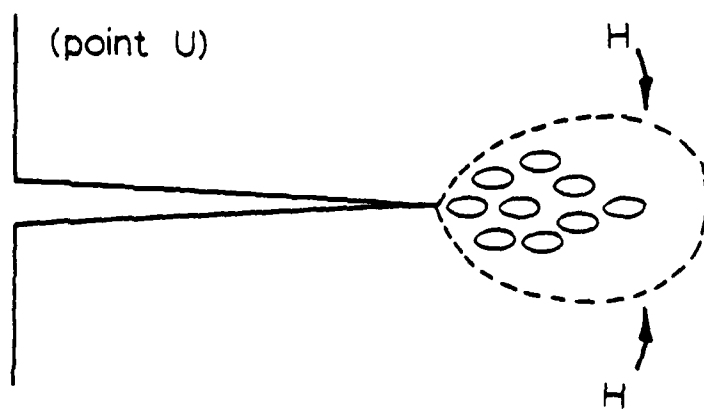
(b)



(c)



(d)



(e)

solution (Fig. 55b). The crack front of the fractured hydride will then serve as a stress concentrator and the process will repeat itself. (9,11,42)

As shown previously by Eqn. (22),  $K_I$  for the s.e.n. specimens, increases as the crack extends. The increasing  $K_I$  would result in a larger plastic zone, a higher local concentration of hydrogen and a decrease in the local solvus thus resulting in faster formation of hydrides (Fig. 55c), and consequently an increase in crack velocity. In the low  $K_I$ , increasing velocity region the stress induced hydride extends throughout the plastic zone and the crack velocity will increase as  $K_I$  and the plastic zone size increases. At sufficiently high  $K_I$  (Fig. 55d), the growth of the hydride and hence the crack velocity will become rate limited by diffusion of hydrogen from the surrounding area to the plastic zone. With a further increase in  $K_I$ , the plastic zone size,  $r_y$ , will continue to grow (Fig. 55e), since  $r_y$  is proportional to  $K_I^2$ , but the crack velocity will not increase since it is now rate limited by diffusion of hydrogen. In this region the extent of the hydride field is less than  $r_y$ . This will result in Stage II behavior of the (V-K) curve. This is, indeed, what the s.e.n. (V-K) results showed (Figs. 10-13).

The fractographic observations of this study and those previously reported<sup>(2)</sup> support this model. In particular, a stress induced hydride embrittlement mechanism can account for the observations that all fracture surfaces of the s.e.n. specimens exhibited brittle transgranular cleavage at low strain rates and ductile necking at high

strain rates. The ductile fracture results when failure occurs at high  $K_I$  in the plastic zone in front of the precipitated hydride zone.

## 6.2 Double Torsion Specimen

### 6.2.1 Decreasing $K_I$ Data

The (V-K) behavior for the decreasing  $K_I$  tests can be satisfactorily explained by the effects of the stress on the solvus and its effect on the crack velocity. These tests were carried out above  $K_{I0}$ , the stress intensity for fracture of the hydrides, and therefore the crack velocity reflects the rate of hydride formation. Figure 56 shows the low concentration end of the niobium-hydrogen equilibrium phase diagram<sup>(7)</sup> and the relative positions of the high, low and intermediate temperature tests with respect to their solvus. The (V-K) behavior of these three temperature ranges will be discussed below.

Figure 57a is a schematic representation of the (V-K) curves at high temperatures. Curves for two temperatures,  $T_1$  and  $T_2$ , are shown where  $T_1$  is greater than  $T_2$ . The curve for  $T_1$  is labeled with points X and Y. Curve  $T_2$  is labeled with point Z where points X and Z represent the same  $K_I$  value. Figures 57b-57d are schematic representations of the conditions at the crack tip for points X, Y and Z, respectively. Reference will be made to these figures for the following high temperature discussion.

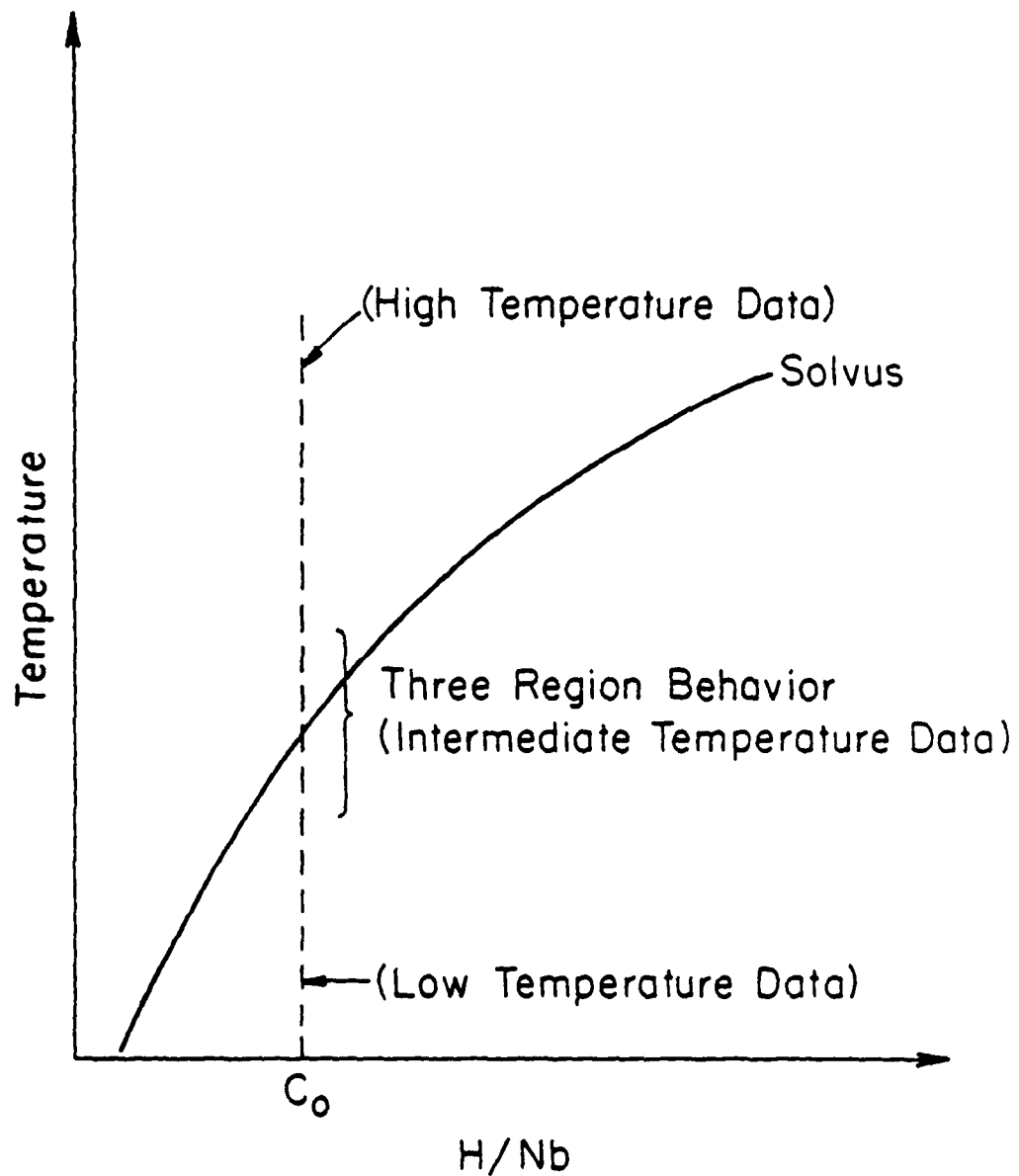


Fig. 36. Low concentration end of niobium-hydrogen equilibrium phase diagram showing positions of decreasing  $K_I$  tests relative to the solvus.

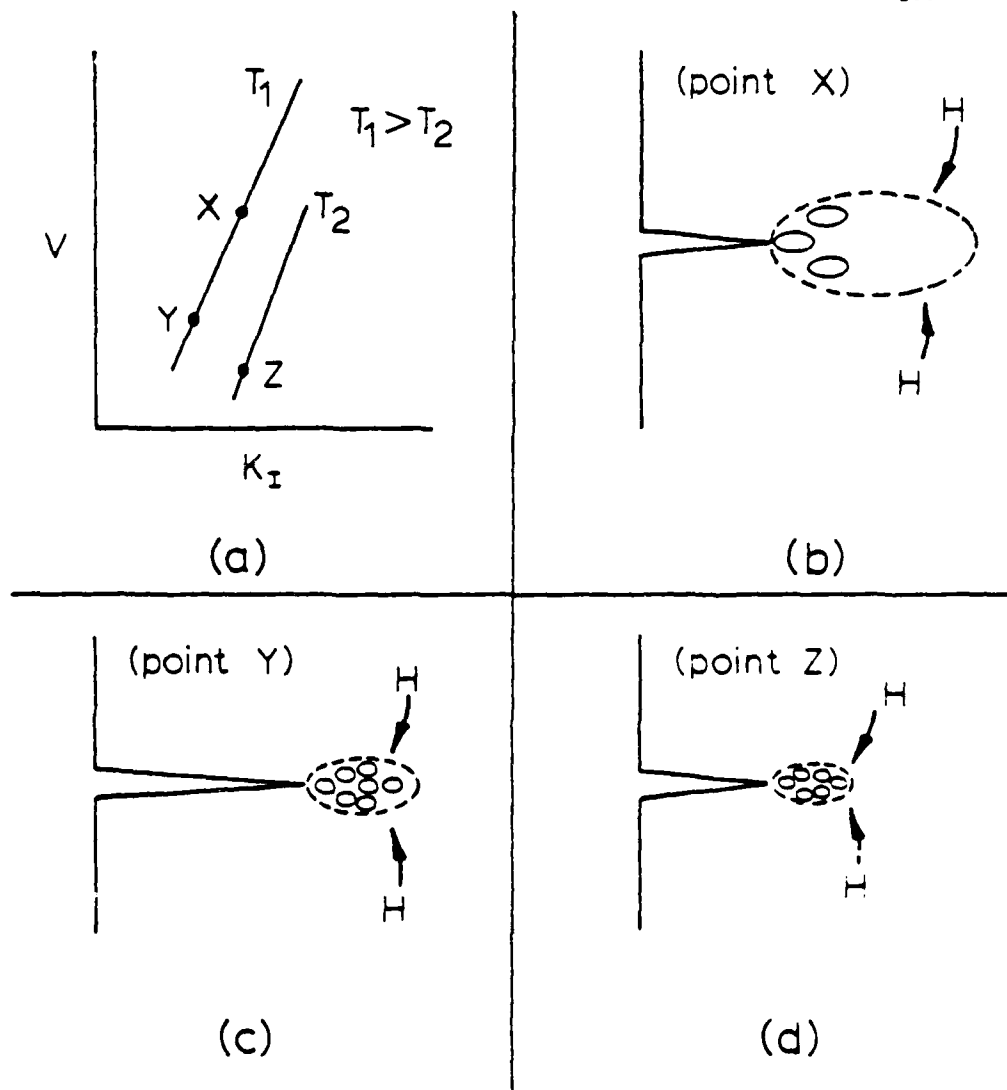


Fig. 57. Schematic representations of (V-K) curves for high temperature decreasing  $K_I$  tests (a), and the corresponding hydride and plastic zone conditions at the crack tip (b), (c) and (d).

If a specimen is tested above its solvus temperature ( $T > T_s + 35 \text{ K}$ ) then only a very high stress should be able to stress induce hydrides at the crack tip. It can be shown that the local solvus temperature at the crack tip is increased about 25 K for a local triaxial stress of 5% of the shear modulus with 1.0 at.% hydrogen in solution.<sup>(2)</sup> In addition to the effect of elastic stress fields at the crack tip on raising the hydride solvus temperature, the plastic deformation will assist the formation of hydrides by reducing the free energy associated with the elastic and plastic accommodation terms<sup>(9,10)</sup> Thus, on loading the specimen, crack propagation will not occur until the stress intensity and the crack tip plasticity raises the local solvus temperature to allow hydride precipitation, (Fig. 57b). Once the hydrides are precipitated, they will fracture and the crack will again propagate at a rate which will be determined by the rate of hydride formation at the crack tip. Since  $K_I$  decreases as the crack propagates, the driving force for hydride precipitation and correspondingly the rate of hydride formation will decrease. Figure 57c is a schematic representation of the smaller plastic zone and hydrides due to a drop in  $K_I$  resulting in a decrease in crack velocity. The high temperature (V-K) curves, (Fig. 22), exhibited this behavior.

For high temperature tests, the local solvus temperature at the crack tip must be increased to the testing temperature, by the local stress field and plastic deformation, to allow the hydrides to precipitate and cleave. This determines the  $K_I$  at which the crack begins to propagate during loading of the specimen. The relatively low value of  $K_I$  at which the crack begins to propagate compared to the

results at low and intermediate temperatures, (Figs. 25 and 35), may be explained by the fact, that at high temperatures, the Nb yield stress is quite low ( $\sim 350$  MPa). This results in a relatively low applied stress required to perform the plastic work which assists the plastic accommodation of the hydrides, allowing them to be stress induced. It does suggest that the dominant terms in shifting the solvus temperature at the crack tip are the reduction of the elastic and plastic accommodation free energies.<sup>(9)</sup> This is a conclusion which is consistent with previous suggestions.

As can be seen in Fig. 22 the (V-K) relation in this temperature range is not single valued as the curves depend on the temperature of the test. At a constant  $K_I$  value the velocity obtained at higher temperature is greater than that obtained or extrapolated from a lower temperature. This is not unexpected since the temperature dependence of the crack propagation at high temperatures will reflect the diffusion of hydrogen to the crack tip as well as any variation of crack tip plasticity with temperature since the dominant effect of stress appears to be the plastic accommodation terms. The conditions at the crack tip responsible for the smaller velocity at equal  $K_I$  at temperature  $T_2$  are shown in Fig. 57d. The increase in yield strength at the lower temperature is responsible for a smaller plastic zone and hydride field resulting in lower crack velocities as compared to the curve for  $T_1$  at equal  $K_I$ .

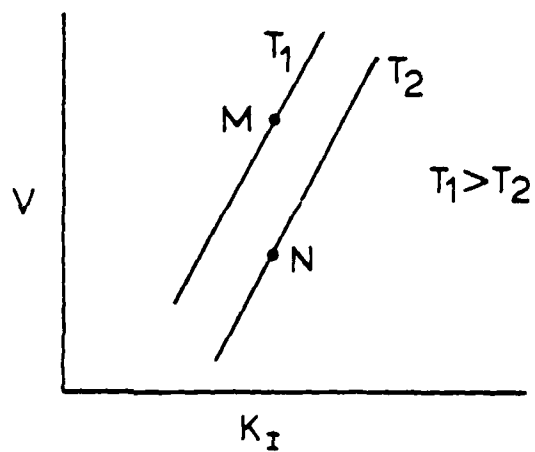
The high temperature fractography (Figs. 23 and 24) shows the presence of some ductile tearing which is consistent with the expected

increase in plasticity for these temperatures. These regions of ductile fracture probably occurred between the stress induced hydrides.

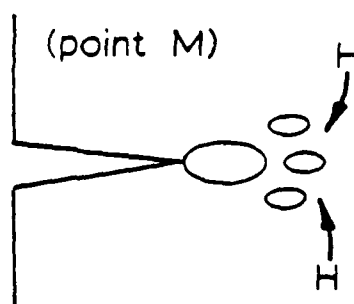
Figure 58a is a schematic representation of the decreasing  $K_I$  (V-K) curves at low temperatures. Curves for two temperatures,  $T_1$  and  $T_2$  are shown where  $T_1$  is greater than  $T_2$ . The curves for  $T_1$  and  $T_2$  are labeled with points M and N which represent the same  $K_I$  value. Figures 58b and 58c are schematic representations of the conditions at the crack tip for points M and N, respectively. Reference will be made to these figures for the following low temperature discussion.

For specimens tested well below their solvus temperatures ( $T < T_s - 60$  K), most of the hydrogen in solution will have already been precipitated as bulk hydrides prior to loading and application of a stress will result in only a very small amount of stress induced hydrides at the crack tip (Fig. 58c). These stress induced hydrides as well as any favorably located hydrides which precipitate on cooling will cleave causing crack propagation until the crack arrests at the hydride-solid solution interface. Continued hydride formation and the concurrent crack propagation will proceed slowly since the hydrogen concentration in solid solution in the area surrounding the crack is small and the diffusivity is low at low temperatures. Crack propagation would be controlled by the rate of stress induced hydride formation as the tests were carried out above  $K_{I0}$ . Since these tests are carried out below the solvus the rate of hydride formation is limited by the hydrogen diffusion to the crack tip.

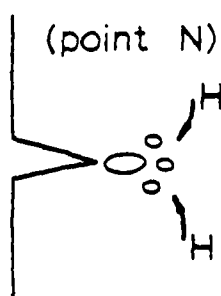




(a)



(b)



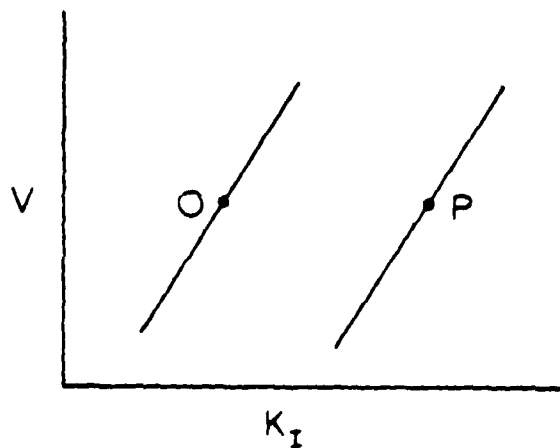
(c)

Fig. 58. Schematic representations of (V-K) curves for low temperature decreasing  $K_I$  tests (a), and the corresponding hydride conditions at the crack tip (b) and (c).

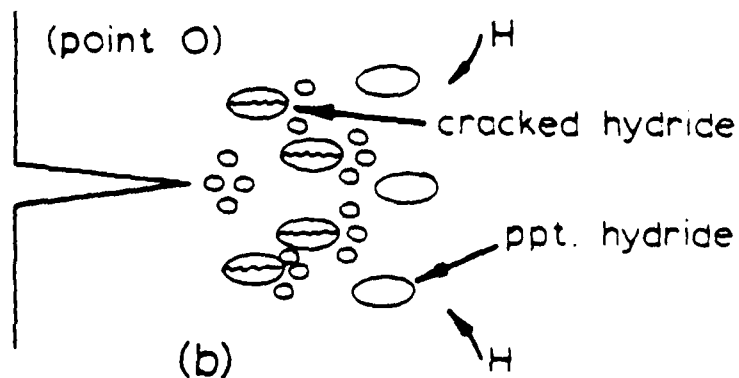
In the low temperature range the Nb yield stress is high ( $\sim 1400$  MPa) and the crack tip plastic zone correspondingly small (Fig. 58c). In the absence of a large plastic zone, the local  $K_I$  will be large (a relatively sharp crack), and the dominant effect of stress on the hydride formation will be on the elastic free energy terms.<sup>(9)</sup> The local stress field at the crack tip provides the driving force for hydrogen diffusion and hydride formation. The rate of hydride formation and hence of crack propagation would reflect primarily the hydrogen flux to the crack tip region and the temperature dependence of the (V-K) curve would then reflect the temperature dependence of the hydrogen diffusivity. For the same  $K_I$  values (Fig. 58a), the hydride at the crack tip as well as the crack velocity at  $T_1$  will be greater than the crack velocity at  $T_2$  due to the lower hydrogen diffusivity.

Since  $K_I$  decreases as the crack propagates, the driving force for hydride formation at the crack tip, i.e., the stress induced decrease in the free energy of the hydride, correspondingly decreases and the rate of hydride formation decreases. This behavior would correspond to a steep decrease in the crack velocity at a relatively high  $K_I$  and this is, in fact, what is observed at 77 K as shown previously in Fig. 25.

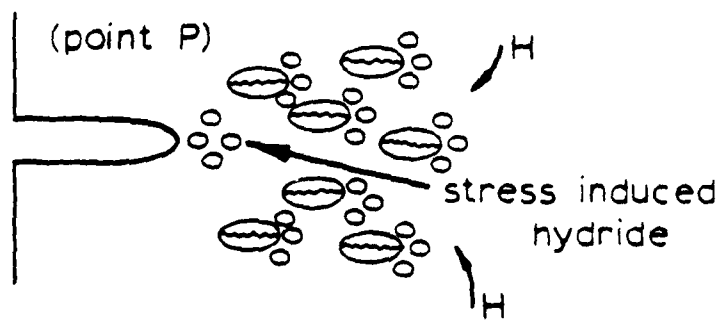
In this low temperature range it is striking that decreasing  $K_I$  tests begun at different  $K_I$  values at the same temperature do not fall on a single (V-K) curve. Tests begun at low  $K_I$  values show much higher crack velocities than those extrapolated from data obtained in tests initiated at higher  $K_I$  values (Fig. 25). Figure 59a is a schematic representation of the multivalued nature of the decreasing  $K_I$  (V-K) curves at 77 K. The curve labeled with point O is the low initial  $K_I$  curve



(a)



(b)



(c)

Fig. 59. Schematic representation of multivalued ( $V$ - $K$ ) curves for the decreasing  $K_I$  tests at 77 K (a), and the corresponding hydride conditions at the crack tip for different  $K_I$  values (b) and (c).

while the curve labeled with point P is the high initial  $K_I$  curve. The fact that the curves are not colinear illustrates the double valued nature of the (V-K) behavior at 77 K. Figures 59b and 59c are schematic representations of the conditions at the crack tip for points O and P, respectively. Reference will be made to these figures in the following discussion.

The multivalued nature of the (V-K) data at 77 K can be understood in view of the fact that a significant amount of the hydrogen was precipitated as hydrides on cooling prior to loading. On application of a stress, at a stress intensity above  $K_{I0}$ , these hydrides will fracture and the measured crack velocity will be the result of crack propagation through the precipitated hydrides and the formation of stress induced hydrides in front of the cracked hydrides as well as in front of the macroscopic notch. The local stress intensity at the macroscopic crack tip,  $K_I^{eff}$ , will be reduced by this hydride cracking in the same manner as by a plastic zone at the crack tip. For tests which begin at low  $K_I$  (Fig. 59b), the extent of this fracture zone is limited and crack propagation occurs by stress induced hydride formation and cleavage at rates determined by hydrogen diffusion to the crack tip at  $K_I^{eff} = K_I$ . The same mechanism applies for tests begun at high  $K_I$  values (Fig. 59c) but a more extensive region of hydride cracking occurs in the precipitated hydrides thus giving an effectively large crack opening displacement with a corresponding decrease in the local  $K_I^{eff}$ . The crack propagates at hydride formation rates consistent with the  $K_I^{eff}$  less than  $K_I$  (applied). At the highest  $K_I$  value tested, many hydrides will fracture and more will be stress induced from the little remaining

hydrogen in solution. This will result in the highest crack velocity as was observed. Due to the decrease of the local  $K_I$  resulting from the large crack field, the velocity will be lower than that extrapolated from tests at low initial  $K_I$  values. The identical slopes of the 77 K (V-K) data which were obtained at different initial  $K_I$  values (Fig. 25) indicates that the rate controlling mechanism, hydrogen diffusion to the crack tip, is independent of the initial  $K_I$  values and depends on the  $K_I^{\text{eff}}$ . Equal crack velocities imply equal hydrogen fluxes and hence equal  $K_I^{\text{eff}}$  even though the macroscopic  $K_I$  values may differ greatly.

The differences between the crack velocities for hydrogen and deuterium charged specimens (Fig. 26) can be understood by considering the isotope effect on the hydrogen diffusion. At 77 K, the ratio between the hydrogen and deuterium diffusion coefficients using data from Wipf and Alefield<sup>(43)</sup> is given by

$$(D_H^{\text{Nb}}/D_D^{\text{Nb}})_{T=77} = 12.8 . \quad (33)$$

Extrapolation of data by Matusiewicz and Birnbaum<sup>(44)</sup> yields a ratio of 17. Since the crack velocities in this low temperature range are determined by hydrogen flux to the crack tip, the isotope effect on velocity should be equal to its effect on the diffusivity. These ratios agree very well with the value of 15 measured for the ratio of the velocities between hydrogen and deuterium charged specimens tested at 77 K. It is clear that the isotope effect accounts for the observed differences in the crack velocities between hydrogen and deuterium

charged d.t. specimens and that the crack velocity in this temperature range is controlled by hydrogen flux to the crack.

Due to the presence of hydrides prior to loading, a predominance of brittle cleavage should occur on the fracture surface and this was observed to be the case. For regions where the crack outran the supply of hydrogen, microvoid coalescence should occur and this also was observed as pointed out in Section 5.2.2.4.

The (V-K) behavior in the intermediate temperature range, i.e. temperatures in the vicinity of the solvus, is considerably more complex than at high or low temperatures as was shown in Fig. 35. This complexity seems to result from the interplay between the large effects of stress on the hydride precipitation and the flux of hydrogen into the crack tip region which allows this precipitation to occur. In this temperature range the variation of the velocity with  $K_I$  was divided into three regions as presented previously in the Results section (5.2.2.5) and shown in Fig. 32. Figure 60 is a schematic representation of the hydrides in the vicinity of the crack tip as the crack advances through Regions A, B and C.

Region A, which occurs immediately on loading the specimen to initiate the crack, consists of a very rapid increase of the crack velocity as  $K_I$  decreases with the crack velocity reaching a maximum value and then decreasing. As seen in Figs. 33 and 34 the initial increase is not always observed and seems to result when the crack is initiated at high stress intensity. At lower  $K_I$  values for the initiation of the fracture only, the decreasing part of the (V-K) curve in Region A is seen. In this temperature range, where the hydrogen

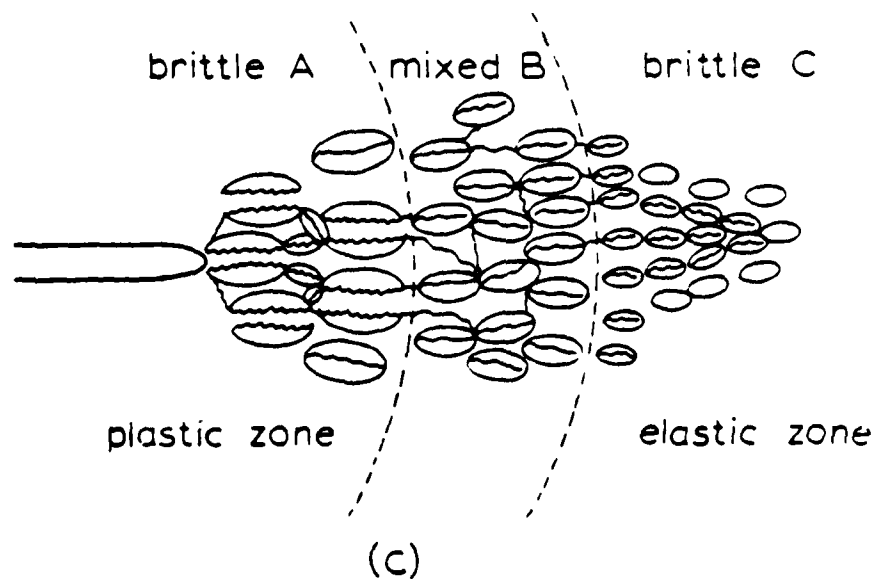
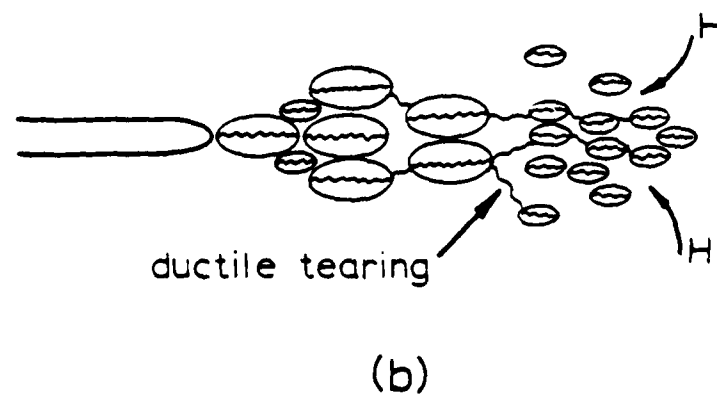
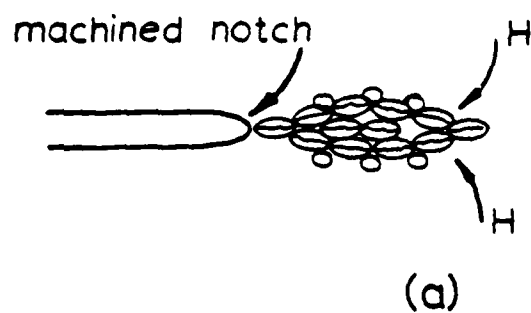


Fig. 60. Schematic representation of hydride behavior responsible for three region (V-K) curves at intermediate temperatures for decreasing  $K_I$  tests as crack advance occurs (a), (b) and (c).

diffusivity is high, large hydride precipitates form during loading of the specimen providing a continuous crack path (Fig. 60a). When these hydrides crack, the propagation rate will increase rapidly into the pre-existing precipitated hydride field. The growth of these hydrides during loading and initial crack propagation, results in a depletion of the hydrogen concentration in the volume in front of the notch. Thus the crack velocity quickly decreases as the crack grows out of the region of hydrides precipitated during loading. For cracks begun at lower  $K_I$ , a smaller hydride zone is formed and the initial high velocity corresponds to the crack propagation through the hydride field. Only the decrease in velocity due to the depletion of the hydrogen concentration by the initial precipitation is seen because at the lower  $K_I$  values, the hydride growth is relatively slower.

As the crack slows down in Region A, existing hydrides continue to grow and new ones are precipitated ahead of the crack tip as depicted in Fig. 60b. This occurs due to stress assisted diffusion of hydrogen to the plastic zone area. The further growth of the hydrides allows the crack to accelerate and the crack propagates by linking up of the cracked hydrides as in Region B.

In Region B, the velocity is determined by the rate of hydride growth and is controlled by diffusion of hydrogen in the stress field at the crack tip. The velocity increase results because the hydrides precipitate well in front of the crack tip and the crack can advance into an existing hydride field (Fig. 60b). Due to the high crack velocity, the linkage of the cracked hydrides by additional hydrides formed during the cracking process, may not be complete and



some ductile tearing may result between the cleaved hydrides as is observed (Figs. 42 and 43).

As a result of the growth of the hydrides in Regions A and B, the volume in front of the crack becomes depleted of hydrogen requiring diffusion from greater distances to form hydrides. This results in a decrease of the hydrogen flux. In addition, the driving force for the stress assisted diffusion falls as  $K_I$  falls. Both effects decrease the amount of hydrogen reaching the plastic zone and hence decrease the rate of hydride formation resulting in a decrease of crack velocity as observed in Region C (Fig. 60c). The crack propagates at a decreasing velocity until the stress intensity falls below  $K_{I0}$ , the stress intensity to crack the hydride, or until  $K_I$  falls below the stress required to form new hydrides at the temperature of the test. The latter factor would provide the threshold condition at temperatures above the solvus while the former would apply below the solvus since even relatively small stress intensities would bias the free energies in favor of hydride formation at the crack tip. This expectation is in accord with the data presented in Figs. 31-34. The data for d.t. specimens 23 and 25 (Fig. 33) correspond to the tests 95 K below the solvus and the  $K_{I0}$  in Region C is about  $3 \text{ MPa} \cdot \text{m}^{1/2}$ . In contrast, the tests for d.t. specimens 53 (Fig. 31), 41 and 54 (Fig. 34), which correspond to test temperatures 13, 18 and 16 K above their respective solvus temperatures, have threshold stress intensities of about 7, 8 and 11  $\text{MPa} \cdot \text{m}^{1/2}$ , respectively. These would correspond to the  $K_I$  required to shift the local solvus temperatures to the test temperatures and are larger than  $K_{I0}$  as expected.

Further discussion of  $K_{I0}$  for various tests will be found in section 6.4

The data exhibiting three region behavior discussed above was obtained in decreasing  $K_I$  tests at intermediate temperatures. A similar behavior was noted in the decreasing  $K_I$  test at 112 K (Fig. 25) although the data were not as complete. This test was performed 96 K below the solvus. While the general behavior was similar to that observed for specimens tested in the decreasing  $K_I$  test at 148 K, 95 K below the solvus (Fig. 33), the three regions were less well defined. Double torsion specimens tested at 148 K had almost 20 times more hydrogen in solution than in the specimen tested at 112 K (see Table 6). It appears, however, that the small amount of hydrogen remaining in solid solution for the specimen tested at 112 K is sufficient to cause the three region (V-K) curve though to a much less well defined extent.

The distinguishing feature of the intermediate temperature range fractography is the completely brittle fracture in Regions A and C and the large amount of ductility associated with Region B of the (V-K) curves (Figs. 39-43). This is consistent with the suggestion that the increase in crack velocity for decreasing  $K_I$  in Region B is due to the hydride formation in front of the crack and linking up of fracturing hydrides. A large amount of ductility between these hydrides would be expected if the velocity was too large for the hydrogen flux which results and therefore a complete hydride path is not formed. The more brittle fractographic features for Regions A and C as shown previously (Figs. 36-38 and 44) are consistent with

their corresponding (V-K) behavior. In Region A, the precipitation of the hydrides during loading results in large hydrides which form an almost continuous path for the fracture. In Region C, the rate of fracture is low enough and is controlled by hydride formation at the crack tip at a rate sufficient to form a complete hydride path for the fracture.

#### 6.2.2 Constant $K_I$ Data

The occurrence of the three stage behavior for the constant  $K_I$  tests as shown in Fig. 45 can be readily explained by a stress induced hydride embrittlement mechanism. In the low  $K_I$  Stage I an extremely high dependence of crack velocity on  $K_I$  was observed. The nature of this dependence is such that Stage I may be a transition between the crack arrest  $K_I$  (i.e.  $K_{I0}$ , the stress intensity for crack propagation in the brittle hydride) and the constant  $K_I$ , Stage II behavior. This is in agreement with the work done on hydrogen embrittled Zirconium alloys.<sup>(27)</sup> Discussion of  $K_{I0}$  for constant  $K_I$  will be found in section 6.4

Stage III was characterized by the onset of rapid crack growth and was observed to be independent of temperature and hydrogen concentration. It corresponds to the effective critical stress intensity,  $K_{IC}^{eff}$ , for rapid fracture by overload. The effective critical stress intensity will be less than the true  $K_{IC}$  since the presence of brittle hydrides in a ductile matrix will reduce the fracture roughness. Fractography was consistent with this behavior since the amount of ductility increased as Stage III was approached (Fig. 50).

Stage II for the constant  $K_I$  data can be explained by a rate limiting model having the crack velocity controlled by the rate of diffusion of hydrogen to the crack tip. In this region a continuous hydride fracture path forms at a rate which is controlled by hydrogen flux to the crack tip. A modified theoretical model by Simpson and Puls<sup>(27)</sup> based on diffusion limited crack propagation is presented in section 6.3. This model allows the expected activation energy for the rate limiting process of Stage II to be calculated. The theoretical value will be shown to be in good agreement with the experimentally observed activation enthalpy for crack propagation in Stage II of the constant  $K_I$  data.

### 6.3 Theoretical Stage II Activation Energy

A theoretical model was presented by Simpson and Puls<sup>(27)</sup> to describe the crack propagation behavior in hydrogen embrittled Zr-2.5 wt.% Nb alloys. A cylindrical geometry shown in Fig. 61 is assumed surrounding the crack tip.<sup>(26)</sup> Their expression for the crack velocity when applied to Nb-H alloys is given by

$$v = \frac{4\Omega_{\text{hyd}} \pi D_{\text{H}}^{\text{Nb}} \cdot C_{\text{H}}^{\text{O}}}{3(\lambda^2) \Omega_{\text{Nb}} \phi(\lambda, L)} \left\{ \exp \left[ \frac{w_{\text{t}}^{\text{inc}}(L)}{RT} \right] \exp \left[ \frac{w_{\text{t}}^{\text{a}}(L)}{RT} \right] \right. \\ \left. - \exp \left[ \frac{w_{\text{t}}^{\text{inc}}(\lambda)}{RT} \right] \exp \left[ \frac{w_{\text{t}}^{\text{a}}(\lambda)}{RT} \right] \right\} \quad (34)$$

- where  $W_t^{inc}$  = Total molal elastic strain energy of matrix and hydride.
- $W_t^a$  = Molal interaction energy of an inclusion with an applied elastic stress field.
- $\Omega_{hyd}, \Omega_{NB}$  = Atomic volumes of hydride and alpha phase atoms in Nb, respectively.
- $D_H^{Nb}$  = Diffusion coefficient of hydrogen in alpha Nb.
- $C_H^0$  = Terminal solid solubility of hydrogen at zero applied stress when precipitated hydrides are present (or the average hydrogen concentration in solid solution at temperatures above the solvus).
- $L$  = Distance from the crack tip to source hydrides in Zr-H alloys as shown in Fig. 61. This parameter was redefined below because source hydrides do not exist in Nb-H alloys.
- $\ell$  = Distance from crack tip to center of plastic zone given by  $K_I^2 / 12\pi\sigma_y^2$ . The factor,  $\sigma_y$ , is the yield stress and at low temperatures is a strong function of temperature.
- $\ell'$  = Crack tip radius and is given by  $K_I^2 / 2\sigma_y E$ , where,  $E$ , is Young's Modulus.
- $\Phi(\ell, L)$  = Function of  $\ell$  and  $L$  approximated by  $\ln(L/\ell)$ .

Equation (34) was derived assuming that the rate of hydride growth in the vicinity of the crack tip is equal to the crack velocity. This ignores the observation that the hydrogen embrittled crack growth is



generally discontinuous in nature.<sup>(27)</sup> Since resolution of the hydrides in niobium are not observed as the crack propagates, the concept of hydrides acting as sources of hydrogen does not apply and the parameter  $L$  must be redefined. In the Nb-H system the solid solution acts as a source of hydrogen for the precipitation of the hydrides at the crack tip. In this case the parameter  $L$  is the distance at which the hydrogen concentration equals the solid solution concentration in equilibrium with the hydrides in an unstressed system (or the solid solution concentration in the absence of the hydrides). For computational purposes,  $L$  was taken to be  $5 \times 10^{-3}$  m which is approximately ten times the plastic zone radius. The crack velocity depends only on  $[\ln(L)]^{-1}$  since  $w_t^{\text{inc}}$  does not depend sensitively on the parameter  $L$  (Eqn. (34)).

The major temperature dependence in Eqn. (34), neglecting  $w_t^{\text{inc}}$  and  $w_t^a$  is found in the product  $D_H^{\text{Nb}} \cdot C_H^0$  for specimens tested below the solvus temperature in systems where the hydrides can redissolve and act as a source of hydrogen. For tests conducted above the solvus temperature or where resolution of the hydrides does not occur, temperature dependence resides only in  $D_H^{\text{Nb}}$ . The diffusion coefficient can be expressed as

$$D_H^{\text{Nb}} = D_0 \exp(-Q/RT) , \quad (35)$$

where  $D_0$  = the pre-exponential multiplier,  
 $Q$  = the activation energy.

Neglecting  $w_t^{inc}$  and  $w_t^a$ , Eqn. (34) can be rewritten as,

$$V = \alpha C_H^0 \exp(-Q/RT) \quad (36)$$

where

$$\alpha = (4\Omega_{hyd} \pi D_o) / 3(2')\Omega_{Nb} \Phi(2, L) . \quad (37)$$

The crack velocity given in Eqn. (36) should follow an Arrhenius behavior. The diffusion coefficient for hydrogen in niobium, measured by Schaumann et al.<sup>(45)</sup> has been found to deviate from an exponential behavior below room temperature. On the other hand, Marusiewicz et al.<sup>(41)</sup> did not find this deviation and for temperatures greater than 165 K, the diffusion coefficient had an activation energy of 8.20 kJ/mol.

The factor  $w_t^{inc}$  depends only on the degree of elastic misfit between the matrix and hydride but not on the applied stress. This implies<sup>(27)</sup>

$$w_t^{inc}(2) = w_t^{inc}(L) = w_t^{inc} , \quad (38)$$

which allows its contribution to the activation energy to be approximated. Puls<sup>(5)</sup> calculated  $w_t^{inc}$  for delta and gamma Zr hydrides having various orientations. Values he found for hydrides having shapes of plates and needles with various orientations ranged from 7.74 kJ/mol to 2.66 kJ/mol. Morphologies observed for niobium hydrides were plate, blocky, dendritic and starlike.<sup>(2)</sup> Stress induced hydrides appearing on specimen surfaces resembling ellipsoids were observed in this investigation. Knowing the equilibrium shape of niobium hydride i.e. a plate, lying parallel to its {100} fracture plane,



$w_t^{inc}$  for niobium-hydrogen alloys was calculated by the following expression used by Puls. (5)

$$w_t^{inc} = v_\beta [E/(1-\nu)] \{ \Delta^2 + (\pi c/2a) [\Delta \cdot \xi + \xi^2/4(1+\nu)] \} \quad (39)$$

where  $c/a = 0.05$  (ratio between minor and major axes for plate).

$E = 1.05 \times 10^{11}$  Pa (Young's modulus for niobium). (46)

$\nu = 0.39$  (Poisson's ratio for niobium). (46)

$v_\beta = 12.3 \times 10^{-6}$  m<sup>3</sup>/mol (partial molal volume of beta hydride calculated from lattice constants for niobium hydride). (47)

$\Delta$  and  $\xi$  = Values defined by the transformation (stress free) strains of beta hydride which were calculated from lattice constants (47) and are equal to 0.039 and 0.003, respectively.

Substituting these values into Eqn. (39) yields

$$w_t^{inc} = 3.24 \text{ kJ/mol} \quad (40)$$

Since  $w_t^{inc}$  is positive, increasing values will exponentially increase the crack velocity.

The factor  $w_t^a$  in Eqn. (34) can be written, assuming elastic constants of hydride and matrix are equal, (5) as

$$w_t^a = -v_\beta \sigma_{ij} e_{ij} \quad (41)$$

where  $\sigma_{ij}$  = applied stresses (positive when tensile),

$e_{ij}$  = stress free transformation strains for the alpha to beta transition.

It can be shown that

$$W_t^a(l) \gg W_t^a(L) \quad (42)$$

since the hydrostatic stresses at the crack tip are much greater than the stresses outside the plastic zone. Typical stresses occurring at  $l$  (plastic zone) under plane strain conditions<sup>(5)</sup> are

$$\begin{aligned} \sigma_{11} &= 3\sigma_y(T) , \\ \sigma_{22} &= 1.8\sigma_y(T) , \\ \sigma_{33} &= 2.4\sigma_y(T) . \end{aligned} \quad (43)$$

Using the data from Chen and Arsenault<sup>(48)</sup> and Pereturina and Pavlov,<sup>(49)</sup> the temperature dependent yield stress of hydrogen charged polycrystalline niobium was approximated by

$$\sigma_y(T) = (1.09 \times 10^5 \text{ MPa} \cdot \text{K}^{-1})/T - (T/4) \text{ MPa} \cdot \text{K}^{-1} , \quad (44)$$

for temperatures between 75 and 300 K.

Figure 62 is  $W_t^a(l)$  versus temperature for a hydride plate parallel to {100} and the stresses  $\sigma_{11}$ ,  $\sigma_{22}$  and  $\sigma_{33}$  applied along [001], [100] and [010] directions, respectively. For temperatures between 180 and 303 K, which correspond to the constant  $K_I$  data,  $W_t^a(l)$  ranges between -2.0 and -1.0 kJ/mol.

Including  $W_t^a(l)$  and  $W_t^{\text{inc}}$ , Eqn. (36) becomes

$$V = \alpha C_H^0 \exp(-Q/RT) \cdot \exp W_t^{\text{inc}} \cdot \exp W_t^a(l) . \quad (45)$$

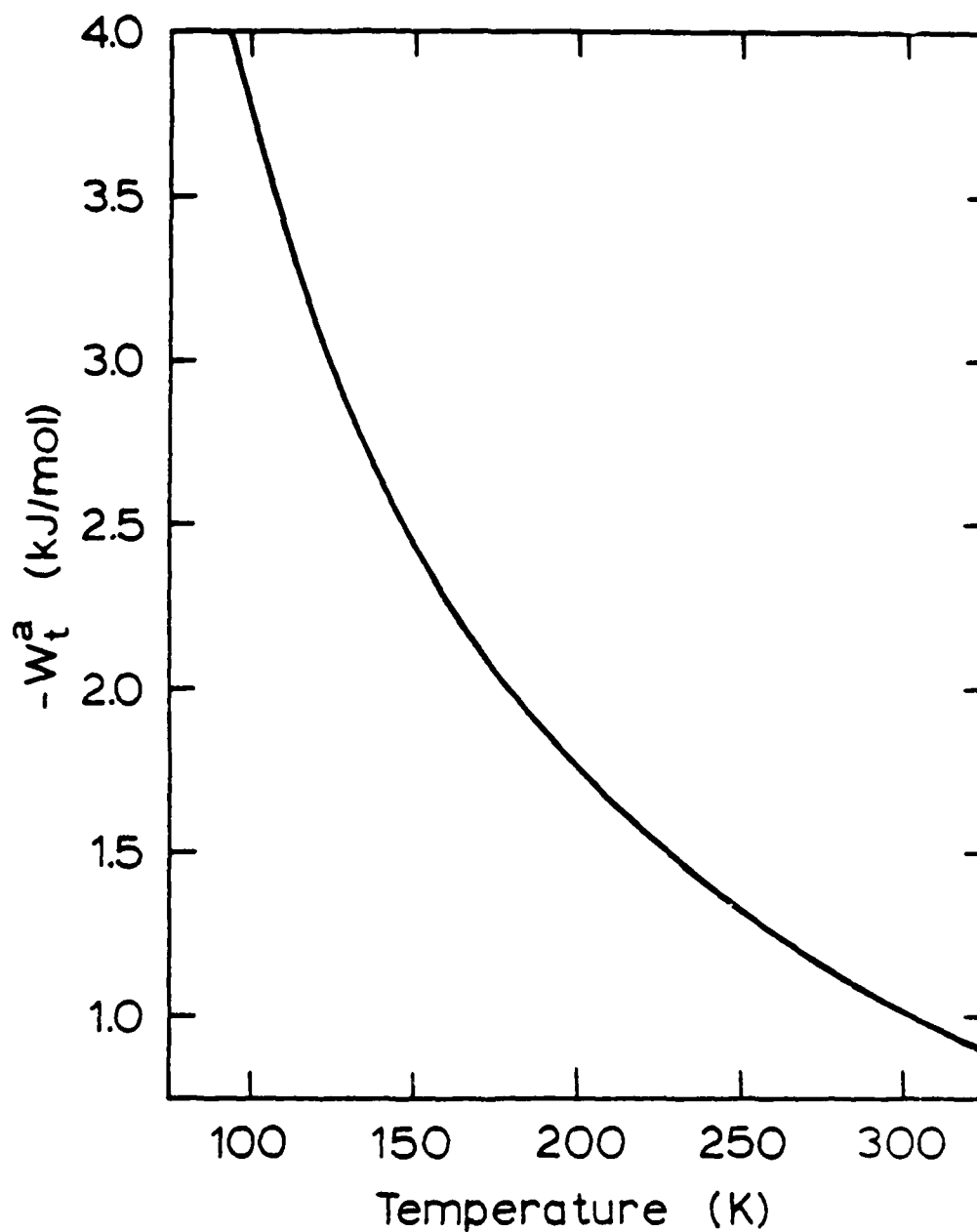


Fig. 62. Graph of  $-W_t^a$  versus temperature for niobium hydride plate parallel to the (100) planes and the stresses given by Eqn. (43) applied along the [001], [100] and [010] directions, respectively.

Substituting the values for  $Q$ ,  $W_t^{inc}$  and  $W_t^a(l)$  into Eqn. (45), the total activation energy,  $Q'$ , is found to range between

$$5.96 \text{ to } 6.96 \text{ kJ/mol} \quad (46)$$

for the constant  $K_I$  data. This range of activation energy is within the experimental error of the measured temperature dependence as will be shown below.

The Stage II activation enthalpy of the experimental constant  $K_I$  data can be compared to the theoretical values of Eqn. (45). Before this can be done, the effect of the hydrogen concentration in solution on the crack velocity must be taken into account. For the Nb-H system the appropriate value of  $C_H^O$  is the concentration in solid solution. This is achieved by rewriting Eqn. (45) so that

$$V/C_H^O = \alpha \exp(-\Delta H/RT) \quad (47)$$

where  $\Delta H$  is the activation enthalpy of the Stage II constant  $K_I$  data. Taking the natural logarithm of Eqn. (47) yields

$$\ln(V/C_H^O) = \ln \alpha - \Delta H/RT \quad (48)$$

The  $K_I$  range common to Stage II behavior for all temperatures tested lies between 27.5 and 32.5 MPa  $\cdot$  m<sup>1/2</sup> (Fig. 45). Figure 63 shows the Arrhenius plot of Eqn. (48) for  $K_I = 30.0$  MPa  $\cdot$  m<sup>1/2</sup>. Similar behavior was observed for  $K_I = 27.5$ , 32.5 and 35 MPa  $\cdot$  m<sup>1/2</sup>. Using the following relation,

$$\Delta H = R[\Delta \ln(V/C_H^O)/\Delta(1/T)] \quad (49)$$

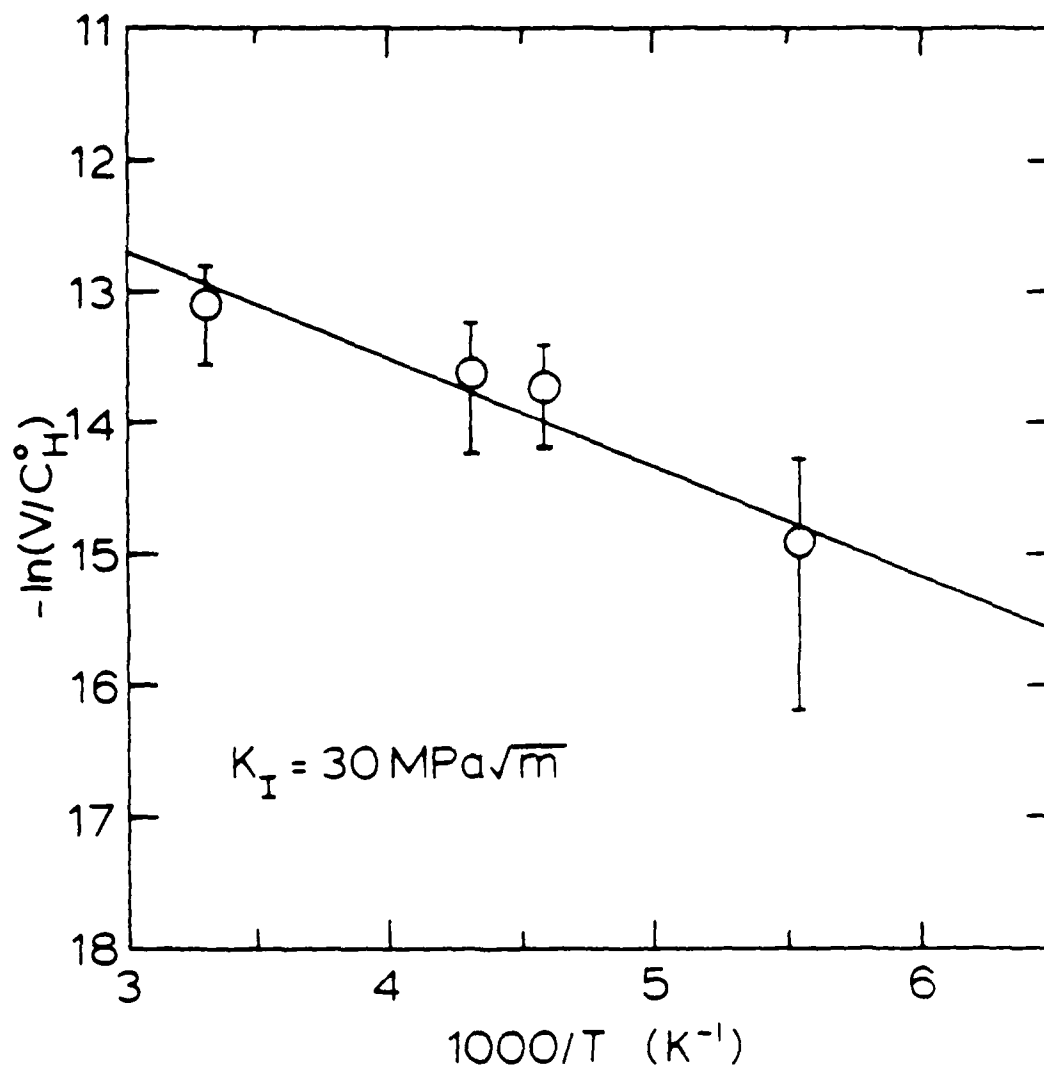


Fig. 63. Plot of  $-\ln(V/C_H^0)$  versus  $1/T$  for  $K_I = 30 \text{ MPa} \cdot \text{m}^{1/2}$ . Calculated activation enthalpy from best fit to data (solid line) using Eqn. (49) is 6.65 kJ/mol.

where  $R$  = the gas constant,

$T$  = temperature in K,

the activation enthalpies were calculated and then averaged resulting in

$$\Delta H = 6.6 \pm 1.5 \text{ kJ/mol} \quad (50)$$

which agrees very well with the measured values given in Eqn. (46).

Figure 64 shows Eqn. (34) plotted as crack velocity versus  $K_I$  for temperatures of 200, 150 and 300 K. Also plotted for purposes of comparison, are the constant  $K_I$  curves for temperatures of 232 and 300 K. The factor  $2'$  appearing in the denominator of Eqn. (34) was defined earlier as being proportional to  $K_I^2$ . As seen in Fig. 64, the (V-K) curves of Eqn. (34) reflect the crack velocities major dependence on  $(1/K_I^2)$ . The functional dependence of Eqn. (34) does not resemble the experimentally observed curves for either Zr-H<sup>(27)</sup> or Nb-H alloys (Fig. 64) for the constant  $K_I$  Stage II behavior and requires further refinement. Numerically, however, the calculated velocities are within a factor of three of the Stage II constant  $K_I$  crack velocities for equal  $K_I$  values.

#### 6.4 Threshold Stress Intensity Factors

As shown in the Results Section (Fig. 43), the threshold stress intensities of the constant  $K_I$  data for specimens tested above their  $T_{\text{trans}}$ ,  $K_{Ic}^{\text{H}} > T_{\text{th}}$ , were greater than the threshold stress intensity for the specimen tested below its  $T_{\text{trans}}$  temperature,  $K_{Ic}^{\text{H}} < T_{\text{th}}$ . This behavior can be explained by considering the effects of hydrogen

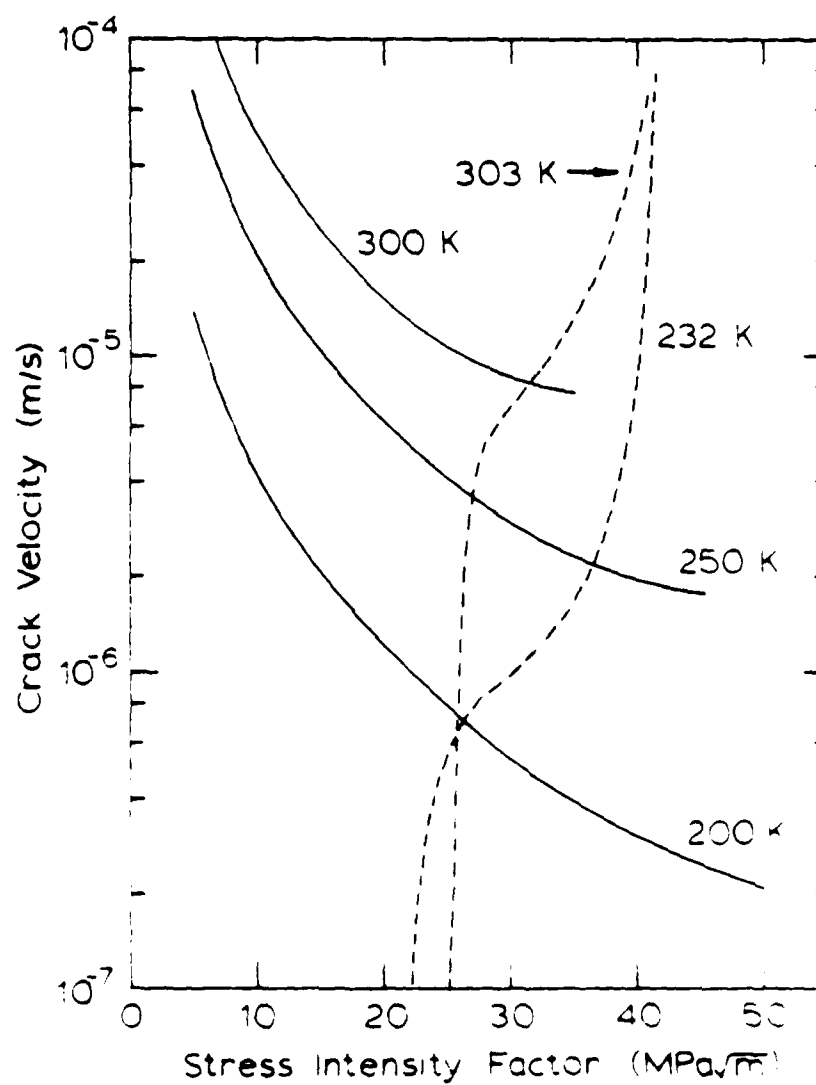


Fig. 24. Crack velocity versus  $K_I$  for Eqn. (34), solid lines, and constant  $K_I$  data, dashed lines, at various temperatures.

stresses on the solvus as was briefly reviewed in the Previous Research section. For specimens tested below its solvus, hydrides were present before loading occurred and the  $K_{I0}(T > T_S)$  is related to the minimum load required to fracture the existing hydrides and form stress concentrations at which additional hydrides are stress induced. Repetition of this process results in slow crack growth. Specimens tested above their solvus temperatures did not have hydrides present prior to loading and as discussed in section 6.2.1 for the decreasing  $K_I$  tests, crack propagation will not occur until the stress intensity and the crack tip plasticity raises the local solvus temperature to the test temperature and allows hydride precipitation. The difference between the stress intensity thresholds above and below the solvus temperatures represents the additional work required to stress induce hydrides. Similar behavior for the threshold stress intensities was observed for the decreasing  $K_I$  tests as shown in Figs. 31-35 which show  $K_{I0}(T > T_S)$  greater than  $K_{I0}(T < T_S)$ .

The constant  $K_I$  specimen tested at the highest temperature, i.e., 303 K, was 14 K above its solvus and had a slightly larger stress intensity threshold than the other two specimens tested at 10 K and 13 K above their solvus temperatures. This is consistent with the above model since the higher a specimen is tested above its solvus temperature, the greater the threshold stress intensity should be.

Figure 36 is a graph of  $K_{I0}(T < T_S)$  versus temperature for increasing, decreasing and constant  $K_I$  tests. The increasing and constant  $K_I$  thresholds are seen to follow the same trend, i.e.,  $K_{I0}(T < T_S)$  increases with decreasing temperature. The single point



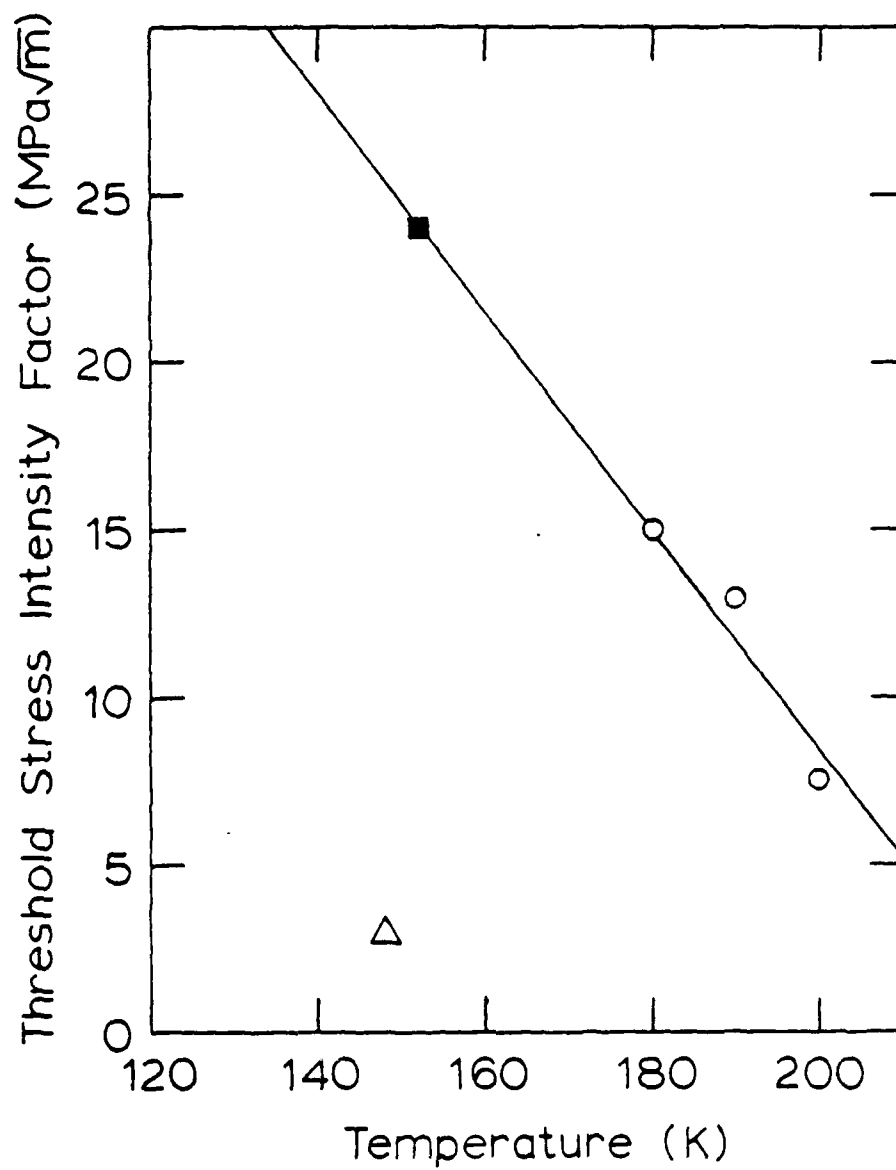


Fig. 65. Threshold stress intensity factor below the solvus versus temperature for increasing  $K_{Ic}$  (circles), constant  $K_{Ic}$  (square) and decreasing  $K_{Ic}$  (triangle) tests. Solid line is least squares fit to increasing  $K_{Ic}$  and constant  $K_{Ic}$  data.

plotted for the decreasing  $K_I$  tests below its solvus indicates a  $K_{I0}(T < T_s)$  of only  $3 \text{ MPa} \cdot \text{m}^{1/2}$  at 148 K and differs significantly from the increasing and constant  $K_I$  tests.

Gahr et al.<sup>(50)</sup> calculated the surface energies for cleavage of niobium hydride single crystals at 77 K and found the critical stress intensities,  $K_{IC}$ , to range from 0.9 to  $1.1 \text{ MPa} \cdot \text{m}^{1/2}$ . This indicates that additional factors are responsible for the larger  $K_{I0}(T < T_s)$  observed for the various tests in the present studies. The hydrides precipitated on cooling below the solvus in the fractured specimens were surrounded by a ductile solid solution matrix. Due to the volume increase on forming the hydride, the precipitates are in compression while the surrounding solid solution is highly deformed.<sup>(10)</sup> Under these circumstances the  $K_{I0}(T < T_s)$  may reflect the stress intensity to form dislocation pile-ups in the solid solution which initiate the cracking in the hydrides. Thus in constant  $K_I$  and increasing  $K_I$  tests the  $K_{I0}(T < T_s)$  reflects the plastic properties of the solid solution surrounding the precipitated hydrides. As a result  $K_{I0}(T < T_s)$  is larger than the  $K_{I0}$  measured on single crystals of hydrides and exhibits a strong temperature dependence (Fig. 65). In contrast to this behavior the low value observed (Fig. 65) in decreasing  $K_I$  tests corresponds to the hydride  $K_{I0}$  since in this test the  $K_{I0}$  measures the stopping of a crack which is already propagating in a hydride formed at higher  $K_I$  values. Since the crack already exists in the hydride the stress required to stop its propagation in the decreasing  $K_I$  test should correspond to the value measured by Gahr

et al. (50) The value of about  $3 \text{ MPa} \cdot \text{m}^{1/2}$  is in relatively good agreement with the value of  $1.0 \text{ MPa} \cdot \text{m}^{1/2}$  measured for the single crystal niobium hydride.

## 7. SUMMARY AND CONCLUSIONS

The underlying mechanism for the observed fracture behavior of hydrogen embrittled niobium was shown to be consistent with the fracturing of preexisting and stress induced hydrides. The specific behavior of the various (V-K) curves was shown to depend on the type of loading a specimen underwent. Similarities and differences in the (V-K) behavior were observed for increasing, decreasing and constant  $K_I$  tests.

Results of the decreasing  $K_I$  tests were able to be grouped in low, high and intermediate temperature ranges. The relationship between the specimen's test and solvus temperature, proved to be the determining factor in the type of (V-K) behavior observed. A unique three region (V-K) behavior occurred in the intermediate temperature tests. These regions were denoted A, B and C and are distinctly different from the three stage behavior observed in the constant  $K_I$  tests. The unusual observation of the crack velocity increasing with decreasing  $K_I$  (Region B) was shown to be due to the linking up of fractured hydrides to form one large crack.

Differences in the stress intensity threshold for the constant  $K_I$  specimens tested above and below their solvus temperatures were successfully explained in terms of the additional stress required to raise the solvus to allow hydride precipitation.

Comparison between the experimental and theoretical activation energies for Stage II of the constant  $K_I$  tests showed excellent

agreement. This gives further support to the proposed model of hydrogen diffusion to the crack tip being the rate limiting mechanism for crack growth during Stage II. Comparison between crack velocities measured in hydrogen and deuterium charged specimens used in decreasing  $K_I$  tests also showed excellent agreement with the expected differences due to the isotope effect. This again indicated that crack velocities are related to the diffusivities of hydrogen or its isotope.

Fractography was able to be correlated with (V-K) behavior of the various tests. Fracture surfaces of the s.e.n. specimens showed identical features of previous work<sup>(2)</sup> where transgranular cleavage was the only brittle failure mode observed. Fracture surfaces of intermediate temperature, decreasing  $K_I$  tests reflected its corresponding three region (V-K) curves particularly well. Brittle behavior occurred at low crack velocities and more ductile features were present at higher velocities reflecting the linking up of fracturing hydrides.

## APPENDIX A

## PHOTOELASTIC INVESTIGATION OF DOUBLE TORSION GEOMETRY

A.1 Introduction

Photoelastic investigation of the d.t. specimen was undertaken in order to document the stress distribution in the plane of the specimen. No analysis of this stress distribution appears in the literature although Trantina<sup>(33)</sup> used a three dimensional elastic finite element stress analysis to measure  $K_I$  in the plane of the crack. For models which are loaded to produce generalized plane stress conditions, the two principal stress directions and magnitudes do not change appreciably with model thickness. As a result, classical photoelastic techniques could be used for their stress analysis.

Though the d.t. specimen is in the shape of a rectangular plate, a three dimensional photoelastic technique v.i.z. the "frozen stress" method was used due to its particular loading arrangement. This method is normally reserved for more complicated configurations. Stressed models whose three principal stress axes change in magnitude and/or inclination in such a way that they are parallel to the incident ray of polarized light, require the "frozen stress" technique. By using the proper polymer and load-thermal cycle, the fringe pattern from an applied stress can be "frozen" into the model. The model can subsequently be cut into thin slices, without altering the fringe pattern, and examined as a generalized plane stress model.

As discussed by Hendry<sup>(51)</sup> the phenomenon of stress freezing is due to the existence of two phases in the plastic. One is very temperature dependent being rigid at room temperature and fluid at high temperature. The other phase has a small temperature dependency and is rigid at all temperatures but less so than the low temperature rigidity of the first phase. A mechanical model consisting of a spring in a fluid which is rigid at room temperature but fluid at the softening temperature represents the stress freezing behavior quite well.

#### A.2 Experimental Procedure.

The plastic d.t. specimen was machined out of a 1.02 cm thick plate of precast epoxy resin called PSM-9 obtained from Photoelastic Division, Measurements Group in Raleigh, North Carolina. The specimen was 5.6 cm wide and 12 cm long. A notch 4 cm long on top and 3.2 cm on bottom of the specimen was cut with a jeweler's saw. After machining, the specimen was placed in the Instron loading stage and immersed in an inert silicone oil bath. Heating and cooling rates were controlled by passing the current from a clock driven Variac through a 400 W heater. Temperature was monitored by thermocouples and kept uniform by circulating the oil. The heating rate was 150 K/hr. At a final temperature of 130 K, a load of 10 N was applied to the specimen. A crack initiated and advanced approximately 3 cm before arresting. While maintaining this load, the specimen was annealed for 2 hours. Temperature was then lowered to room temperature at a rate of 2 K/hr. After the stress freezing cycle, the specimen was sliced in the manner shown in Fig. 66. The slices consisted of six squares 3.3 cm on a side

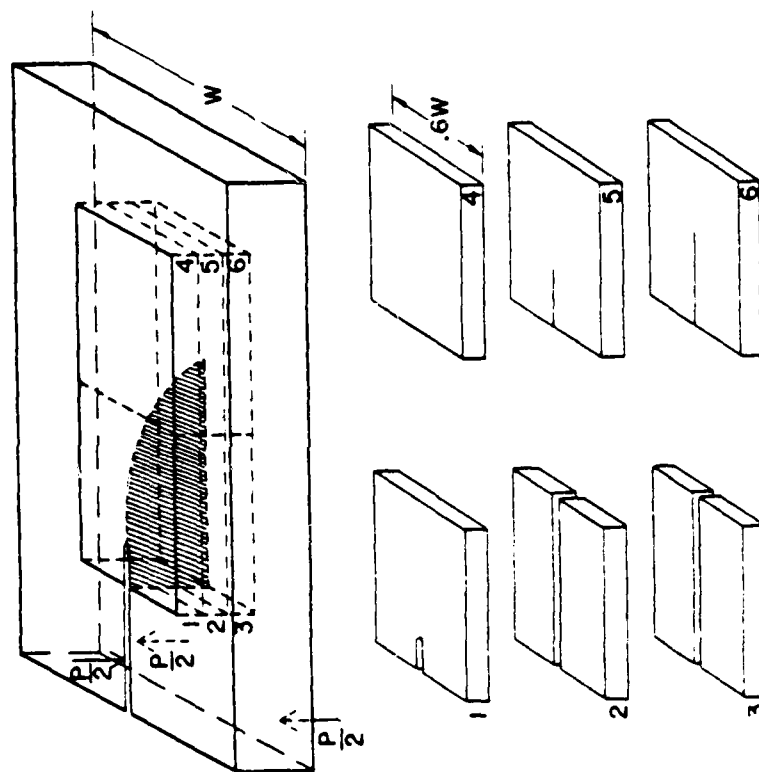


Fig. 66. Exploded view of plastic d.t. specimen showing slices used in photoelastic analysis.



corresponding to six tenths of the specimen width. Thicknesses are listed in Table 9. Slices two and three each consist of two halves since the propagating crack bisected them. Slices one, five and six were partially bisected. Slices one and four represent the top surface of the specimen, two and five, the middle and three and six, the bottom. These slices were cut using a water cooled jewelers saw to minimize generation of heat which would tend to distort the fringe pattern at the cut edges. Cut surfaces were wet sanded to eliminate surface scratches. A circular polariscope, model series 241 manufactured by the supplier of PSM-9, was used to observe the isochromatics and isoclinics. A fringe multiplier was used to obtain reasonable numbers of observable isochromatics. Only a multiplication of five, however, was attainable before off axis distortion prevented the resolution of higher order fringes. All isochromatics were photographed in bright field on Kodak's Contrast Process Ortho 4154 film using monochromatic light from a green filtered mercury lamp. Isoclinics were photographed on PN 55 Polaroid film using a diffuse fluorescent light source. Isoclinics for the middle section were difficult to locate and their presence for angles between  $40^\circ$  and  $90^\circ$  had to be estimated. The middle section only exhibited two orders of isochromatics even under a fringe multiplication of five.

#### A.3. Model Fringe Value Calculation

A measurement of the material stress fringe,  $f$ , for PSM-9 was necessary before the principal stress differences could be calculated from the isochromatics. The fringe value is defined as the stress

TABLE 9

Slice	Slice Thickness	Model Fringe Value (F)
	(t) (cm)	
		(Pa/fringe)
Top	0.234	$2.74 \times 10^4$
Middle	0.241	$2.66 \times 10^4$
Bottom	0.228	$2.81 \times 10^4$

required to produce n number of fringes in a plate of thickness t and is given by<sup>(52)</sup>

$$f = (\sigma_1 - \sigma_2)t/n \quad (51)$$

A calibration disk loaded in compression along a diameter was used to find the f value. The disk was cut to a diameter of 5.39 cm on a precision lathe out of the same sheet used in making the plastic d.t. model. The thermal cycle of the disk was controlled to closely duplicate the thermal cycle of the d.t. model. Isochromatics of the disk were photographed, without a fringe multiplier, in green monochromatic light. Both bright and dark field were used in order to obtain one half fringe resolution. The analytic expression for the principal stress differences at the center of the disk is given by<sup>(53)</sup>

$$\sigma_1 - \sigma_2 = 8P/\pi dt \quad (52)$$

where P = applied compressive load

d = diameter of disk

At the center of the disk, the fringe order was found to be 4.8 for an applied load of 32.5 N. Substituting Eqn. (52) into Eqn. (51) and solving for f yields  $f = 3.20 \times 10^{-4}$  Pa/fr/cm. This value must then be divided by five to obtain the proper material fringe value for the slices since their isochromatics were obtained using a fifth order fringe multiplication, so

$$f_{\text{slice}} = 6.40 \times 10^{-3} \text{ Pa/fr/cm.} \quad (53)$$

The model fringe values given for  $P = 1$  for the slices are listed in Table 4.

#### A.4 Principal Stress Differences and Directions

In this section, the isochromatics and isoclinics for the top, middle and bottom slices are given. The principal stress directions are drawn for the isoclinics (using the methods of Jessop and Harris), and the principal stress differences for several selected directions through the slices are compared. It is important to note that the calculated principal stresses are not the principal stresses but instead projections of the principal stress differences in the plane of the slices. With the information given below, it is not possible to resolve the stress differences into their principal components. A comprehensive solution to the stress distribution in the d.t. specimen would require a second identically prepared plastic d.t. specimen model whose slices were perpendicular to the original six. Then, in theory, the principal stresses could be resolved into their individual components. In practice, this is a very tedious procedure. The following analysis is not intended for exact work but is presented to give an approximate indication of the relative magnitude of the projected principal stress differences in the top, middle and bottom slices.

Figures 67-69 show the isoclinics and stress trajectories. Since the slices as well as the entire specimen are symmetrical about the plane of the crack surface, the isoclinics are drawn on the left half and the principal stresses are drawn on the right half for clarity of presentation. Figures 70-72 show the isochromatics for the top, middle

Fig. 67. Isoclines, isochronal curves and principal stresses (isochronal curves) for top slices (one and four

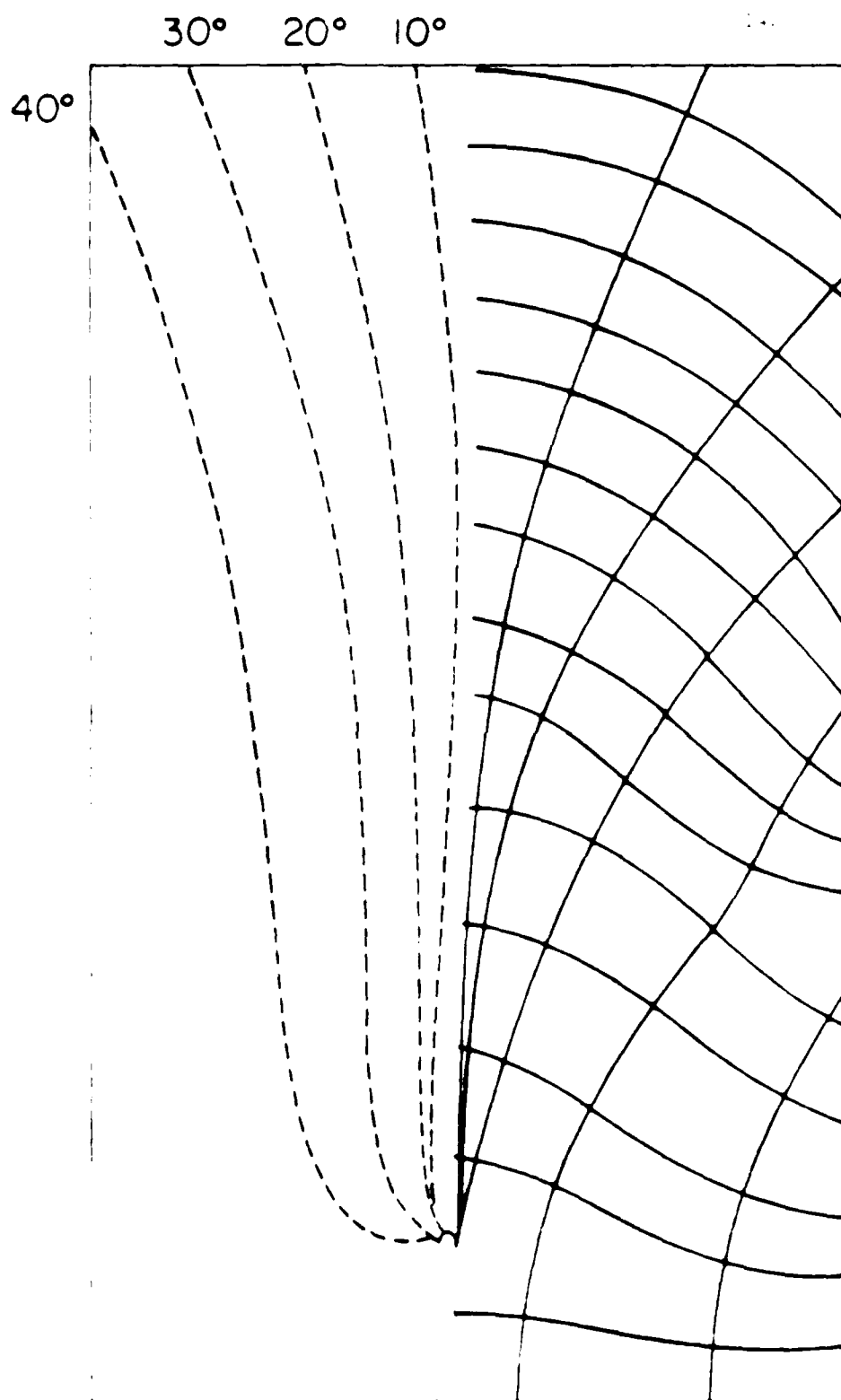


Fig. 68. Isoclinics (dashed curves) and principal stresses (solid curves) for middle slices (two and five).

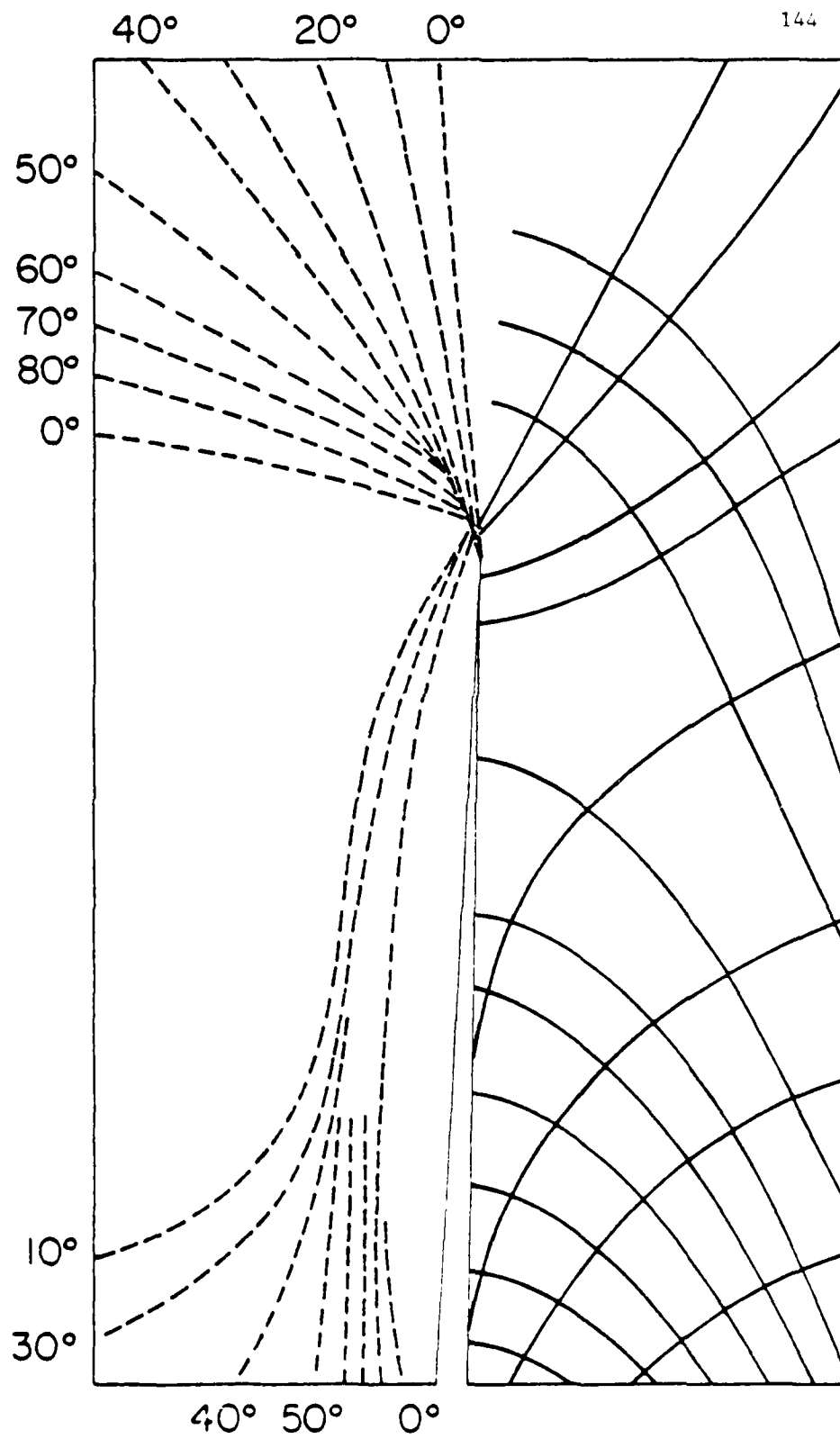




Fig. 69. Isoclinics (dashed curves) and principal stresses (solid curves) for bottom slices (three and six).

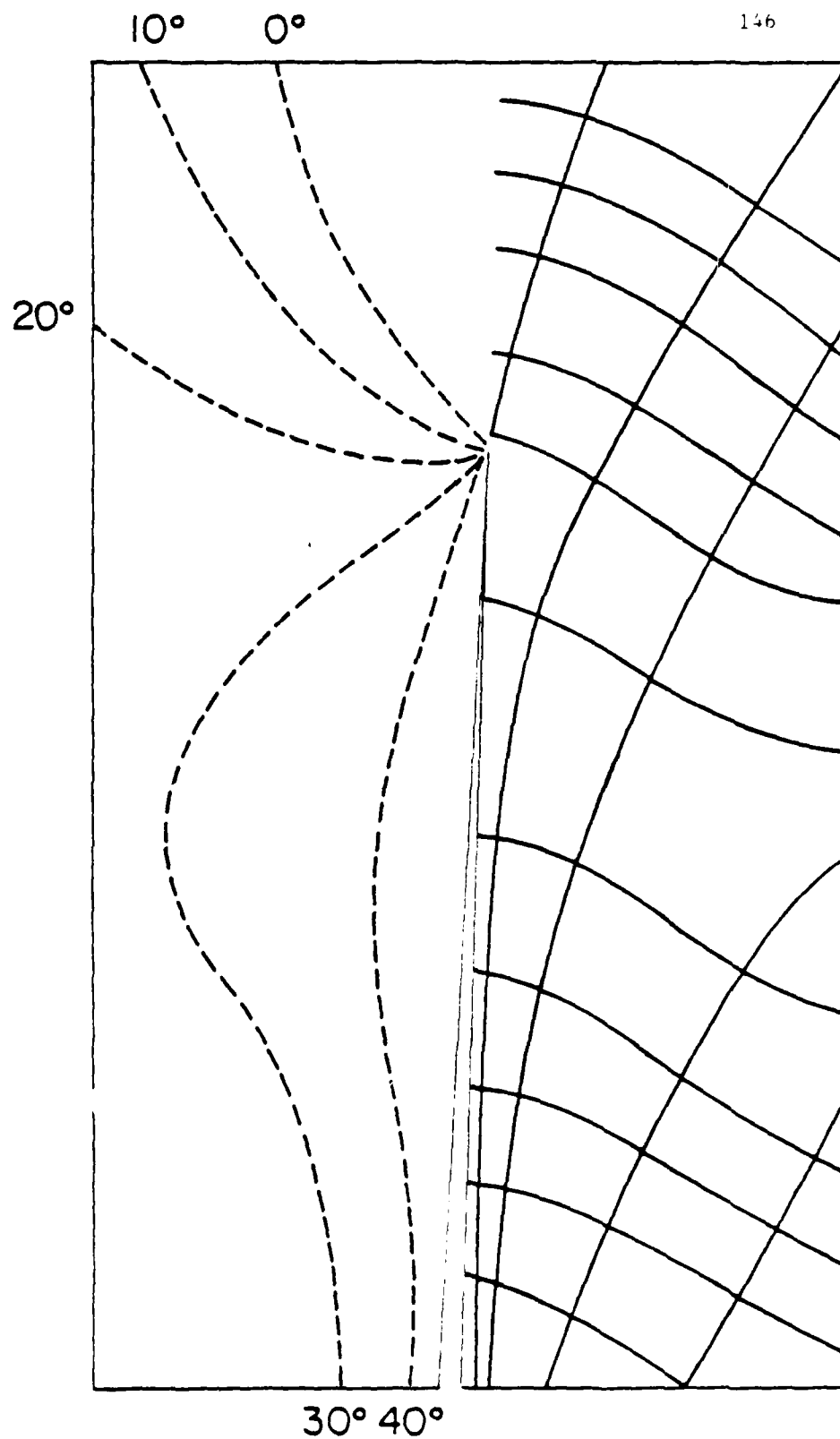


Fig. 70. Isochromatic fringes for top slices (one and four).  
Lines OA, OB and OC are graduated in tenths of  $(W/2)$ .

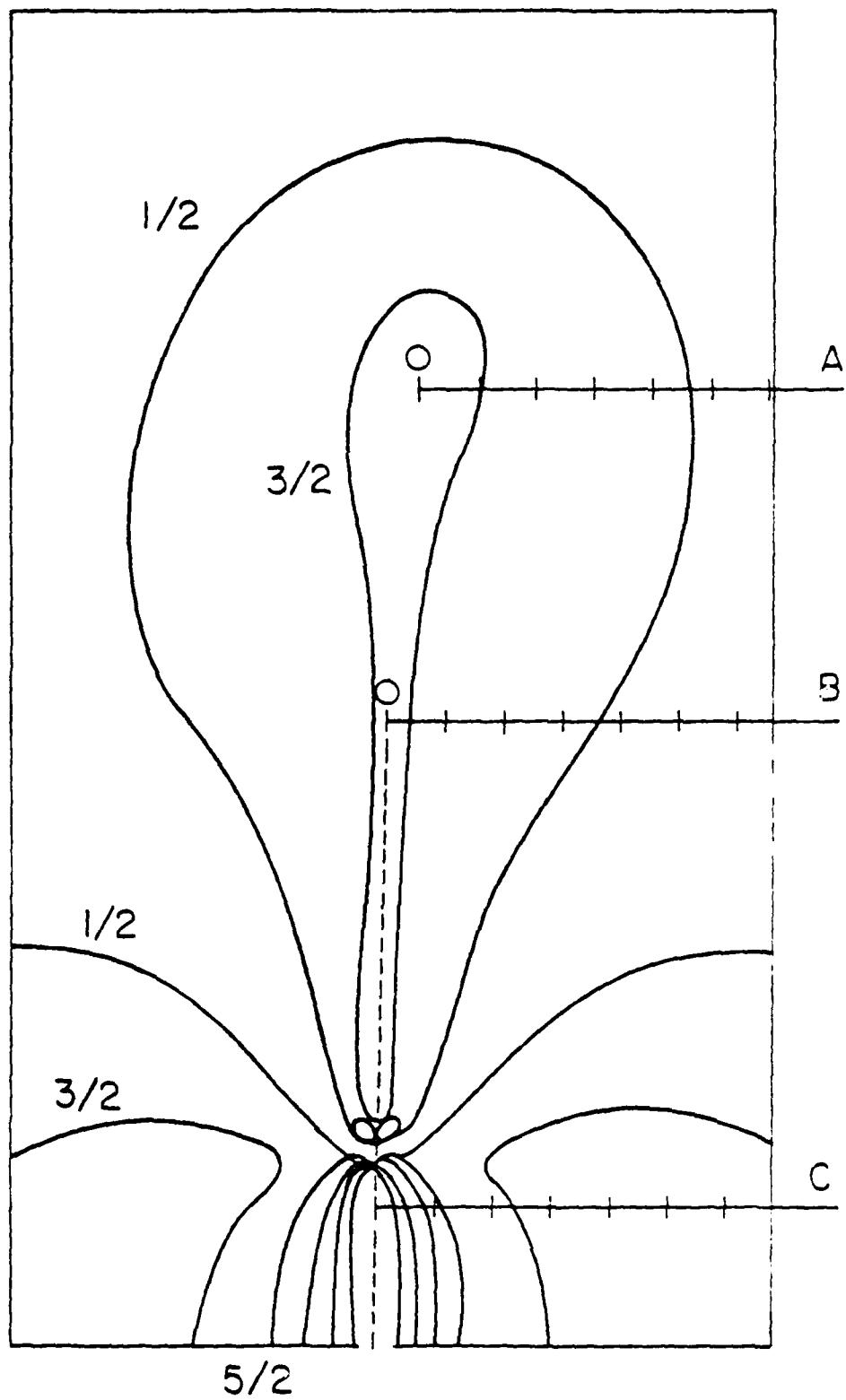


Fig. 71. Isochromatic fringes for middle slices (two and five).  
Lines OA.OB and OC are graduated in tenths of  $(W/2)$ .

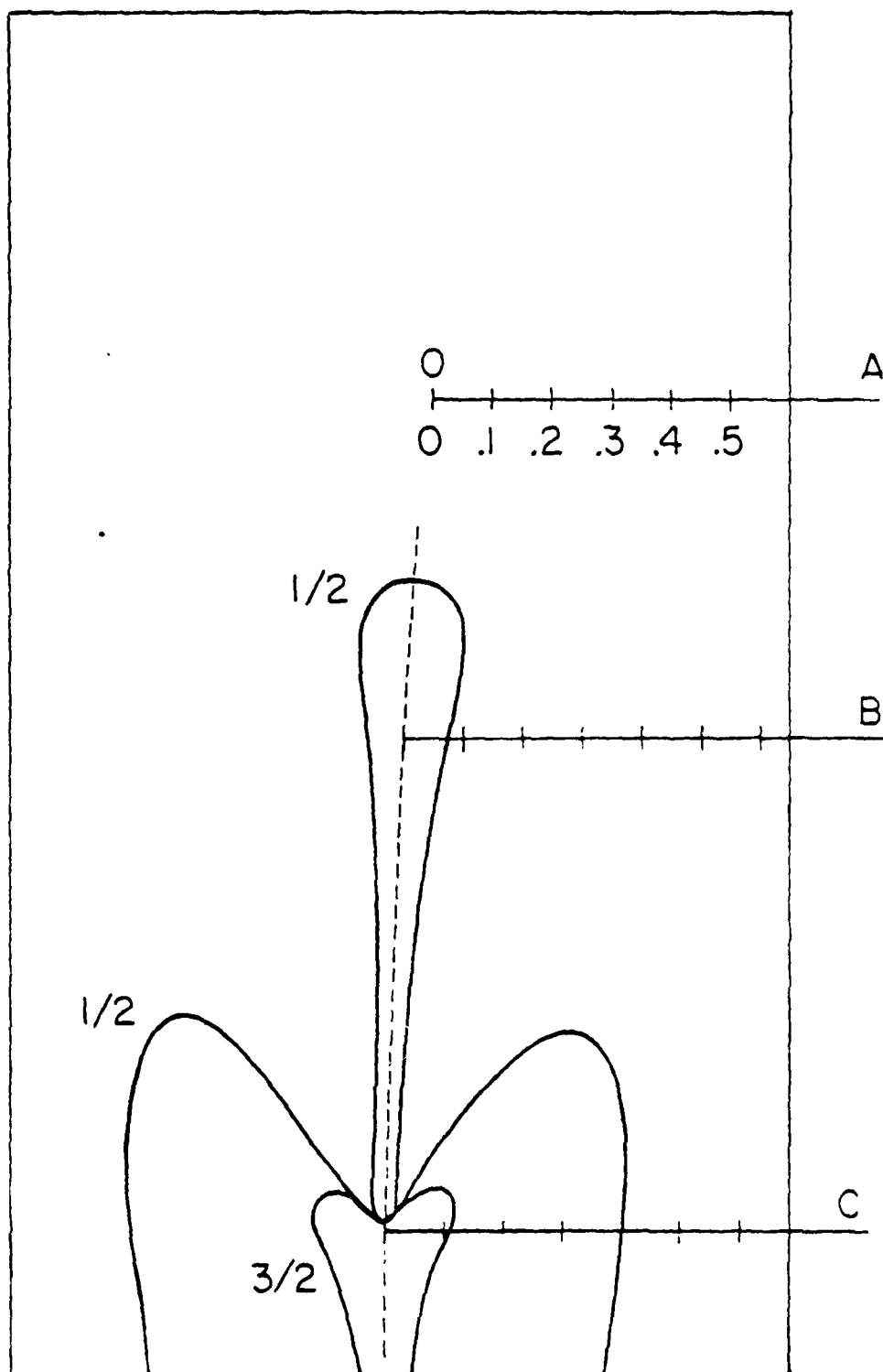
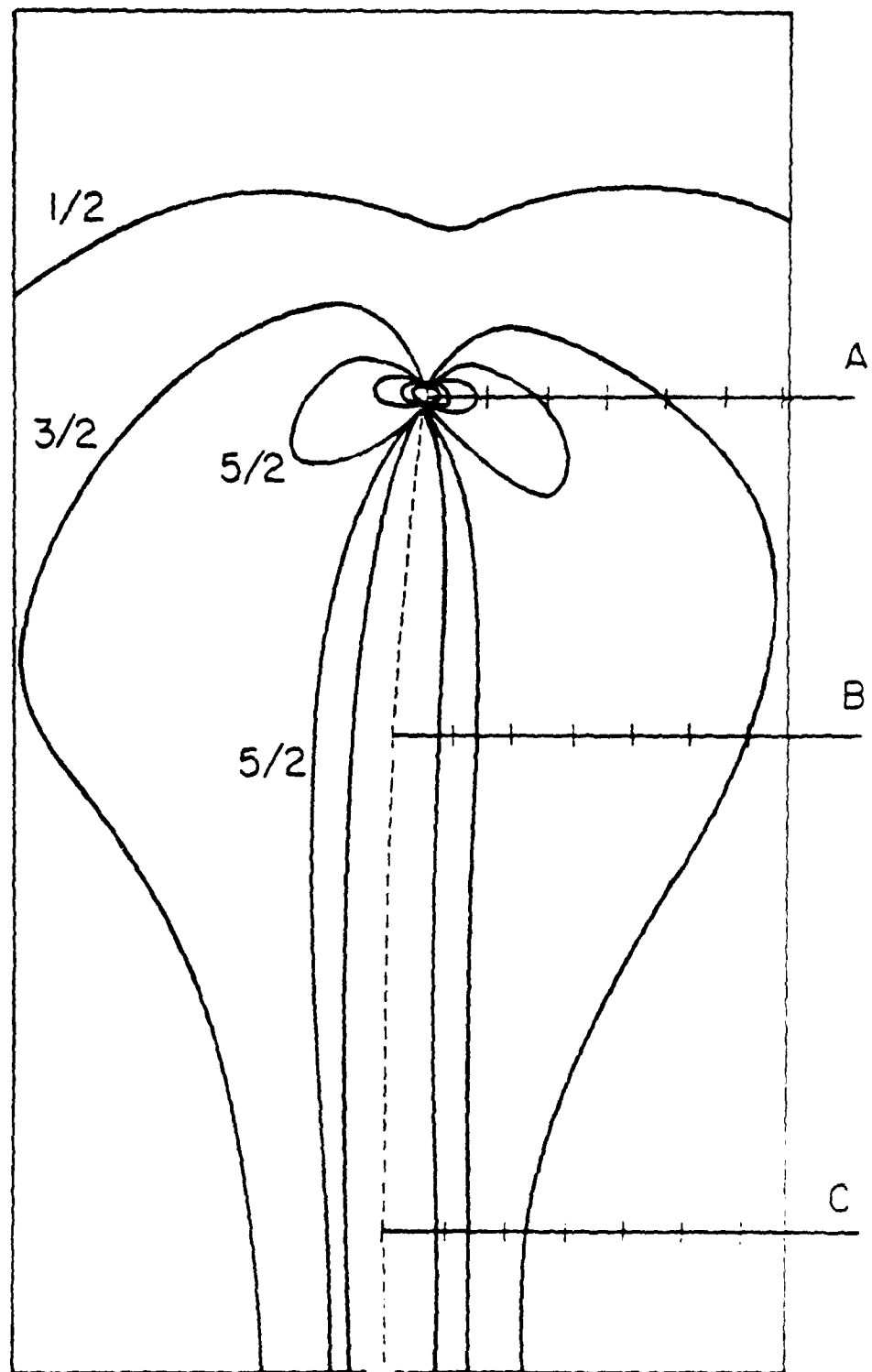


Fig. 72. Isochromatic fringes for top slices (three and six). Lines OA, OB and OC are graduated in tenths of  $(W/2)$ .





and bottom slices, respectively. All curves represent odd half numbers of relative wavelength retardation and are labeled for fringe order where space allowed. Also drawn on the right half of these isochromatic figures are three parallel lines labeled OA, OB and OC which lie perpendicular to the crack direction. Each line is graduated in fractional units of one half the width,  $W$  of the specimen. OA intersects the crack tip on the bottom slice, OC intersects the crack origin on the top slice and OB intersects the fracture surface on the top, bottom and middle. It is of interest to examine how the magnitude of the principal stress difference varies along lines OA, OB and OC for the three different levels. These results are shown in Figs. 73-75 and are discussed below.

The approximate state of stress near the crack front can be recognized simply by considering the loading arrangement of the d.t. specimen, thus, the crack front appearing on the top surface should be in a state of compression. The crack surface in the middle section should be in a type of neutral stress zone, similar to the neutral plane which occurs in a beam loaded in pure bending. On the bottom of the specimen, the crack surface should be in a state of tension.

Referring to Fig. 73, the principal stress difference along OA intersects the crack tip in the bottom surface and therefore exhibits the greatest stress concentration. The fractional orders of the isochromatics intersecting OA for the middle section were too ill defined to locate, however, they were substantially less than the stresses for the top or bottom. At the leading edge of the crack front, which corresponds to the origin of line OA on the bottom

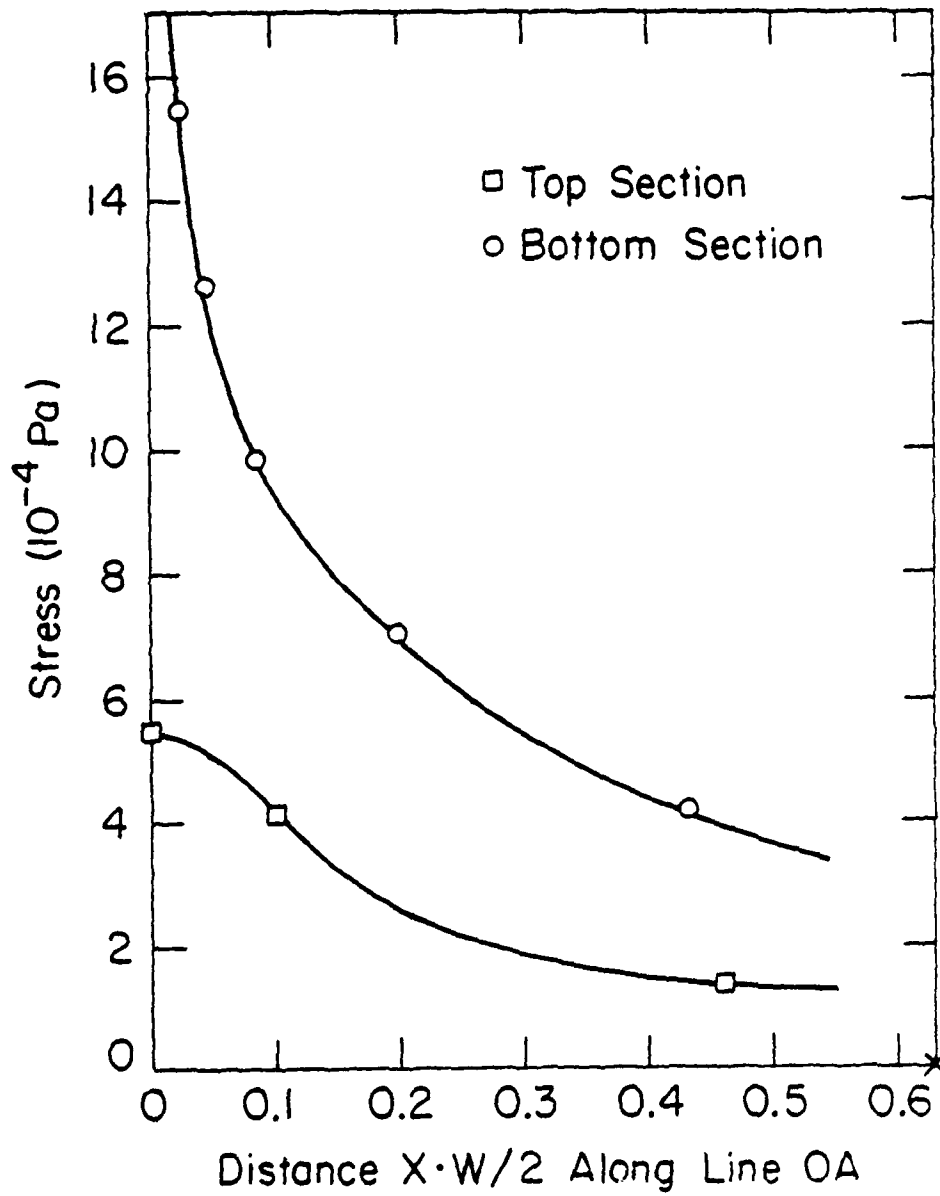


Fig. 73. Principal stress difference versus fractional distance along line OA for top and bottom slices.

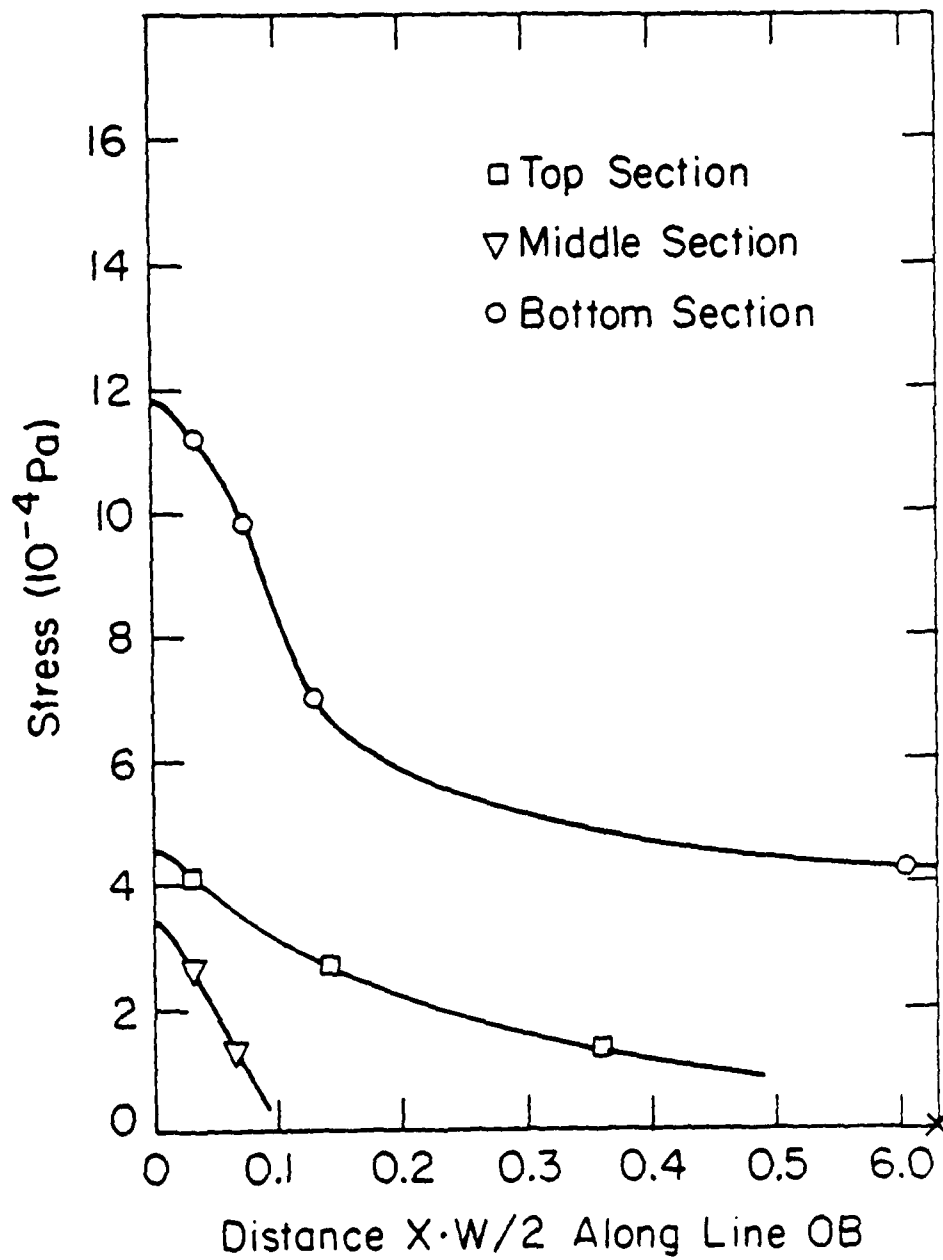


Fig. 74. Principal stress difference versus fractional distance along line OB for top, middle and bottom slices.

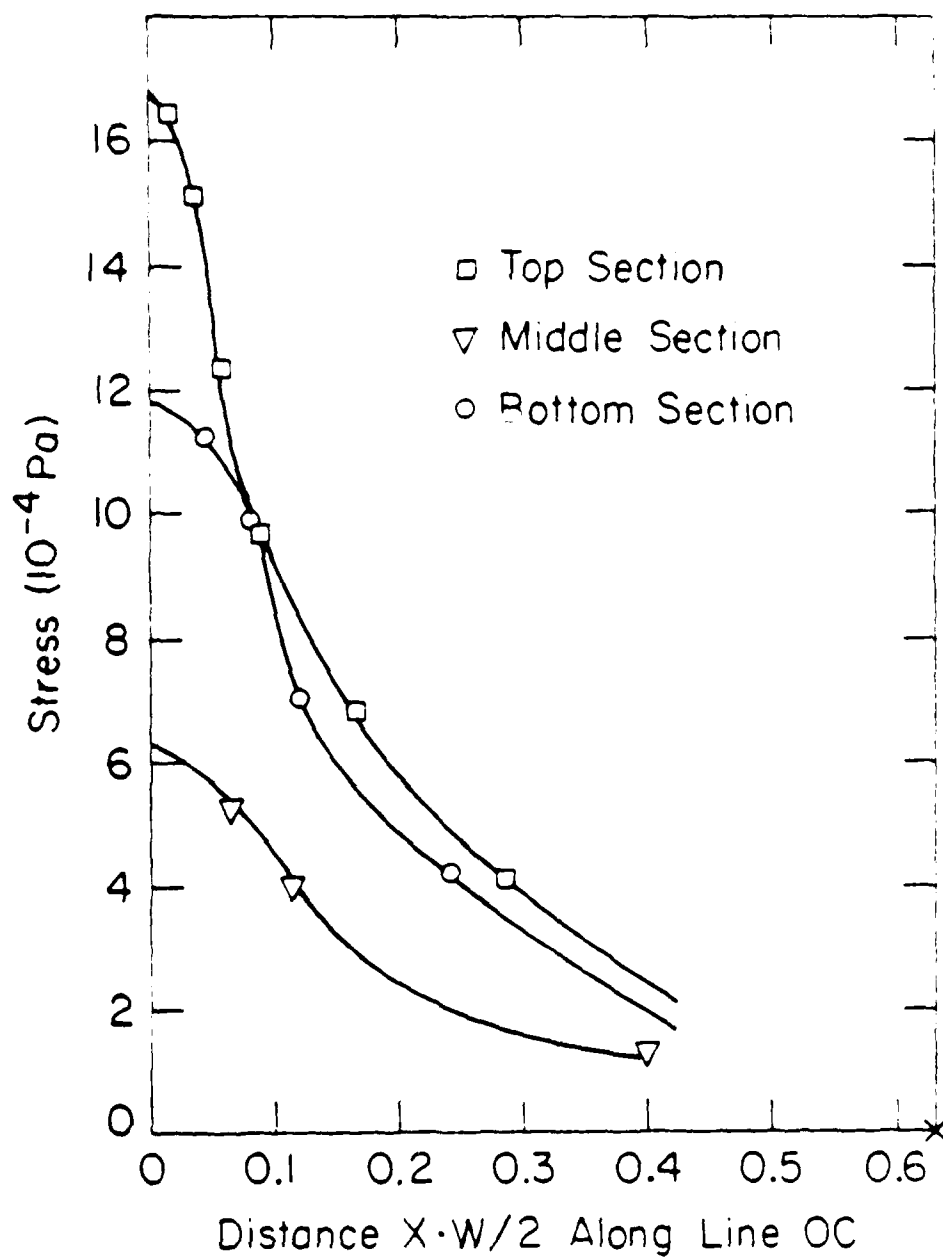


Fig. 75. Principal stress difference versus fractional distance along line OC for top, middle and bottom slices.

surfaces, the principal stress difference is at least greater by a factor of 3.5 than the origin of line OA on the top surface. In Fig. 74, the principal stress differences occurring along OB are also greatest for the bottom. The stresses in the middle were again less than those for top or bottom. In particular, the bottom stresses at the origin of OB were factors of 2.6 and 3.5 greater than the top and middle slices, respectively. As shown in Fig. 75, the principal stress differences along line OC are greatest for the top slice especially close to the crack surface. This is understandable since line OC is perpendicular to the intersection of the crack surface with the top surface. The stresses in the middle slice along OC are still less than the top and bottom but not as small as in the cases for lines OA and OB. In fact, for the middle, stresses along OC are almost identical to the stresses along OA for the top slice. At the trailing edge of the crack, which corresponds to the origin of line OC, the principal stress difference is maximum for the top surface and is a factor of 1.4 greater than the bottom slice stresses and a factor of 2.7 greater than the middle slice stresses.

#### A.5 Mode I Opening

Experimental data has suggested that the crack front is predominantly Mode I Opening.<sup>(17)</sup> As shown in Fig. 69, one of the principal stress directions, is almost perpendicular to the fracture surface at the crack tip. It has been shown that this is a tensile stress, implying a Mode I loading is occurring. This would then

justify the use of Mode I stress intensity factor,  $K_I$  in fracture mechanics calculations for the d.t. specimen.

## APPENDIX B

### ERROR ANALYSIS OF (V-K) DATA

Basically, two steps were used in calculating the error in the crack velocity and stress intensity factor. The first was the estimation of the uncertainties contained in the equations for V and K. These uncertainties were mostly due to instrumental errors. The second step was to use these uncertainties and employ the method of propagation of errors<sup>(55)</sup> to calculate the final probable errors. It was assumed in these calculations that all the observed fluctuations in the data were uncorrelated.

#### B.1 Single Edge Notch Tests

The stress intensity factor for the s.e.n. specimen was given by Eqn. (20). The uncertainties for  $K_I$  are listed below

$$\sigma_p = \pm 5 \text{ N}$$

$$\sigma_h/h = \pm 0.01$$

$$\sigma_w/w = \pm 0.002$$

$$\sigma_a = \pm 30$$

$$\sigma f(a/w)/f(a/w) = \pm 0.015$$

The error in  $K_I$  for the s.e.n. specimen can be written as

$$\sigma_{K_{\text{sen}}} = K_I \left[ \left( \frac{\sigma_p}{p} \right)^2 + \left( \frac{\sigma_a}{2a} \right)^2 + \left( \frac{\sigma f(a/w)}{f(a/w)} \right)^2 + \left( \frac{\sigma_w}{w} \right)^2 + \left( \frac{\sigma_h}{h} \right)^2 \right]^{1/2} \quad (54)$$

For typical values of  $a$ , and  $P$ , Eqn. (54) yields

$$\frac{\sigma_{K_{sen}}}{K_I} = \pm 3.4\% \quad (55)$$

The crack velocity for the s.e.n. specimen was given by Eqn. (19). The uncertainties for  $\Delta X$  and  $\Delta t$  are  $\sigma_{\Delta X} = \pm 10 \mu m$ ,  $\sigma_{\Delta t} = \pm 10 s$ . The error in  $V$  is given by

$$\sigma_V = \pm V \left[ \left( \frac{\sigma_{\Delta X}}{\Delta X} \right)^2 + \left( \frac{\sigma_{\Delta t}}{\Delta t} \right)^2 \right]^{1/2} \quad (56)$$

For typical values in  $\Delta t$ , Eqn. (56) yields

$$\frac{\sigma_V}{V} = \pm 7\% \quad (57)$$

## B.2. Double Torsion Tests

### B.2.1 Stress Intensity Factor

The stress intensity factor for the d.t. specimen was given in Eqn. (7). The uncertainties in the parameters of the constant  $C_1$  are given below

$$\sigma_w/W = \pm 0.0009$$

$$\sigma T/T = \pm 0.025$$

$$\sigma T_n/T_n = \pm 0.05$$

$$\sigma W_m/W_m = \pm 0.006$$

$$\sigma v/(1+v) = \pm 0.008$$



The error in  $K_I$  is given by

$$\sigma_{K_{d.t.}} = \pm K_I \left[ \left( \frac{\sigma_{wm}}{wm} \right)^2 + \left( \frac{\sigma_w}{2w} \right)^2 + \left( \frac{3\sigma_T}{2T} \right)^2 + \left( \frac{\sigma_{Tn}}{2Tn} \right)^2 + \frac{1}{4} \left( \frac{\sigma_v}{1+v} \right)^2 + \left( \frac{\sigma_p}{p} \right)^2 \right]^{1/2} \quad (58)$$

The uncertainty in the load measuring capability of the Instron's load cell is approximately  $\sigma_p/p = \pm 0.005$ . Substituting these uncertainties into Eqn. (58) yields

$$\sigma_{K_{dt}} / K = \pm 4.6\% \quad (59)$$

#### B.2.2 Constant Deflection Method (Decreasing $K_I$ )

The expression for the crack velocity during constant deflection was given by equation (14). The uncertainties in the constant  $C_2$  are the same as in the constant  $C_1$  except for the uncertainty in Young's modulus which is given by  $\delta E/E = \pm 0.05$ . The error in  $C_2$  is given by

$$\sigma_{C_2} = C_2 \left[ \left( \frac{\sigma_w}{w} \right)^2 + \left( \frac{\sigma_E}{E} \right)^2 + \left( \frac{3\sigma_T}{T} \right)^2 + \left( \frac{2\sigma_{wm}}{wm} \right)^2 + \left( \frac{\sigma_v}{1+v} \right)^2 \right]^{1/2} \quad (60)$$

Substituting the appropriate values into Eqn. (60) yields

$$\sigma_{C_2} / C_2 = \pm 12.7\% \quad (61)$$

The error in  $V_y$  after correcting for the effect of plasticity is given by

$$\sigma_{Vy} = V_y \left[ \left( \frac{\sigma C_2}{C_2} \right)^2 + \left( \frac{\sigma y}{y} \right)^2 + \left( \frac{\sigma t}{t} \right)^2 + 25 \times 10^{-6} \left( \frac{P_m^2 + P_p^2}{P_c^2} \right) \right]^{1/2} \quad (62)$$

For typical values,  $\sigma y/y = \sigma t/t = \pm 0.002$  and  $2 \lesssim (P_m^2 + P_p^2)/P_c^2 \lesssim 40$ , which results in

$$\sigma_{Vy}/V_y = \pm 13\% \quad (63)$$

The major contribution to the error in  $V_y$  is the uncertainty in the constant  $C_2$ .

### B.2.3 Constant Load Method (Constant $K_I$ )

The expression for the crack velocity during constant load tests was given by Eqn. (18). The error in  $V_p$  after correcting for the effect of plasticity is given by

$$\sigma_{vp} = \pm \sqrt{2} V_p \left[ \left( \frac{\sigma C_2}{C_2} \right)^2 + \left( \frac{\sigma p}{p} \right)^2 + \left( \frac{\sigma y}{y} \right)^2 + \left( \frac{\sigma t}{t} \right)^2 \right]^{1/2} \quad (64)$$

The factor of  $\sqrt{2}$  in equation (64) arises from calculating the error in the differences of two quantities each with the same error. The ratio  $\sigma p/p$  for the constant load method was approximately 0.01 and using typical values for the other uncertainties in Eqn. (64), yields

$$\sigma_{vp}/V_p = \pm 18\% \quad (65)$$

APPENDIX C  
VELOCITY MEASUREMENT LIMITS

C.1 Single Edge Notch Tests

The minimum crack velocity that could be measured using the inscribed s.e.n. specimen and video observation is limited only by the patience of the observer. In practice, velocities as low as  $10^{-10}$  m/s could be observed. The maximum crack velocity is limited by the time required for the specimen to fracture within the duration of one video frame. This corresponds to a crack velocity of approximately  $5 \times 10^{-2}$  m/s.

C.2 Double Torsion, Constant Deflection (Decreasing  $K_I$ )

The minimum crack velocity that could be measured using the d.t. specimen depended on several factors. Among these are the presence of thermal fluctuations in the loading frame, and the stability and precision of the measuring and data acquisition instruments. For the constant deflection method, the limiting factors are the presence of various thermal fluctuations and gradients which may affect the measured load. The requirement to achieve testing temperatures either above or below room temperature introduces additional thermal gradients in the loading frame which may affect the measured load. The use of materials in the loading frame with differing thermal coefficients of expansions will cause further changes in the measured load due to ambient thermal fluctuations. In this investigation, the

affects of thermal gradients were minimized by waiting a sufficiently long time to achieve steady state conditions before testing a specimen. Thermal fluctuations were minimized by air conditioning the room and keeping the duration of an average crack velocity test from 1/2 to 5 hours. These precautions enabled crack velocities as low as  $10^{-8}$  m/s to be measured with reasonable confidence. Using precise temperature control, other investigators<sup>(56)</sup> measured crack velocities as low as  $10^{-9}$  m/s and Evans<sup>(17)</sup> claimed to measure crack velocities down to  $10^{-11}$  m/s in glass.

For constant deflection tests, upper crack velocity measurements were limited by the response of the load cell to changes in load. Since the load cell has a high frequency response, crack velocities of several hundred meters per second could be measured reliably. If, however, a strip chart is required to record the load relaxation, an upper limit of only several meters per second could be measured.

### C.3 Double Torsion, Constant Load (Constant $K_I$ )

For the constant load method, the limiting factor for measuring small crack velocities was the stability of the constant load controller. Crack velocities near  $10^{-8}$  m/s were measurable when the load controller was properly adjusted. Upper crack velocity measurement was limited by the response and speed of the moveable crosshead to maintain a desired load. This placed a limit of approximately  $5 \times 10^{-2}$  m/s for the maximum velocity that could be measured.

## REFERENCES

1. H. K. Birnbaum, Environment - Sensitive Fracture of Engineering Materials, Z. A. Foroulis, ed., p. 326, The Metallurgical Society of AIME, Warrendale, PA, (1979).
2. M. L. Grossbeck, Ph.D. Thesis, Univ. of Illinois (1975).
3. J. C. M. Li, R. A. Oriani and L. S. Darken, Z. Phys. Chem. Neue Folge, 49, 271, (1966).
4. M. P. Puls, Scr. Metall., 12, 595, (1978).
5. M. P. Puls, Atomic Energy of Canada Limited, Report AECL-6302, Aug., (1978).
6. T. B. Flanagan, N. B. Mason and H. K. Birnbaum, Scr. Metall., to be published.
7. D. G. Westlake and S. T. Ockers, Metall. Trans., 6A, 399, (1975).
8. W. M. Albrecht, M. W. Mallet and W. S. Goode, J. Electrochem. Soc., 105, 219, (1958).
9. H. K. Birnbaum, M. L. Grossbeck and M. Amano, J. Less-Common Met., 49, 357, (1976).
10. B. J. Makenas and H. K. Birnbaum, Acta Metall., 28, 979, (1980).
11. M. L. Grossbeck and H. K. Birnbaum, Acta Metall., 25, 135, (1977).
12. S. Koike and T. Suzuki, Acta Metall., to be published.
13. A. G. Evans and H. Johnson, J. Mater. Sci., 10, 214, (1975).
14. P. W. R. Beaumont and R. J. Young, J. Mater. Sci., 10, 1334, (1975).
15. H. P. van Leeuwen, Corrosion, 31, 42, (1975).
16. A. G. Evans, Int. J. Fract., 10, 251, (1974).

17. A. G. Evans, J. Mater. Sci., 7, 1137, (1972).
18. S. J. Hudak and R. P. Wei, Metall. Trans., 7A, 235, (1976).
19. R. P. Wei, S. R. Novak and D. P. Williams, Mater. Res. Stand., 12, no. 9, p. 25, (1972).
20. C. S. Carter, Corrosion, 27, 11, (1971).
21. H. G. Nelson, Metall. Trans., 7A, 621, (1976).
22. H. G. Nelson, D. P. Williams and J. E. Stein, Metall. Trans., 3, 469, (1972).
23. D. P. Williams and A. G. Evans, J. Test. Eval., 1, no. 4, 264, (1973).
24. D. P. Williams and H. G. Nelson, Metall. Trans., 1, 63, (1970).
25. R. A. Oriani and P. H. Josephic, Acta, Metall., 25, 979, (1977).
26. R. Dutton, K. Nuttall, M. P. Puls and L. A. Simpson, Metall. Trans., 8A, 1553, (1977).
27. L. A. Simpson and M. P. Puls, Metall. Trans., 10A, 1093, (1979).
28. L. A. Simpson and C. F. Clarke, Atomic Energy of Canada Limited, Report AECL 5815, Oct., (1979).
29. J. O. Outwater and D. J. Gerry, NRL Interim Contract Report, Contract NONR 3219(01)(x), AD 640848, Univ. of Vermont, Burlington, Vt., (1966).
30. J. A. Kies and B. J. Clark, Fracture- 1969, P. L. Pratt, ed., Chapman and Hall, Ltd., London, pp. 483-491, (1969).
31. J. C. Pollet and S.J. Burns, J. Am. Ceram. Soc., 62, no. 5-6, p. 426, (1979).
32. D. K. Shetty, Anil. V. Virkar and M. B. Howard, J. Am. Ceram. Soc., 62, no. 5-6, p. 307, (1979).

33. G. G. Trantina, J. Am. Ceram. Soc., 60, no. 7-8, p. 338, (1977).
34. V. V. Novozhilov, Theory of Elasticity, Translation from the Russian book Teoriya Uprugosi, Israel program for Scientific Translation, Jerusalem, p. 232, (1961).
35. D. W. Chung and N. S. Stoloff, Metall. Trans., 9A, 1386, (1978).
36. W. W. Gerberich and Y. Katz, Eng. Fract. Mech., 1, 569, (1969).
37. W. F. Brown, Jr. and J. E. Srawley, Am. Soc. Test. Mater. Spec. Tech. Publ. No. 410, (1966).
38. R. E. Peterson, Stress Concentration Factors, Wiley, N. Y., (1974).
39. S. J. Burns, Private communications, (1979).
40. E. R. Fuller, Jr., Fracture Mechanics Applied to Brittle Materials, ASTM STP No. 678, S. W. Freiman, ed., ASTM, Philadelphia, PA, pp. 3-18, (1979).
41. G. Matusiewicz, R. Booker, J. Keiser and H. K. Birnbaum, Scr. Metall., 8, 1419, (1974).
42. S. Gahr, M. L. Grossbeck and H. K. Birnbaum, Acta Metall., 25, 125, (1977).
43. H. Wipf and G. Alefeld, Phys. Status Solidi (A), 23, 175, (1974).
44. G. Matusiewicz and H. K. Birnbaum, J. Phys. F., 7, no. 11, 2285, (1977).
45. G. Schaumann, J. Völkl and G. Alefeld, Phys. Status Solidi (A), 42, 401, (1970).
46. D. I. Bolef, J. Appl. Phys., 32, 100, (1961).
47. M. S. Rashid and T. E. Scott, J. Less-Common Met., 30, 399, (1977).

48. C. C. Chen and R. J. Arsenault, Hydrogen in Metals, I. M. Bernstein and A. W. Thompson, ed., p. 393, Metals Park, Ohio, American Society for Metals (1974).
49. I. A. Pereturina and V. A. Pavlov, Phys. Met. Metallogr., 41, No. 4, p. 146, (1976).
50. S. Gahr, B. J. Makenas and H. K. Birnbaum, Acta Metall., 28, 1207, (1980).
51. A. W. Hendry, Elements of Experimental Stress Analysis, S. I. Edition, Pergamon Press, Oxford, p. 97, (1977).
52. A. J. Durelli and W. F. Riley, Introduction to Photomechanics, Prentice-Hall, Inc., Englewood Cliffs, N.J., p. 64, (1965).
53. S. P. Timoshenko and J. N. Goodier, Theory of Elasticity, third Edition, McGraw Hill, N.Y., p. 167, (1970).
54. H. T. Jessop and F. C. Harris, Photoelasticity, Principles and Methods, Dover, N. Y., p. 73, (1960).
55. P. R. Bevington, Data Reduction and Error Analysis for the Physical Sciences, McGraw Hill, N.Y., p. 56, (1969).
56. B. J. Pletka, E. R. Fuller, Jr. and J. G. Koepke, Fracture Mechanics Applied to Brittle Materials, ASTM STP. No. 678, S. W. Freiman, ed., ASTM, Philadelphia, PA, pp. 19-37 (1979).



## VITA

Barry Scott Hindin was born on January 19, 1953 in Chicago, Illinois and resided there until graduating from Stephen Mather High School in 1970. As a junior high school student in 1969, he entered the Chicago Public School Science Fair contest and his paper entitled "The Effects of Electromagnetic Fields on the Acceleration of Steel Ball Bearings" won first place in the physics division. He enrolled at the University of Wisconsin at Madison in 1970 and as a physics major established and became president of the undergraduate Physics Club in 1973 and graduated with a Bachelor of Science Degree in 1974. Since 1974 he has been a graduate research assistant in the Department of Metallurgy and Mining Engineering at the University of Illinois at Urbana-Champaign. In August 1979, he married Emily Louise Sudman.

Unclassified

Security Classification

DOCUMENT CONTROL DATA - R & D		
<i>(Security classification of title, body of abstract and indexing annotation must be entered when the overall report is classified)</i>		
1. ORIGINATING ACTIVITY (Corporate author)		2a. REPORT SECURITY CLASSIFICATION
University of Illinois at Urbana Champaign		Unclassified
		2b. GROUP
3. REPORT TITLE		
Fracture Kinetics of Hydrogen Embrittled Niobium		
4. DESCRIPTIVE NOTES (Type of report and inclusive dates)		
Technical Report		
5. AUTHOR(S) (First name, middle initial, last name)		
Barry S Hindin and H K Birnbaum		
6. REPORT DATE	7a. TOTAL NO. OF PAGES	7b. NO. OF REFS
March 1981	168	56
8a. CONTRACT OR GRANT NO	9a. ORIGINATOR'S REPORT NUMBER(S)	
USN 00014-75-C-1012		
b. PROJECT NO		
c.	9b. OTHER REPORT NO(S) (Any other numbers that may be assigned this report)	
d.		
10. DISTRIBUTION STATEMENT		
This document is unclassified. Reproduction and distribution for any purpose of the US Government is permitted.		
11. SUPPLEMENTARY NOTES		12. SPONSORING MILITARY ACTIVITY
		Office of Naval Research
13. ABSTRACT		
See attached		

DD FORM 1473

Unclassified

Security Classification

Unclassified

Security Classification

14	KEY WORDS	LINK A		LINK B		LINK C	
		ROLE	WT	ROLE	WT	ROLE	WT
	hydrogen Niobium Hydrogen embrittlement Fracture Fracture kinetics						

Unclassified

Security Classification

DATE  
FILMED  
-18